UNIVERSIDADE DE SÃO PAULO
FACULDADE DE FILOSOFIA, CIÊNCIAS E LETRAS DE RIBEIRÃO PRETO
PROGRAMA DE PÓS-GRADUAÇÃO EM FÍSICA APLICADA À MEDICINA E BIOLOGIA

RENAN HIROSHI MATSUDA

Robotized System for Navigated Transcranial Magnetic Stimulation
Sistema Robotizado para Estimulação Magnética Transcraniana Navegada

Ribeirão Preto – SP
2022

UNIVERSIDADE DE SÃO PAULO
FACULDADE DE FILOSOFIA, CIÊNCIAS E LETRAS DE RIBEIRÃO PRETO
PROGRAMA DE PÓS-GRADUAÇÃO EM FÍSICA APLICADA À MEDICINA E BIOLOGIA

Robotized System for Navigated Transcranial Magnetic Stimulation

Sistema Robotizado para Estimulação Magnética Transcraniana Navegada

RENAN HIROSHI MATSUDA

Versão Corrigida

Tese apresentada à Faculdade de Filosofia, Ciências e Letras de Ribeirão Preto da USP, como parte das exigências para a obtenção do título de Doutor em Ciências.

Área de concentração: Física Aplicada à Medicina e Biologia.

Orientador: Prof. Dr. Oswaldo Baffa Filho
Coorientador: Dr. Victor Hugo Souza

Ribeirão Preto – SP
2022

Catalogação da Publicação
Serviço de Documentação da Universidade de São Paulo
Faculdade de Filosofia, Ciências e Letras de Ribeirão Preto

Matsuda, Renan Hiroshi

Robotized System for Navigated Transcranial Magnetic Stimulation / Renan Hiroshi Matsuda; orientador Oswaldo Baffa Filho, coorientador Victor Hugo Souza. Ribeirão Preto – SP, 2022.

137 f.: il.

Tese (Doutorado em Ciências) – Programa de Pós-Graduação em Física Aplicada à Medicina e Biologia, Faculdade de Filosofia, Ciências e Letras de Ribeirão Preto, Universidade de São Paulo, 2022.

Orientador: Prof. Dr. Oswaldo Baffa Filho

Coorientador: Victor Hugo Souza

1) Neuronavegação. 2) Estimulação magnética transcraniana. 3) Instrumentação Biomédica. 4) Robôs colaborativos. 5) Visão Computacional.

Nome: MATSUDA, Renan Hiroshi

Título: Robotized System for Navigated Transcranial Magnetic Stimulation

Tese apresentada à Faculdade de Filosofia, Ciências e Letras de Ribeirão Preto para obtenção do título de Doutor em Ciências.

Aprovado em: 28/11/2022

Banca Examinadora

Prof. Dra. Claudia Domingues Vargas

Professora Titular do Instituto de Biofísica Carlos Chagas Filho/UFRJ.

Julgamento: Aprovado

Prof. Dr. André Russowsky Brunoni

Professor Associado do Departamento de Psiquiatria da Faculdade de Medicina/USP.

Julgamento: Aprovado

Prof. Dr. Antonio Adilton Oliveira Carneiro

Professor Titular do Departamento de Física da Faculdade de Filosofia, Ciências e Letras de Ribeirão Preto/USP.

Julgamento: Aprovado

PREFACE

This doctoral thesis contains the results of research undertaken at the Physics Department of the Faculty of Philosophy, Science and Letters of Ribeirão Preto, University of São Paulo, Brazil. Part of this work was accomplished at the Department of Neuroscience and Biomedical Engineering, Aalto University School of Science, Espoo, Finland, under the supervision of Professor Risto J. Ilmoniemi.

During my doctoral thesis, my fascination with biomedical instrumentation led me to expand applications and technological developments beyond TMS. Regarding brain studies, I had the opportunity to collaborate on two papers: “Forearm and hand muscles exhibit high coactivation and overlapping of cortical motor representations” and “Motor potential evoked by transcranial magnetic stimulation depends on the placement protocol of recording electrodes: a pilot study”. Also, I had the honor to lead the writing of a dissemination review paper about TMS, entitled: “Estimulação magnética transcraniana: uma breve revisão dos princípios e aplicações”. As a complementary reading, I recommend the paper published by our group, entitled “Development of an Optical Pumped Gradiometric System to Detect Magnetic Relaxation of Magnetic Nanoparticles”.

AGRADECIMENTOS / ACKNOWLEDGMENTS

Meu primeiro agradecimento vai ao meu orientador e coorientador. Ao longo de quase onze anos trabalhando juntos, tenho o privilégio de ter muito mais que um orientador e co-orientador, tenho dois grandes amigos que sempre me apoiaram e me incentivaram ao longo de minha carreira acadêmica. Desde minha iniciação científica, em 2012, passando pelo mestrado, em 2017, e agora, meu doutorado, de 2018-2022. Ao Professor Oswaldo Baffa, uma pessoa autêntica, sempre me senti muito acolhido ao seu lado. Orgulho, é a palavra que melhor descreve o sentimento de poder trabalhar e aprender ao seu lado. Baffa é minha inspiração como cientista, não apenas por suas grandes contribuições na ciência e na educação, mas também nas relações interpessoais, sempre leve, sorridente e aberto para conversar e me ensinar algo sobre qualquer assunto. Ao Victor Hugo Souza, meu irmão da pesquisa, comecei minhas atividades no laboratório de Biomagnetismo graças a uma visita apresentada por você. De cara fiquei fascinado no sistema de neuronavegação e na possibilidade de me tornar um pesquisador. Tenho imensa gratidão por todos os aprendizados e admiração de poder trabalhar ao seu lado.

Aos companheiros de laboratório; Fernando, Gabriela, Petrus, Thais, Carlos, Guilherme, Matheus, Leonardo França e Leonardo Rakauskas muito obrigado pela amizade, companheirismo no lab, por todo o auxílio, conversas e inúmeros cafés. Aos amigos tagmáticos Felipe Grillo e Carlo Rondinoni, obrigado pelas parcerias dos projetos, é um prazer trabalhar com vocês. Agradeço a oportunidade de aprender com os professores Glauco Caurin, Hélio Machado, Jorge Silva e em especial Marco Garcia e André Peres. Marquinho, muito obrigado pela confiança e as intensas colaborações. André, obrigado pela coragem em iniciar os trabalhos com neuronavegação e TMS no laboratório. Thiago Moraes e Paulo Amorim sempre solícitos a desenvolver novas ferramentas e melhorias no InVesalius, muito obrigado! Aos funcionários da secretaria, Nilza e Denise, e aos técnicos Carlos Renato Silva, Lourenço Rocha e Élcio Navas por todo o suporte. Sem eles, nada disso seria possível.

I would like to thank you Prof. Risto Ilmoniemi for giving me the opportunity to work in your group at Aalto University. Many thanks for your support and belief. I learned a lot from you, and it is an honor to work with such an inspiring and brilliant person. People commonly say the finns have frozen hearts, but that is not true, Risto has a warm and open heart and welcomed me in Finland like at home. During my stay in Finland I could work with a fantastic group. Ana Soto, thank you so much for the friendship and several discussions. You are awesome! Work by your side is productive and fun, at the same time. Heikki, Mikko, Minh, Joonas, Ivan, Isabel, Eva, Hanna, Mikael, Olli-Pekka, Andrey, Baran, Dubravko Dubi, Jaakko, Pantelis, and Tuomas, thank you for the fellowship, friendship, and shared experiences.

Muito obrigado aos meus pais, Edson e Edwiges. Minha maior base, toda admiração e respeito pela minha criação, por todo o carinho e suporte que me proporcionam. Pelas broncas e puxões de orelha, sempre me motivando quando não me sentia capaz ou me sentia inseguro com minhas escolhas. Amo vocês! Levo comigo o seguinte ensinamento: “Aprender por aprender é estudo morto, enquanto aprender algo para ser utilizado na sociedade é estudo vivo”, Mokiti Okada. As minhas irmãs, Karen e Leila. Sempre abertas a me apoiar e me ouvir, muito obrigado! A minha família, especialmente a tia Mitiko. Meu porto seguro em Ribeirão Preto. Obrigado por ter me acolhido e me incentivado à carreira acadêmica.

Outra parte fundamental dessa caminhada foram as amizades que Ribeirão Preto me proporciona. A Rep. Zika, e aos queridos amigos Poti, Gambs, Ballina, Vicenzo, e Piaui agradeço pelas conversas, churrascos e incontáveis cervejas, sei que posso sempre contar com vocês.

Um muito obrigado especial para minha companheira, Katharine, por sempre me apoiar, incentivar, pela paciência e por todo o amor. Você tornou essa caminhada mais suave e cheia de experiências boas. Através da Kath, conheci pessoas incríveis, obrigado Perereca, Pri, Ana, Germano, Aline, Dri e Tércio.

Este trabalho recebeu financiamento do Conselho Nacional de Desenvolvimento Científico e Tecnológico (CNPq) (bolsa nº 141056/2018-5), da Academia da Finlândia, do European Research Council (ERC) under the

European Union’s Horizon 2020 research and innovation programme (No. 810377), e da FAPESP pelo Centro de Pesquisa, Inovação e Difusão em Neuromatemática (nº 2013/07699-0).

Dedico este trabalho à minha
Batchian Luzia, i*n memoriam*.

RESUMO

MATSUDA, Renan Hiroshi. **Sistema Robotizado para Estimulação Magnética Transcraniana Navegada.** 2022. 137 f. Tese (Doutorado Programa de Pós-graduação em Física Aplicada à Medicina e Biologia). Departamento de Física da Faculdade de Filosofia, Ciências e Letras de Ribeirão Preto, Universidade de São Paulo, Ribeirão Preto; 2022.

A estimulação magnética transcraniana (EMT) é uma técnica de estimulação cerebral não invasiva amplamente utilizada para investigar as funções do cérebro humano. Os sistemas de neuronavegação fornecem guia por imagem para procedimentos de posicionamento da EMT, conhecidos como EMT navegado (EMTn). O EMTn usa um dispositivo de rastreamento para monitorar o movimento da cabeça do paciente. O marcador de rastreamento de cabeça, ou ferramenta, deve permanecer estático durante todo o tratamento ou protocolo. Pequenas variações no marcador de cabeça ou no posicionamento da bobina de EMT podem causar mudanças não intencionais consideráveis nas respostas fisiológicas, comprometendo a confiabilidade e a reprodutibilidade da EMT. Robôs colaborativos têm sido usados para superar essas limitações de posicionamento da EMT. No entanto, o posicionamento robótico da bobina de EMT não é comum devido à baixa portabilidade, alto custo e plataformas de desenvolvimento de software de código fechado. Assim, o objetivo desta tese foi: 1) desenvolver um sistema robotizado para EMTn; 2) desenvolver um rastreador de cabeça *markerless* para EMT navegada. Na primeira parte, desenvolvemos e caracterizamos um sistema de controle em malha fechada combinando o posicionamento robótico eletrônico e físico do transdutor da EMT. Nossa nova plataforma de código aberto para posicionamento de bobinas de EMT robotizado é um passo importante para aumentar a precisão e confiabilidade dos procedimentos de EMT, facilitando o desenvolvimento de novas ferramentas e métodos para investigação cerebral, como a automação de mapeamentos motores. Em segundo lugar, desenvolvemos e caracterizamos o *MarLe*; uma nova estratégia de um rastreador de cabeça *markerless* para EMT navegada. *MarLe* usa técnicas de visão computacional combinadas com uma

câmera de baixo custo para estimar a pose da cabeça para sistemas de neuronavegação. *MarLe* melhora a confiabilidade da navegação, simplificando e reduzindo o tempo de protocolo de técnicas de intervenção cerebral, como a EMTn.

Palavras-chave: Neuronavegação. Estimulação magnética transcraniana. Instrumentação biomédica. Robôs colaborativos. Visão computacional.

ABSTRACT

MATSUDA, Renan Hiroshi. **Robotized System for Navigated Transcranial Magnetic Stimulation**. 2022. 137 f. Tese (Doutorado ¬ Programa de Pós-graduação em Física Aplicada à Medicina e Biologia). ¬ Departamento de Física da Faculdade de Filosofia, Ciências e Letras de Ribeirão Preto, Universidade de São Paulo, Ribeirão Preto; 2022.

Transcranial magnetic stimulation (TMS) is a non-invasive brain stimulation technique widely used to investigate human brain functions. Neuronavigation systems provide image guidance to TMS targeting procedures, known as navigated TMS (nTMS). nTMS uses a tracking device to monitor the patient's head movement. The tracking head marker must remain static during the entire treatment or experimental protocol. Small variations in the head marker or in the TMS coil positioning may cause considerable unintended changes in the physiological responses, compromising the TMS reliability and reproducibility. Moreover, collaborative robots have been used to overcome these TMS targeting limitations. However, robotic TMS coil positioning is not common due to poor portability, high cost, and closed-source software development platforms. Therefore, the aim of this thesis was: 1) to develop an open-source robotized system for nTMS; 2) to develop a markerless head tracker for navigated TMS. In the first part, we developed and characterized a closed-loop control system combining the electronic and physical robotic positioning of the TMS transducer. Our new open-source platform for robotized TMS coil positioning is an important step to increase the accuracy and reliability of TMS procedures, facilitating the development of new tools and methods for brain investigation, such as the automation of motor mappings. Second, we developed and characterized *MarLe;* a novel strategy of a markerless head tracker for navigated TMS. *MarLe* uses computer vision techniques combined with a low-cost camera to estimate the head pose for neuronavigation systems. *MarLe* improves the neuronavigation reliability, simplifying and reducing the time of brain intervention protocols, such as with nTMS.

Keywords: Neuronavigation. Transcranial Magnetic Stimulation. Biomedical Instrumentation. Collaborative robots. Computer Vision.

LIST OF FIGURES

LIST OF TABLES

LIST OF ABBREVIATIONS

2D	two-dimensional
3D	three-dimensional
ANOVA	analysis of variance
APB	abductor pollicis brevis
API	application programming interface
ASCII	American standard code for information
Cobots	collaborative robots
EEG	electroencephalography
E-field	electric field
EMG	electromyography
FPS	frames per second
M1	primary motor cortex
MEP	motor evoked potential
MRI	magnetic resonance imaging
mTMS	multi-locus transcranial magnetic stimulation
nTMS	navigated transcranial magnetic stimulation
SD	standard deviation
TCP	tool center point
TMS	transcranial magnetic stimulation
VCU	video camera unit

SUMMARY

1. Theory And General Concepts

1.1. NEURONAVIGATION

Neuronavigation systems were developed to assist neurosurgeons in performing highly complex surgeries. By increasing the precision of surgical procedures, neuronavigation helps in preserving eloquent regions and thus improving the patient prognosis (HAASE, 1999; ORRINGER; GOLBY; JOLESZ, 2012; ROSLER *et al.*, 2014).The location of neuronal structures is given through the three-dimensional reconstruction of brain images from computed tomography or magnetic resonance imaging (MRI). The working principle of a neuronavigation system is given by a mathematical model that describes the real coordinate system (patient's head), to the virtual coordinate system, i.e., to the coordinate system of tomographic images (GRUNERT *et al.*, 2003). The interaction between the surgical instruments and the neuronavigation system is established by a tracking device. The tracking device provides the position and orientation of sensors or markers attached to instruments and to the patient's head. The markers fixation must remain static during the entire brain intervention.

Tracker devices are classified according to their physical principle of operation, divided into three types: visible light, electromagnetic, and infrared. The visible light trackers have stereoscopic cameras that detects visual patterns. Once located, through internal triangularization algorithms, the position and orientation of each marker is estimated. The wireless capability in optical tracking gives the system greater versatility. However, the planar markers require to be always facing towards the camera lenses. Electromagnetic devices rely on low frequency fields produced by transmitter antennas, which are detected by antennas on a stationary receiver. This excitation at the receiver provides the necessary data to estimate its position and orientation relative to the transmitter. Electromagnetic trackers have a wide operating field and there is no concern about the positioning between the emitter and the receiver. However, this tracker technology is highly susceptible to interference from the environment, for example, metallic materials around the device affect the electromagnetic fields, resulting in estimation inaccuracies of the sensor position and orientation. Infrared tracking uses a stereoscopic camera together with an infrared emitter.

The tracker detects retroreflective markers pattern attached to a tool or object. Like visible light trackers, the infrared system is wireless, but requires that the retroreflective markers are always within the field of view of the stereoscopic camera. The precision and accuracy of neuronavigation are directly linked to the tracking technology used. Each scenario, which will be carried out with the neuronavigation, has an optimal tracking device. Factors such as the geometry of the room, the number and arrangement of other equipment in the room, and the lighting will affect the tracker accuracy.

The main factors that influence the accuracy of neuronavigation are the co-registration method, the technical specifications of the tracking devices, and the image parameters(STEINMEIER *et al.*, 2000). The accuracy error of neuronavigation systems is given by the sum of all factors that influence the technique. A neuronavigation system is expected to have an upper limit of accuracy error of 3 to 4 mm (KUEHN *et al.*, 2008).

Neuronavigation has been used to locate brain structures in non-invasive brain interventions, such as in transcranial magnetic stimulation (TMS) (BOROOJERDI *et al.*, 1999; JULKUNEN, 2014; LEFAUCHEUR, 2010); electroencephalography (EEG) (CHIARELLI *et al.*, 2015; MURTHY *et al.*, 2014); magnetoencephalography (LITTLE; BOE; BARDOUILLE, 2014) and near-infrared spectroscopy (TSUZUKI; DAN, 2014).

So far, few alternatives for neuronavigation systems have been presented with the proposal of free distribution and open source, among the alternatives are SlicerIGT (FEDOROV *et al.*, 2012) and InVesalius Navigator (SOUZA *et al.*, 2018a). SlicerIGT was conceived by David Gering in 1999 (GERING *et al.*, 2001) and has been developed mainly by researchers at the Massachusetts Institute of Technology and Brigham and Women's Hospital at Harvard Medical School. In turn, InVesalius Navigator was initially proposed in 2008 by André Peres and Victor Hugo Souza (PERES *et al.*, 2010; SOUZA *et al.*, 2018a), and has been developed at the Physics Department of the University of São Paulo, in partnership with the Department of Three-Dimensional Technologies, from the Renato Archer Information Technology Center, in Campinas (AMORIM *et al.*, 2015). Both programs are open-source, cross-platform, with tools for viewing and processing medical images, and an interface for neuronavigation with multiple

spatial trackers. Among the peculiarities of each one, we highlight the large number of extensions for MRI processing developed for SlicerIGT and the active community that frequently contributes to the development of new functionalities. In contrast, InVesalius Navigator is translated into 22 languages and has specific tools for TMS neuronavigation and EEG experiments.

1.2. TRANSCRANIAL MAGNETIC STIMULATION

TMS is a valuable tool for non-invasive brain stimulation (BARKER; JALINOUS; FREESTON, 1985; HALLETT, 2000; MATSUDA *et al.*, 2019; WASSERMANN; ZIMMERMANN, 2012). Magnetic pulses generated by a coil positioned on the scalp depolarize neurons by TMS-induced electric fields in the cortical tissue. The coil positioned over the primary motor cortex (M1) generates action potentials that travel through the corticospinal tract, reaching the spinal motor neurons and, finally, the target muscle. The motor evoked potential (MEP) is the myoelectric activity produced at the target muscle in response to the magnetic pulse. The MEP is commonly acquired by surface electromyography (EMG) (ROSSINI; ROSSI, 1998; WASSERMANN *et al.*, 1992).

The physical principle of TMS follows the electromagnetic laws of induction (WASSERMANN; ZIMMERMANN, 2012). According to the Biot-Savart law (Equation 1) the intensity of the magnetic field is directly proportional to the applied current, i.e., the greater the current the greater is the magnetic field intensity. However, the activation source is given by the electric field induced in the tissue. According to Faraday's law of induction (Equation 2), the electric field (E-field) is proportional to the variation of the magnetic field. Therefore, TMS machines are conceived such that a high current is conducted through the coil in a short–time interval. Biological tissues have a magnetic permeability equivalent to vacuum and the magnetic field penetrates through the scalp and skull inducing an electric field on the conductive cortical surface. In turn, the electric field influences the charged particles in the conducting medium of the cerebral cortex,

for example, neuron membranes, creating a current flow, as demonstrated in Equation 3, and consequently depolarizing the underlying neurons.

$$\vec{B} = \frac{\mu_0}{4\pi} i \oint_C \frac{d\vec{l} \times \hat{r}}{r^2} \quad (1)$$

$$\vec{\nabla} \times \vec{E} = -\frac{\partial \vec{B}}{\partial t} \quad (2)$$

$$\vec{J} = \sigma \vec{E} \quad (3)$$

where $\vec{E}$ is the electric field, $\vec{B}$ the magnetic field, $\vec{J}$ the current density and σ the tissue conductivity.

The simplified TMS circuit is composed of three components: a capacitor, an inductor (stimulation coil), and a thyristor for switching. The intensity of the TMS magnetic field is on the order of 2 T, but it depends on the equipment quality, coil geometry and the stimulation intensity. The stimulation intensity is personalized for each participant (or volunteer), and it is defined by finding the hotspot and the resting motor threshold for a given muscle or set of muscles. The hotspot is the cortical site below the center of the coil that results in an MEP with maximum amplitude for a single TMS pulse (SÄISÄNEN *et al.*, 2008; WASSERMANN *et al.*, 1992). The resting motor threshold is defined as the lowest stimulus intensity capable of evoking potentials greater than a certain amplitude (CONFORTO *et al.*, 2004). The EMG electrodes placement requires caution, electrodes displacements can result in distinct responses in resting motor thresholds (GARCIA *et al.*, 2020; GARCIA; SOUZA; VARGAS, 2017).

To obtain the desired response, TMS application requires proper adjustment of the coil positioning. The coil positioning is a crucial component since the technique involves magnetic and electric fields direction of propagation (PELL; ROTH; ZANGEN, 2011; ROTH; BASSER, 1990; SOUZA *et al.*, 2022). It is well known that the optimal angle of the stimulation coil, for motor mapping studies, is 45º in relation to the anteroposterior axis (BRASIL-NETO *et al.*, 1992;

SOUZA *et al.*, 2018b), therefore, monitoring the position and orientation of the coil is essential for an accurate stimulation session.

To assist the TMS coil positioning, a combination of neuronavigation and TMS is used, called navigated transcranial magnetic stimulation (nTMS). This technique allows real-time monitoring of the TMS coil based on brain imaging. The nTMS employs the anatomical differences between individuals for positioning the coil on the investigated site. Neuronavigation also allows adjusting the optimal orientation of the stimulation field in relation to the brain structures (BASHIR *et al.*, 2013; CINCOTTA *et al.*, 2010; KALLIONIEMI; KÖNÖNEN; JULKUNEN, 2015). nTMS allows the delimitation of a target muscle representation area on its cortical surface, this technique being called motor mapping (ROMERO et al., 2011; (ROMERO *et al.*, 2011; WASSERMANN *et al.*, 1992) et al., 1992b). Motor mapping is used in studies of brain physiology to assess damage to the motor cortex and corticospinal tract (ROSSINI *et al.*, 2015; ZIEMANN, 2000), and to assess the functional representation of muscle in the brain (ETTINGER *et al.*, 1998; TARDELLI *et al.*, 2022).

However, there is a lack of low-cost and easily portable neuronavigation systems to support the application of TMS in clinical and research routines, which highlights the importance of open source neuronavigation, such as InVesalius Navigator (SOUZA *et al.*, 2018a). New technological developments have been presented to increase the performance, accuracy, and versatility of TMS, such as the multi-locus TMS (mTMS)(KOPONEN; NIEMINEN; ILMONIEMI, 2018; NIEMINEN *et al.*, 2022; SOUZA *et al.*, 2022). mTMS is an outstanding technology able to change the stimulation spot without physically moving the transducer. mTMS utilizes multiple overlapping coils (transducer) to generate a unique stimulation pattern by combining the produced electric field from each coil in the transducer. This is a critical improvement compared to conventional TMS. However, the mTMS transducer is heavy (around 5 kg) and manual positioning can be challenging.

More details and information about TMS are presented in Appendix C.

1.3. COLLABORATIVE ROBOTS

The first robotic system was introduced for industrial environments to automate and improve the accuracy of laborious tasks such as welding and assembly. Robotic systems cater to tasks, with a superior level of strength, repeatability, and accuracy, that are dangerous to the worker's health. However, industrial robots are not allowed to interact with the operator due to safety and technological issues. The development of new security mechanisms allowed the introduction of collaborative robots (cobots). The cobots can safely operate side by side with humans, unlike traditional industrial robots (PESHKIN; COLGATE, 1999). The cobots can operate not only for industrial purposes but also for medical applications for example (HAIDEGGER, 2019).

The effect of TMS on the brain is highly specific, millimeter-order variations in coil placement evoke substantially different responses (NIEMINEN *et al.*, 2019). The manual coil positioning even when assisted by neuronavigation may depend on the user’s expertise. In addition, the patient performs small involuntary movements, even with a head support. If the patient moves, the stimulator must be repositioned. Therefore, cobots have been used to aid positioning of the TMS coil (MATTHÄUS *et al.*, 2006; NOCCARO *et al.*, 2021; PENNIMPEDE *et al.*, 2013). Robotic positioning also enables the development of new methods for automated motor mapping (GIUFFRE *et al.*, 2021; GRAB *et al.*, 2018). The control of the TMS robotic positioning can be done be by a feedback closed-loop system (WAN ZAKARIA, 2012; WAN ZAKARIA; TOMARI; NGADENGON, 2016).

A closed-loop system is a set of mechanical or electronic devices that automatically regulate a variable to the desired state without human interaction. An example of a closed loop system, from our daily life, is the inverter air conditioning. The sensors measure the ambient air temperature and then adjust the compressor, by controlling its speed, to the level necessary to reach the desired temperature. Closed-loop systems are designed to automatically reach and maintain the desired condition (output condition) by comparing it to its current condition (actual condition). The comparison is made through an error signal, which is the difference between the reference output and input. For the robotized

TMS coil positioning, the error signal is provided by the neuronavigation TMS guide positioning, i.e., the required offset to reach the desired TMS target.

However, the combination of nTMS and robotic arms is still not commonly used by the clinical and scientific communities due to three main factors. The first is low portability, i.e., the systems are fixed and cannot be transported between rooms and clinics. The second factor is the high cost of commercial equipment, and the third factor is that commercial navigation programs are closed, making it difficult for new tools to be developed.

1.4. OBJECTIVES AND THESIS ORGANIZATION

The objective of this thesis is to develop a novel autonomous TMS positioning system by combining the physical cobot coil positioning with a fast electronic control of the E-field provided by the multi-locus TMS. Second, we developed *MarLe*; the first markerless head tracker for navigated TMS capable of eliminating the use of a sensor attached to the patient's head.

Chapter 1 introduces the theory and general concepts used in the thesis. In chapter 2 describes the robotized TMS positioning system and the third chapter depicts the markerless head tracker. Lastly, our results and conclusions are summarized in chapter 4. The three appendices contain the studies of which I contributed during my doctoral thesis: “Forearm and hand muscles exhibit high coactivation and overlapping of cortical motor representations”, “Motor potential evoked by transcranial magnetic stimulation depends on the placement protocol of recording electrodes: a pilot study”, and “Estimulação magnética transcraniana: uma breve revisão dos princípios e aplicações”.

2. A ROBOTIC OPEN-SOURCE PLATFORM FOR NAVIGATED TRANSCRANIAL MAGNETIC STIMULATION

2.1. INTRODUCTION

TMS is a non-invasive brain stimulation technique widely used to probe human brain function. Small variations in the positioning of the stimulator cause variations in the evoked responses in the brain (HALLETT, 2000). Neuronavigation systems have been used to increase the precision and accuracy of TMS targeting. However, when the coil is manually positioned, placement inaccuracies may occur. In addition, the stimulator must be manually repositioned every time the patient moves. Cobots have also been used to improve the reproducibility and accuracy of the TMS coil placement (GOETZ *et al.*, 2019). However, the robotic TMS coil positioning is not widely used due to low portability, high cost, and closed-source development platforms.

Also, the target repositioning of the conventional robotic TMS is limited to the robot velocity and cannot perform rapid change (in the millisecond time scale) of the stimulation spot. mTMS can change the stimulation spot without physically moving the transducer. However, the mTMS transducer has a maximum range of 15 mm around the center of the transducer. The manual positioning can be challenging due to the heavy weight of the transducer (around 5 kg).

Therefore, we developed a novel open-source platform that combines accurate robotic positioning with mTMS fast electronic control of stimulation spots. We characterized our platform and demonstrated the automation of a TMS motor mapping. This combination of techniques offers unprecedented possibilities to study the brain with TMS and certainly will open new windows to study this important organ and generate important questions and data to be studied and modelled by physical and mathematical tools.

2.2. MATERIALS AND METHODS

We used the cobot Elfin E5 (HAN'S Robots, China). Elfin E5 has 6 rotation joints, a 5 kg payload, 800 mm maximum operation range, and a repeatability accuracy of ± 0.05 mm. The algorithm to perform the robotized TMS coil

positioning was defined as robot control. The robot control was fully developed in Python 3.8. The main requirements are the following libraries:

- *Socket*, for communication protocols;
- *NumPy*, for matrices operations;
- *OpenCV*, for filtering;
- *Threading*, for parallel processing.

All the code is available at https://github.com/biomaglab/Robot_TMS.

2.2.1. ROBOT CONTROL COMMUNICATION ARCHITECTURE

The robot control was developed to operate with InVesalius (AMORIM *et al.*, 2015). InVesalius and the robot control can be run on the same or different computers, bringing flexibility to the user and greater stability and reliability to the system. The communication between the robot control and the neuronavigator is made by a middle layer server using WebSocket protocol. The middle layer server receives messages from InVesalius, which are then transmitted to the robot control. The middle layer is bidirectional, and the data from the robot control is also transmitted back to InVesalius. InVesalius provides the tracker device coordinates, i.e., the coil and head pose, the TMS target, and the targeting feedback, i.e., the required translation and rotation offset to reach the TMS target. Figure 1 illustrates a summary of the communication architecture. Extra information about the exchanged data can be found at https://github.com/biomaglab/Robot_TMS/blob/main/main_loop.py.

Figure 1: Flowchart of the communication architecture of InVesalius and robot control. InVesalius sends the tracker coordinates and the required offset to reach the target. The robot control sends the cobot coordinates and status messages to feedback to the InVesalius graphical user interface.

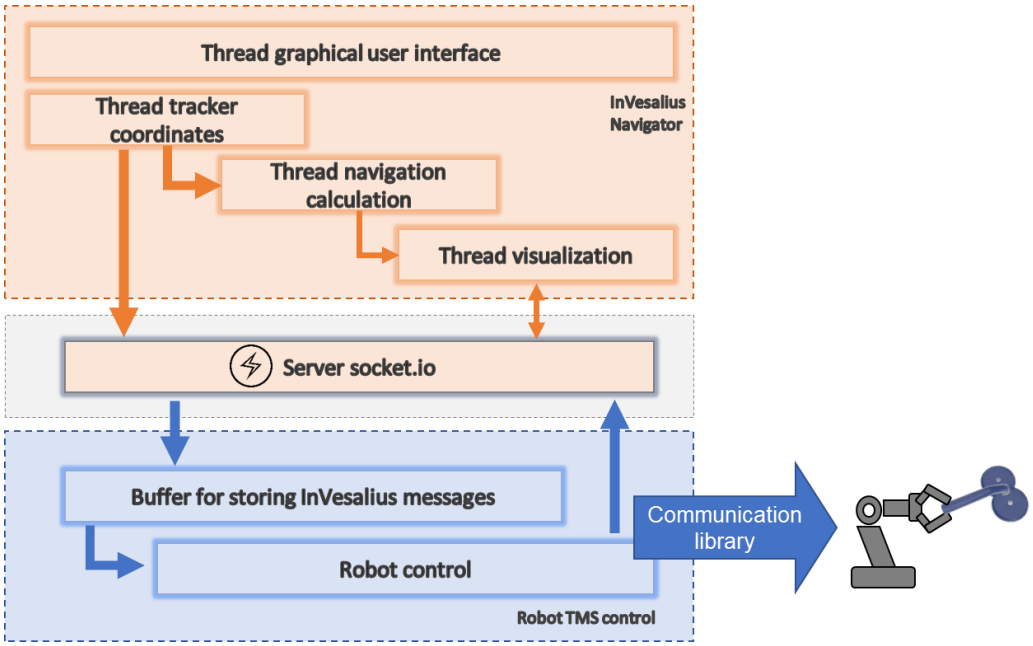

Elaborated by the author

We developed a Python library to communicate with the cobot Elfin E5. We used the Hans Robot communication protocol interface. The communication architecture is based on transmission control protocol/internet protocol (TCP/IP). Elfin operates as a server and the robot control as a client, i.e., the robot control sends messages as a request for Elfin. The message format is composed by the name of the function followed by input parameters. The commands and replies are in American standard code for information interchange (ASCII) format. However, Elfin's supports only one message at time, discarding the consecutives messages, which were considered in the robot control algorithm. The Elfin communication Python library can be found at:

https://github.com/biomaglab/Robot_TMS/blob/main/robot/control/elfin.py.

2.2.2. COBOT–INVESALIUS COREGISTRATION

A coregistration between the cobot and InVesalius is required to estimate the transformation matrix that binds both coordinate systems. The coregistration consists in acquiring simultaneously the coil pose in the cobot and tracker coordinate system. The cobot provides the coordinate of the center of the end-

effector. Then, a translation matrix ($TCP_{end-effector}^{coil}$) is applied to reach the tool center point (TCP), i.e., the center of the TMS coil. The tracking device provides the coordinate of the center of the marker fixed on the coil. Similar to the cobot, we applied a transformation matrix (TCP_{marker}^{coil}) to translate between the collected marker coordinate to the center of the TMS coil.

We developed a dedicated graphical user interface to perform the coregistration between the cobot and tracker coordinate systems. We experimentally defined that the registration requires, for an accurate and redundant transformation, at least 500 paired coil poses. To solve the given problem in terms of mathematical operations from paired poses set, we used a closed-form solution through the equation:

$$\mathrm{T}_{cobot}^{coil} \; M_{tracker}^{cobot} = M_{tracker}^{cobot} \; \mathrm{T}_{tracker}^{coil} \tag{4}$$

T_{cobot}^{coil} and $T_{tracker}^{coil}$ are given by:

$$T_{cobot}^{coil} = T_{cobot}^{end-effector} \; TCP_{end-effector}^{coil} \tag{5}$$

$$T_{tracker}^{coil} = T_{tracker}^{marker} \; TCP_{marker}^{coil} \tag{6}$$

where $T_{cobot}^{end-effector}$ and $T_{tracker}^{marker}$ are homogeneous transformation matrices from the cobot basis to the cobot end-effector and from the tracker device to the coil marker, respectively.

Based on Equation 4, we used the 500 pairs of coil poses ($\mathrm{T}_{cobot\ 500x6}^{coil}$ and $\mathrm{T}_{tracker\ 500x6}^{coil}$) to find the coregistration matrix $M_{tracker}^{cobot}$ through a least square solution method. Figure 2 illustrates the transformation method. Once the coregistration is done, the cobot base and the tracker device must stay static during the TMS session. The final step is the conventional neuronavigation coregistration, i.e., to find the transformation matrix between the tracker device and the anatomical image $M_{tracker}^{image}$. Thus, the matrices $M_{tracker}^{cobot}$ and $M_{tracker}^{image}$establish the connections between the anatomical image, the tracking device, and the cobot coordinates systems. The robot control requires both

matrices to perform the TMS coil positioning based on anatomical images. The transformation between the InVesalius TMS target to the cobot TMS coil positioning is through the following equations:

$$M_{InV}^{tracker}{}_{target} = M_{tracker}^{image\ -1}\ P_{InV_{target}} \quad (7)$$

Given a TMS target defined in InVesalius $P_{InV_{target}}$ we found the transformation matrix to the tracker coordinate system $M_{InV}^{tracker}$. Then, the cobot position and orientation to reach the TMS target ($P_{cobot_{target}}$) is given by:

$$P_{cobot_{target}} = M_{tracker}^{cobot}\ M_{InV}^{tracker}{}_{target} \quad (8)$$

Figure 2: Illustrated flowchart of the coregistration method between robot control and InVesalius. TCP is an acronym for tool center point. The first step is to create the TCP, on the bottom center of the TMS coil, for the robot and for the tracking marker. Then, the coregistration matrix is estimated by 500 random pairs of coil poses around the operation area. The final step is to perform the conventional neuronavigation coregistration, i.e., the transformation matrix between the patient's head with the respective neuroimage.

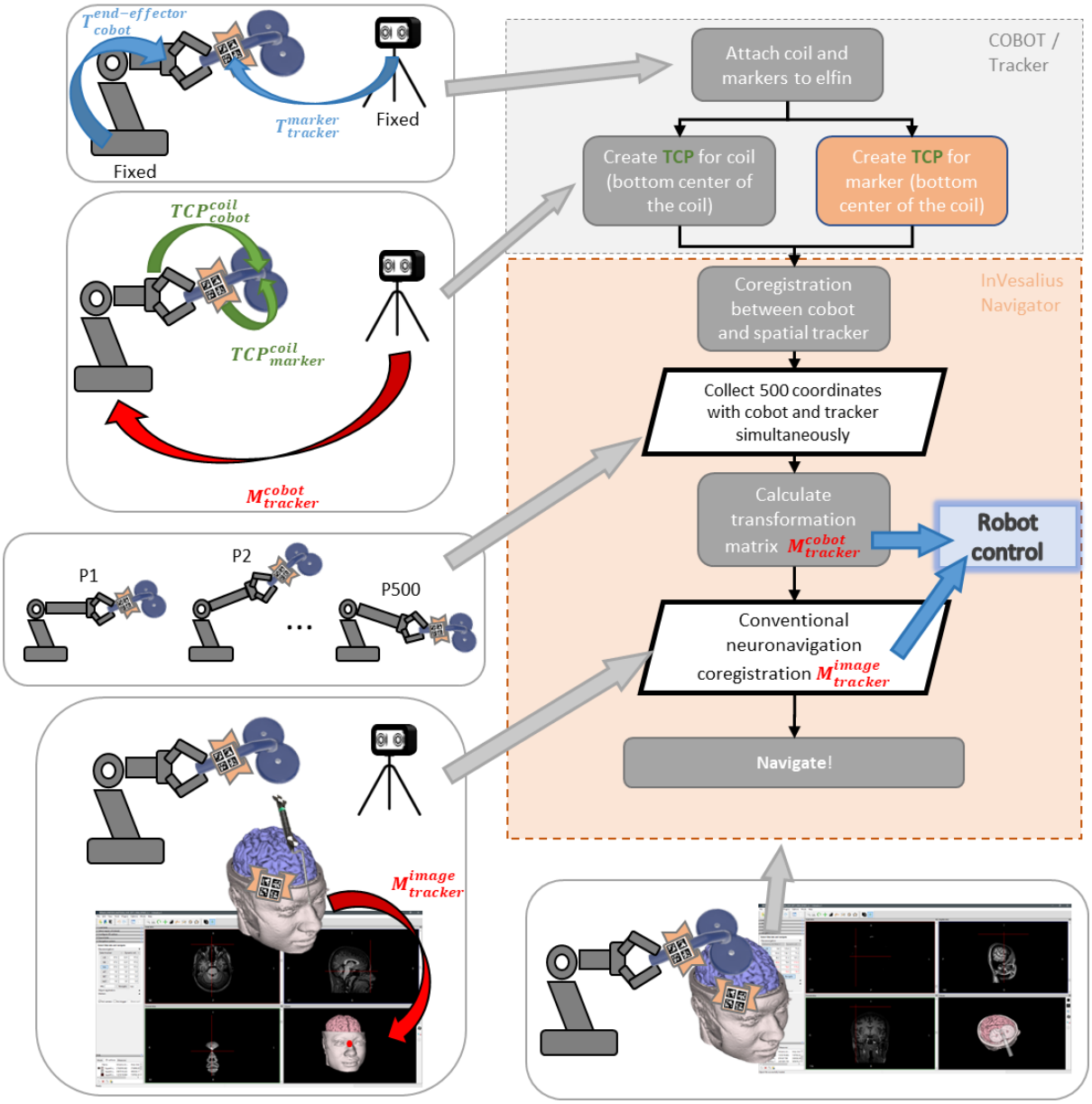

Elaborated by the author

2.2.3. ROBOTIC CLOSED-LOOP CONTROL

Figure 3 illustrates the closed-loop control. InVesalius provides the graphical user interface to the cobot and the targeting feedback shown in Figure

4. The closed-loop control requires the input of the TMS target location, from InVesalius. Based on Equation 8, the robot control estimates the cobot position and orientation to move the coil to the desired target. If the patient moves, the robot control can detect the disturbance and a feedback signal is provided to perform the head movement compensation. Once the cobot reaches the target, within a range of 5 mm/5°, the robot control starts to fine tune the positioning. The tuning uses the targeting feedback from the InVesalius positioning guide. The targeting feedback is the coil offset to a precise position at the target, i.e., InVesalius provides the displacement between the current position to the target. The head movement compensation is given by following equations:

given,

$$M_{head\ target}^{cobot} = M_{tracker}^{cobot}\ P_{tracker-head_{target}} \quad (9)$$

where $P_{tracker-head_{target}}$ is the target head position in the tracker coordinate system. $\mathrm{M}_{head\ \mathrm{target}}^{cobot}$ is the transformation matrix from the head position to the cobot coordinate system. If the patient head moves, we have a new transformation matrix:

$$M_{head\ new}^{cobot} = M_{tracker}^{cobot}\ P_{tracker-head_{new}} \quad (10)$$

Based on the $P_{cobot_{target}}$, we find the transformation matrix M_{cobot}^{target}, i.e., the TMS scalp target in the cobot coordinate system,

$$M_{cobot}^{target} = M_{head\ target}^{cobot\ -1}\ P_{cobot_{target}} \quad (11)$$

Using $M_{head\ new}^{cobot}$ and M_{cobot}^{target}, we have the new cobot position:

$$P_{cobot_{new}} = M_{head\ new}^{cobot}\ M_{cobot}^{target} \quad (12)$$

Appling Equation 9 and Equation 10, we find the general equation to perform the head move compensation:

$$P_{cobot_{new}} = M_{tracker}^{cobot}\ P_{cobot_{new}}\ (M_{tracker}^{cobot}\ P_{head_{target}})^{-1}\ P_{cobot_{target}} \quad (13)$$

Figure 3: Closed-loop control of the TMS coil positioning. The robot control (blue box) set a cobot target coordinate and detects and corrects head movements. The orange boxes are the user interface (InVesalius) with the robot control.

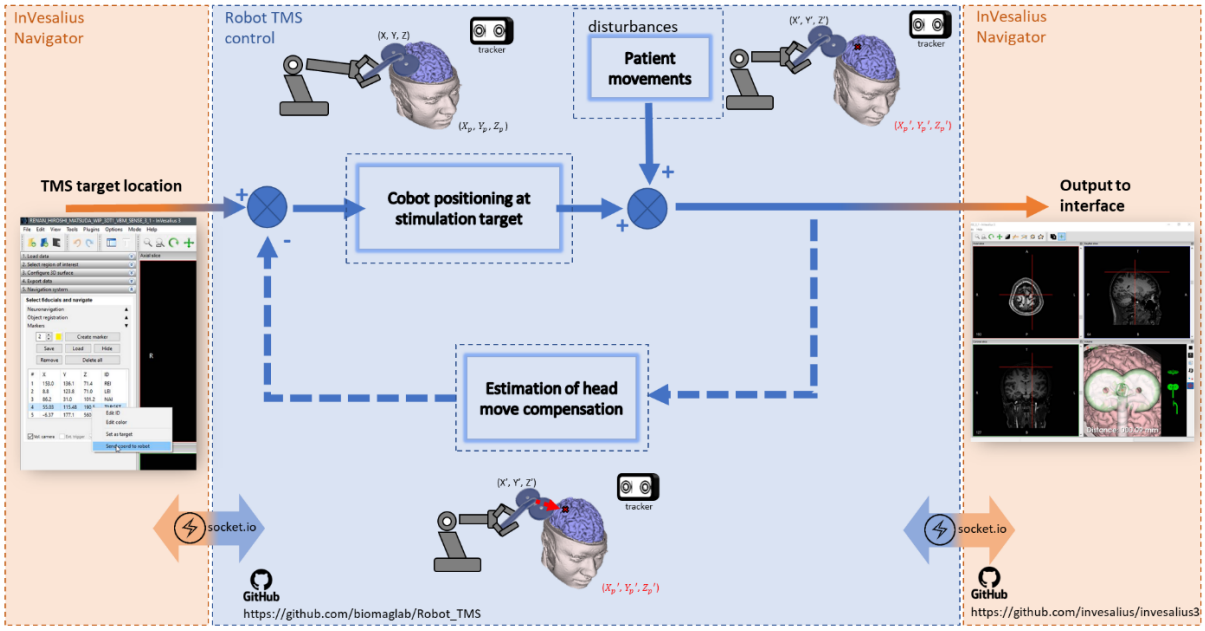

Elaborated by the author

Figure 4: InVesalius Navigator user interface (on the left) guiding the cobot TMS coil placement (on the right).

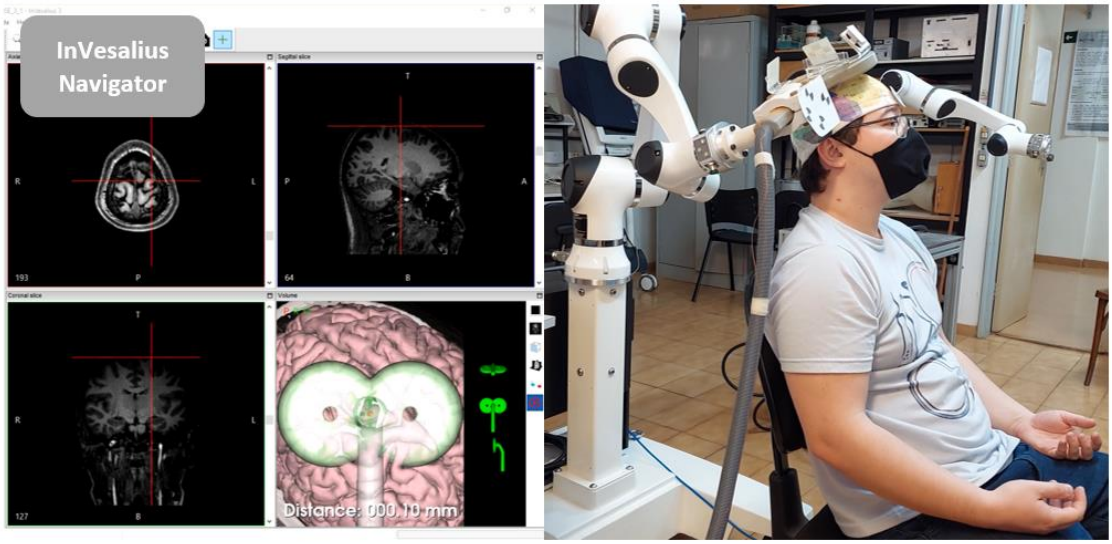

Elaborated by the author

2.2.4. SAFETY LAYERS

We developed five software safety layers: 1) the robot must perform movements only if the tracking marker fixed to the patient's head is visible. 2) A Kalman filter for the patient's head coordinates prevents sudden fluctuations of the tracking device. 3) A head velocity estimation to allow the robot movement only if the head movements are slower than 5 mm/s. 4) The robot must position the stimulator only inside a pre-defined working space. 5) Restricted control of the trajectory for new placements. If the distance for movement is greater than 10 cm, the robot makes an arc path, avoiding collisions with the head. The robot performs head displacement compensation only if all the five conditions are accepted, guaranteeing that the coil is positioned safely at the target spot. The flow diagram is illustrated in Figure 5.

Besides the conditions for moving the robot, we must measure the applied force of the coil on the scalp surface. Therefore, a force and torque sensor, FT 300-S (Robotiq, Canada), was coupled to the robot, Figure 6. The sensor provides the force applied in three directions and the corresponding torque. The force control has three conditions; 1) a threshold up to 5 N; the robot immediately stops the head move compensation. 2) For a contact force higher than 30% of the initially applied force, the robot performs a linear movement contrary to the head position. The robot continues to retreat until the applied force is 30% lower than the initial force, ensuring safety in relation to the pressure exerted by the coil on the patient's head.

Figure 5: Flow diagram of the security layers from the robot control

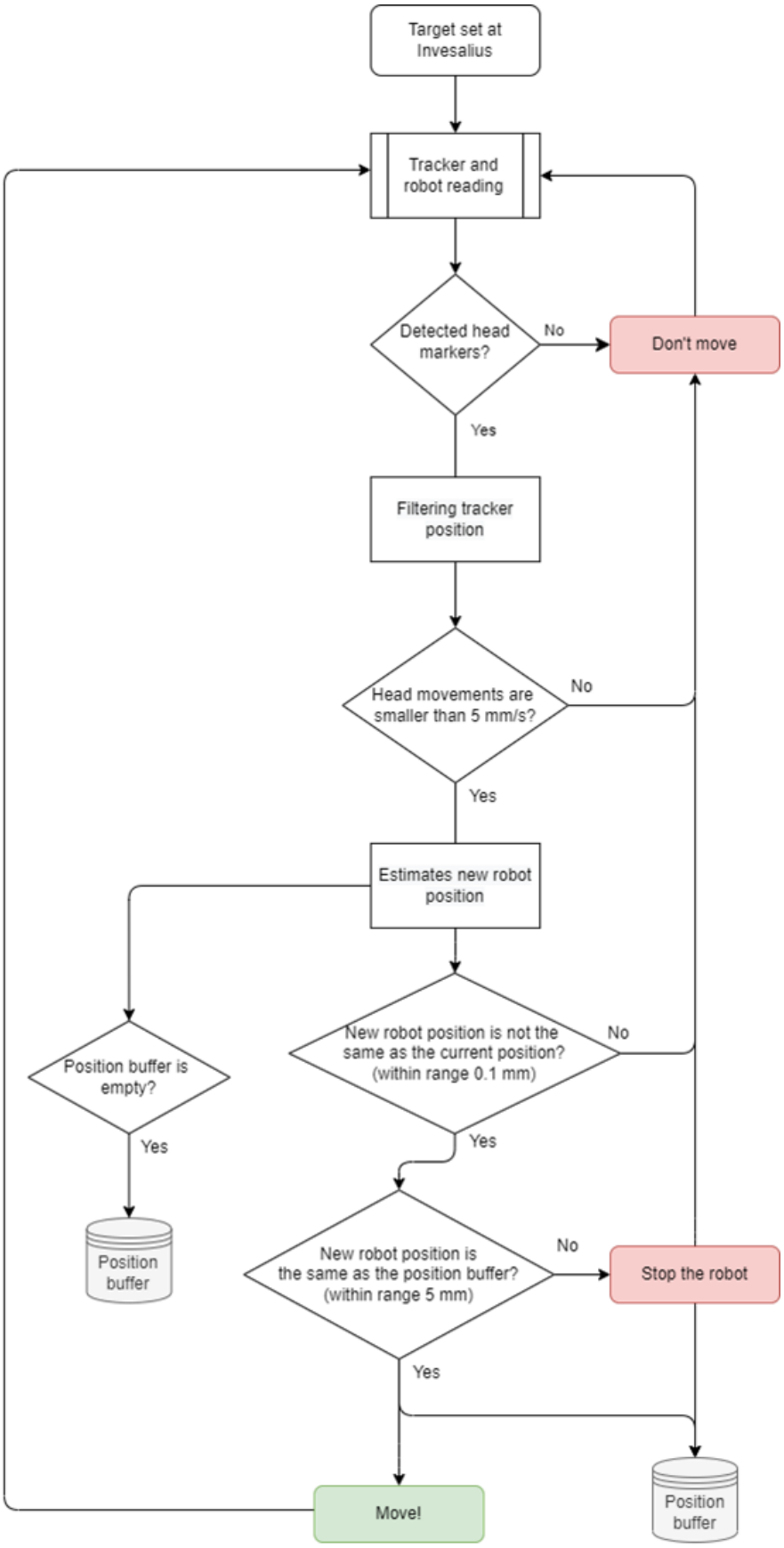

Elaborated by the author

Figure 6: Left: Force and torque sensor; Center: Sensor coupling with cobot end-effector; Right: mTMS transducer attached to the sensor and the robot end-effector.

Elaborated by the author

2.2.5. CHARACTERIZATION

We validated the control system's stability and accuracy in repositioning the TMS coil on a defined target on polystyrene foam dummy head. To measure the stability, we recorded the coil pose for 15 minutes with an acquisition rate of 3 Hz, resulting in 2700 coil poses. The accuracy in repositioning on the TMS target was divided into two experiments:

1) We defined a TMS target (approximately over a region representing the motor cortex) and a home position (arbitrary location far away from the dummy head). Then, we alternated the cobot position 15 times between the target and home position. We used InVesalius, connected to the tracking device Polaris Vega VT (Northern Digital Inc., Canada), to record the coil pose when the target was reached. We repeated the experimental protocol for the robotic and manual positioning. We used the Montreal Neurological Institute average MRI (EVANS *et al.*, 1993), based on 152 MRIs, to perform the neuronavigation. The fiducials, right and left tragus and nasion were collected for the coregistration.

2) We assessed the accuracy in repositioning through the induced E-field. We reproduced the previous experimental protocol but instead of using a dummy head, a TMS calibrator was used to measure the E-fields induced by the TMS coil, the calibrator automates measuring the E-field in a spherically symmetric conductor approximating the human head (NIEMINEN; KOPONEN; ILMONIEMI, 2015). The E-field was mapped on 100 points covering a 15-mm radius circular region from the center of the TMS coil. We used the figure of eight coil from the mTMS transducer. The neuronavigation, connected to the tracking device

OptiTrack (NaturalPoint, Inc., USA), was performed with a phantom MRI with a similar dimension (11 x 15 x 17 cm) to the calibrator (Figure 7). The phantom MRI is composed of a set of 180 images generated in MATLAB 2022a (MathWorks Inc., USA). The images represent a conventional 3D T1-weighted structural MRI, with a matrix of 256 x 256 x 180 and a pixel size of 1x1x1 mm^3. The collected fiducials were the right and left bottom part, and the front top middle of the calibrator stand, we collected the corresponded fiducial in the phantom MRI, Figure 8 and Figure 9. The measurements were repeated three times.

Figure 7: InVesalius screenshot with a simulated MRI of the TMS calibrator. The dots are spaced by 1 cm.

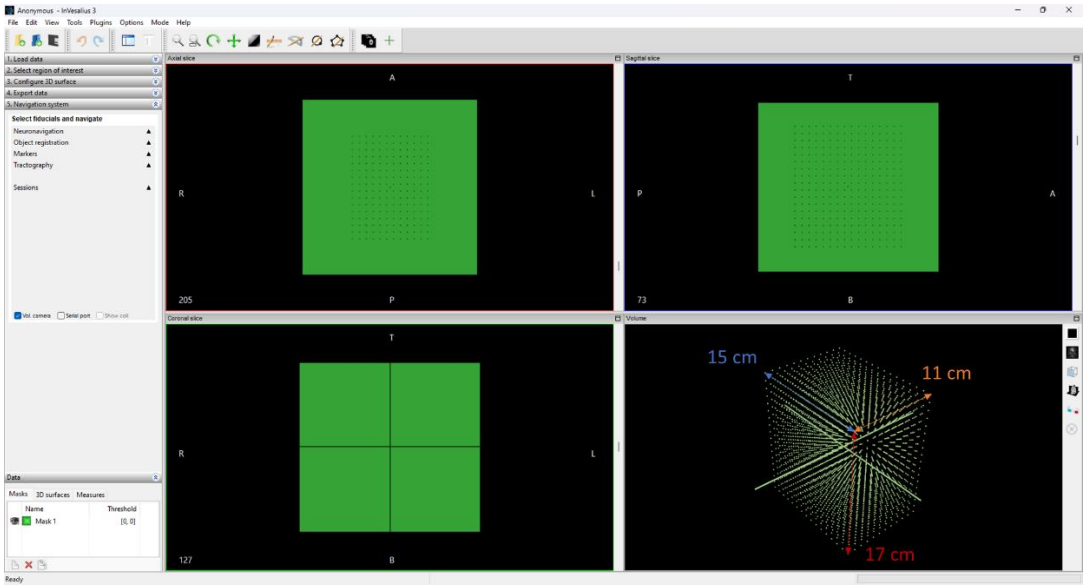

Elaborated by the author

Figure 8: Simulated MRI of the TMS calibrator; The yellow spheres are the fiducial landmarks for the neuronavigation coregistration.

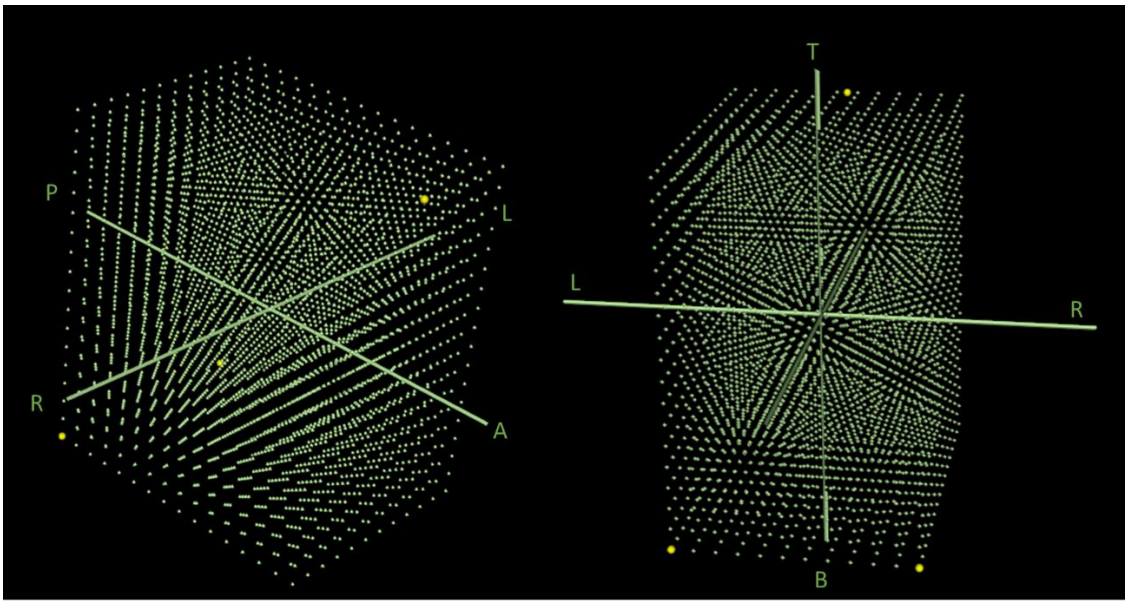

Elaborated by the author

Figure 9: TMS calibrator. The three yellow stars are the fiducials landmarks for the neuronavigation coregistration.

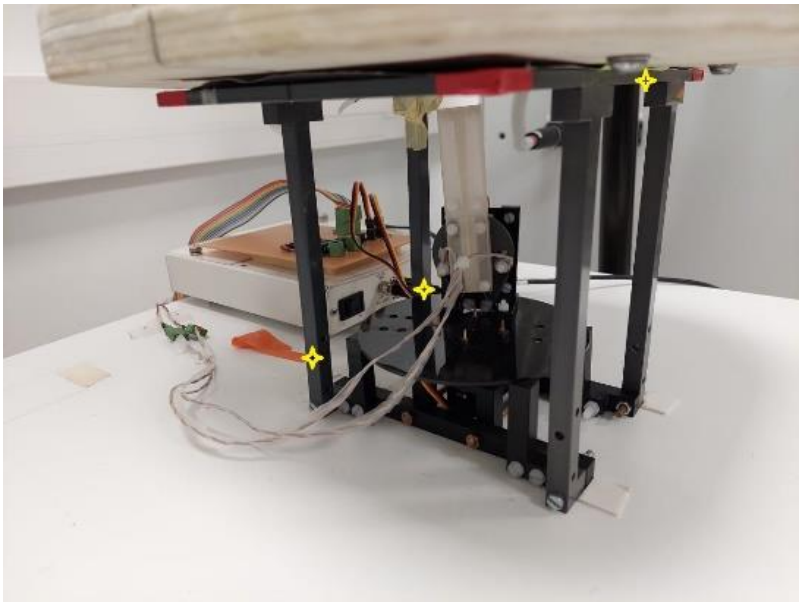

Elaborated by the author

2.2.6. DATA ANALYSIS

The stability was defined as the standard deviation (SD) of the difference of the translation and three orientation vectors from the target. The accuracy in

repositioning on the TMS target was defined as the Euclidean distance between the fixed TMS coil target and the measured final positions. The accuracy in repositioning on the TMS target, evaluated trough the induced E-field, was assessed by the coordinates of the centroid of 70% of the E-field maximum intensity area. The centroid comparison was performed through the combinations without repetition of the 15 E-field centroids taking the subtraction between two centroids, i.e., each centroid was subtracted by the all-other centroids, without repetition, resulting in 105 combinations. The data variability of the repositioning accuracy was quantified by the average absolute deviation (AAD), Equation 14.

$$AAD = \frac{1}{n}\sum_{i=1}^{n} |x_i - \bar{x_i}| \quad (14)$$

The stability and the repositioning accuracy of rotation angles were assessed with a one-way analysis of variance (ANOVA). The comparison between the robotic and the manual repositioning of the difference to the target was assessed with a two-way ANOVA. Tukey HSD post-hoc multiple comparisons were performed for all analyses. The software R 4.2 (R Core Team, Austria) was used for all statistical analysis and the significance threshold set at 0.05.

2.2.7. ROBOTIZED MULTI–LOCUS TRANSCRANIAL MAGNETIC STIMULATION

The integration of the electronic positioning, given by the mTMS, and the physical positioning of the mTMS transducer, given by the robot control, was implemented in InVesalius, Figure 10. The communication between InVesalius and the mTMS is via an application programming interface (API). InVesalius works as a bridge between robot control and mTMS; The robot control sends a message to InVesalius and then InVesalius processes and forwards the message to mTMS.

Figure 10: Robotized mTMS positioning guided by InVesalius

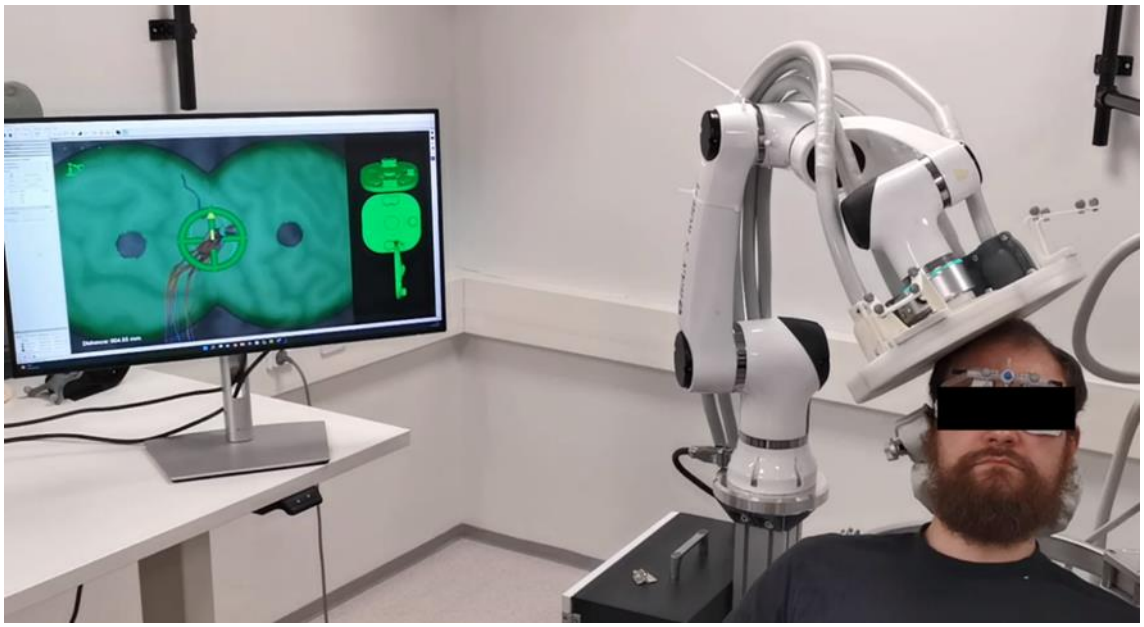

Elaborated by the author

First, we verified the electromagnetic interference of the cobot in the magnetic field produced by the mTMS transducer. We used an mTMS transducer with 5 coils (NIEMINEN et al., 2022). We characterized the induced E-field produced by each of the 5 mTMS coils individually, Figure 11. The induced E-field was measured along 250 points using the TMS calibrator, covering a 20-mm radius from the center of the mTMS transducer. The measurements were performed with and without the cobot. We used a wood stand to support mTMS transducer on top of the calibrator, Figure 12. The mTMS transducer position did not change for the measurements with and without the robot, due to the wood stand, we first measured with the cobot, and then we decoupled the mTMS transducer and moved the cobot away from the transducer.

Figure 11: Coils windings. The coils are assembled on the top of each other. The coil (a) is the closest to the scalp, and the coil (b) is the furthest from the scalp. (f) The 5-coil mTMS transducer. Adapted from (NIEMINEN *et al.*, 2022). The mTMS transducer present in (f) is the newest model developed. The coil windings (a) to (e) are from the previous model. However, the windings patterns are the same.

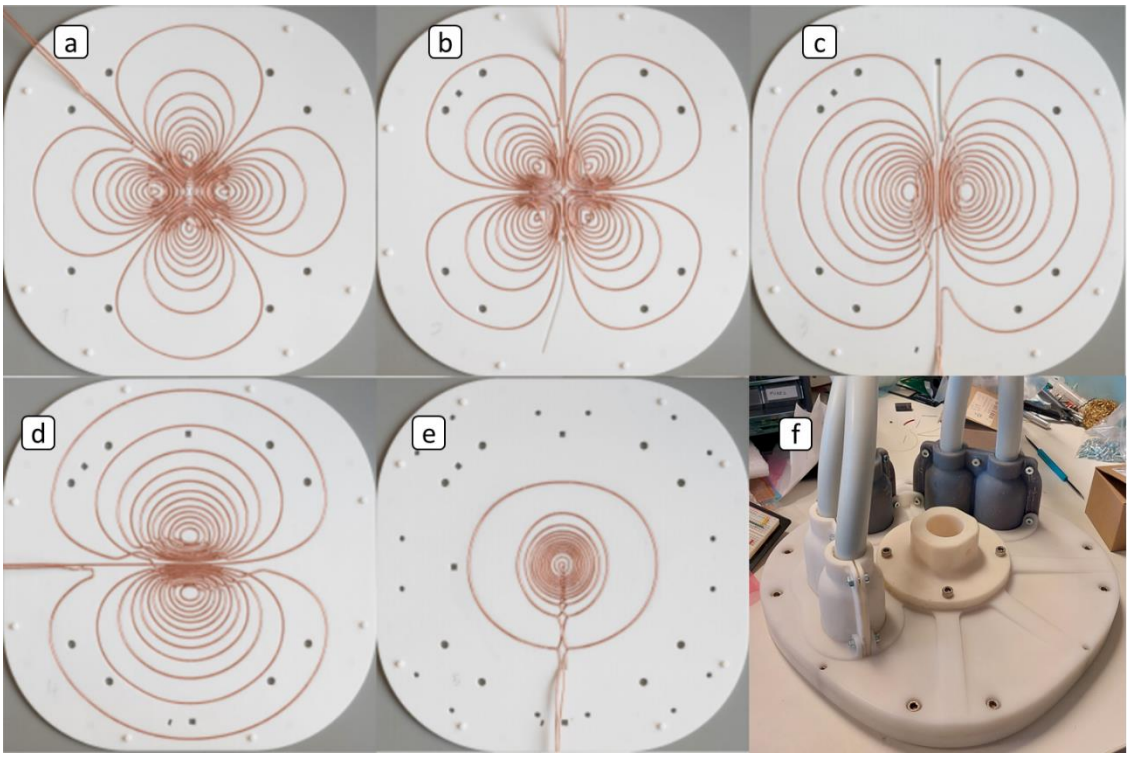

Elaborated by the author, adapted from (NIEMINEN et al., 2022)

Figure 12: Two views from the experimental setup with the mTMS transducer held by the cobot on top of the TMS calibrator

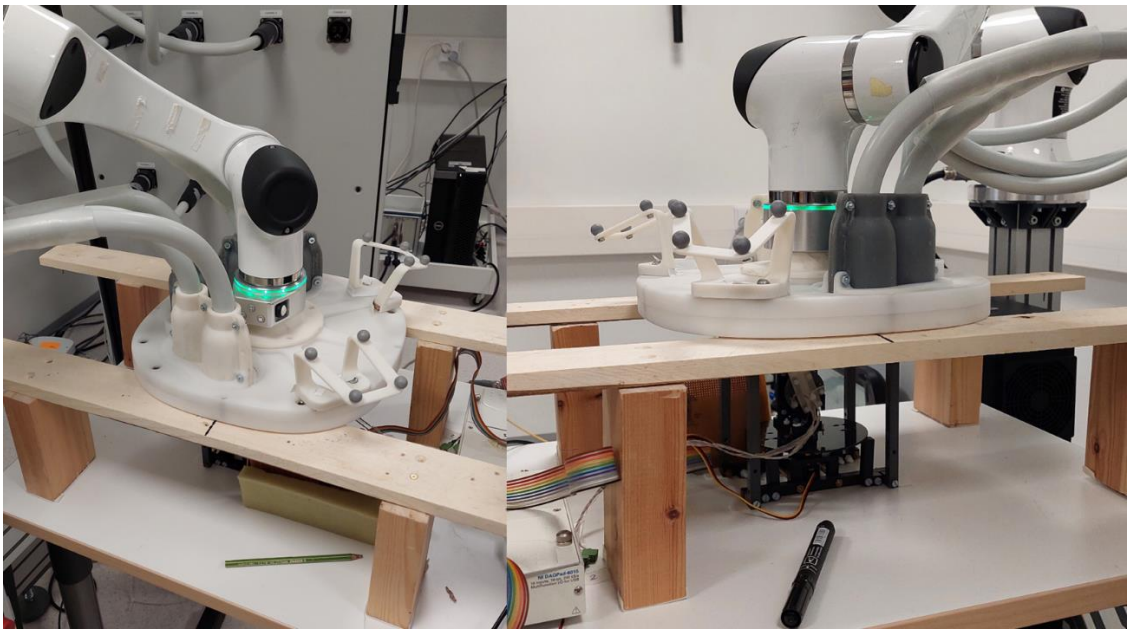

Elaborated by the author

Then, based on a scalp target defined in InVesalius, we analyzed the robotized mTMS system capability of electronically change the stimulation spot. The *random* Python library was used to create pseudo–random mTMS transducer coordinates (scalp targets). We used the maximum mTMS range (15 mm radius around the center of the TMS calibrator) to generate 10 scalp targets on the TMS calibrator top plate, i.e., the height was the same for all random targets (on the top of the TMS calibrator); the rotation angle range was defined from -30 to 30°. Figure 13 illustrates the random scalp targets. Thus, the robotized mTMS system estimates the offset to translate the maximum E-field from the center of mTMS transducer to the center of the TMS calibrator, for all random scalp targets. The E-field was mapped along 100 points, for each target, covering a 15 mm radius from the center of the TMS coil. The experiment was repeated three times, resulting in 30 random scalp targets. The accuracy of the combined robotic placement with the mTMS electronic change of the stimulation spot was assessed by the coordinates of the 70% of the E-field maximum intensity centroid. The stability was estimate as the SD and the 95^{th} percentile of the *x* and *y* centroid coordinates and for the maximum E-field intensity.

Figure 13: Dialog box to generate random scalp targets. The red arrow represents the center of the TMS calibrator. The blue arrows are the random targets to perform the electronic compensation to the center of the TMS calibrator. All the blue arrows are inside the mTMS range (15 mm radius).

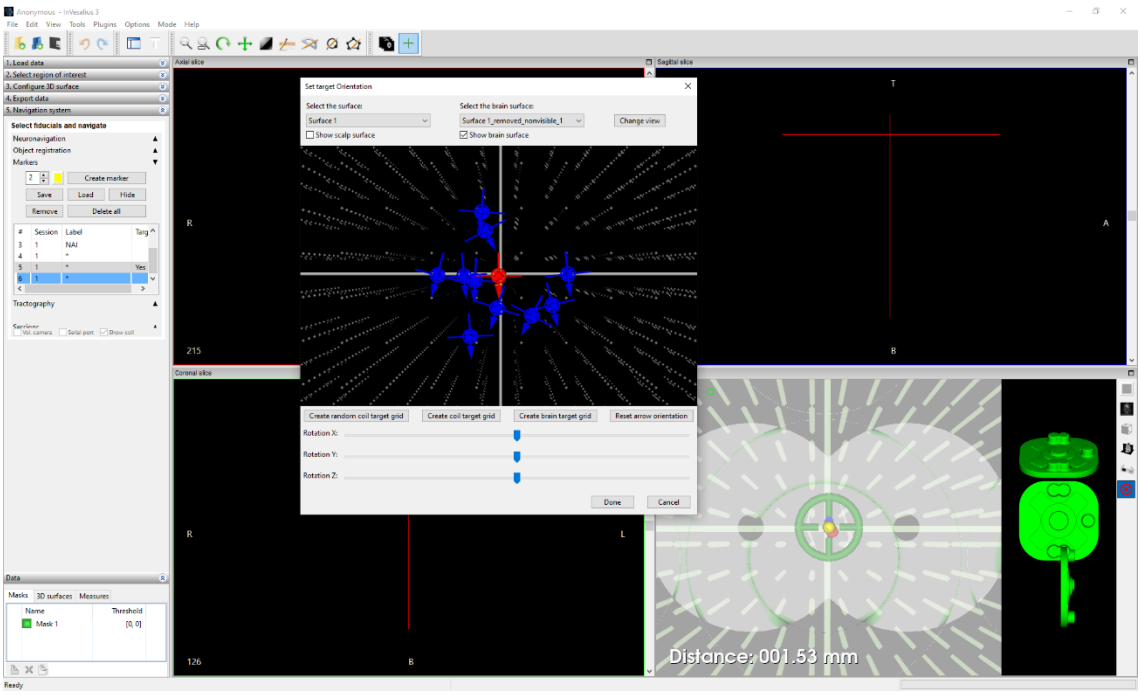

Elaborated by the author

2.2.8. ROBOTIZED MTMS MOTOR MAPPING

We performed a motor mapping experiment to demonstrate the combination of robotized transducer placement with the mTMS electronic targeting. Figure 14 depicts the experimental setup. Three healthy volunteers (32–35 year–old men with no reported neurological disorders) participated in this study. Subjects were instructed to sit comfortably in a chair. For neuronavigation, we used a T1-weighted MRI (volumetric gradient echo sequence; voxel size 1×1×1 mm^3; 240×240×240 acquisition matrix) acquired in a Skyra 3T scanner (Siemens Healthcare, Germany). The neuronavigation coregistration was performed using the three conventional fiducial landmarks: nasion, right, and left ear tragus (SOUZA et al., 2018a). Eight Flex13 cameras (OptiTrack, NaturalPoint, Inc., USA) were used as the tracking device. The cobot registration was performed with at least 500 coil paired-poses. Surface EMG electrodes (circular 24-mm diameter; Spes Medica, Italy) were placed over the *abductor pollicis brevis* (APB) muscle, following the International Federation of Clinical Neurophysiology

montage recommendation, i.e., with one electrode over the muscle belly and the other over the closest tendon, Figure 15. The EMG signal was acquired using NeurOne (Bittium Biosignals Ltd., Finland) with 24–bit resolution and 5 kHz of sampling frequency. The resting motor threshold was found as the minimal intensity needed to evoke MEPs larger than 50μV peak-to-peak amplitude in the APB in at least five out of ten pulses (CONFORTO *et al.*, 2004; KAMMER *et al.*, 2001).

Figure 14: Experimental setup for robotized mTMS motor mapping. The EMG recording software was running in a different computer than InVesalius and robot control.

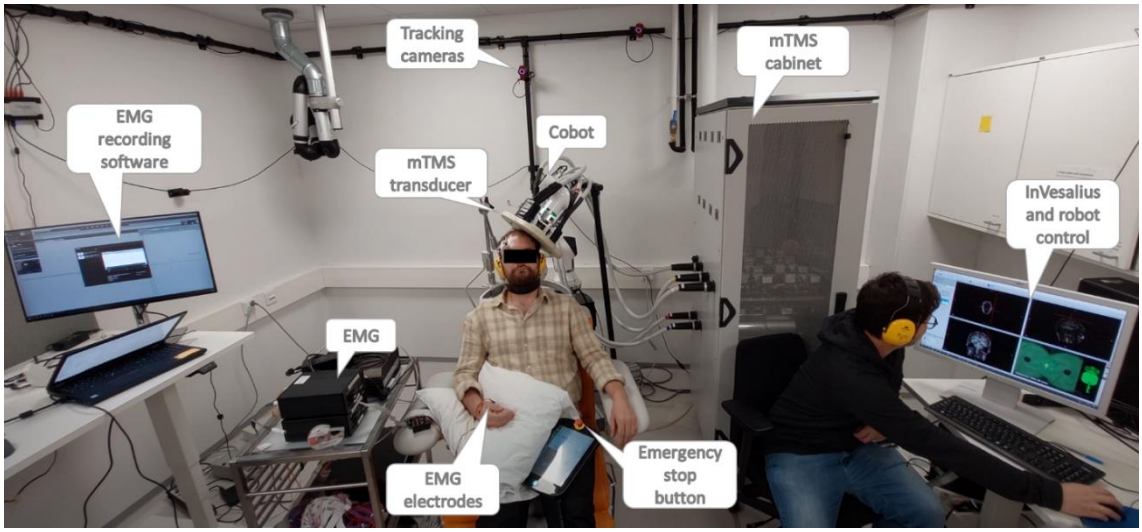

Elaborated by the author

Figure 15: Belly-tendon EMG montage, following the IFCN recommendation. The ground electrode (black) was placed on a bony prominence.

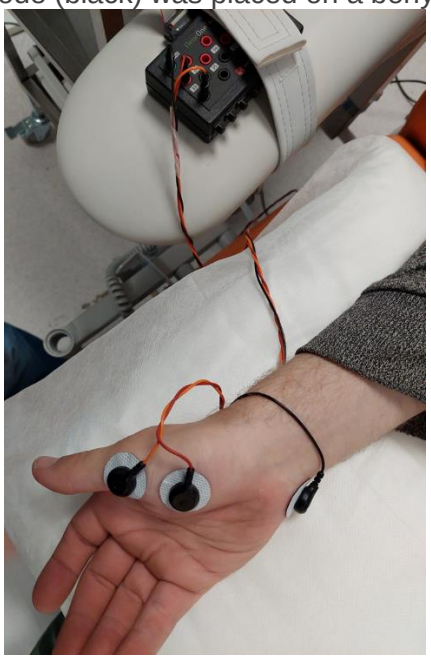

Elaborated by the author

The APB hotspot search was performed with the robot control. We pre-defined 7 robot targets along the hand knob, the stimuli orientation was perpendicular to the hand knob direction. The hotspot was defined as the scalp coil location resulting in the highest MEP amplitudes for a fixed intensity. Based on the hotspot we created two scalp targets, one on the right side and another on the left side along the primary motor cortex. Then, we created a 3 by 3 square grid of brain targets for each scalp target, Figure 16. The brain targets are projected at a 15-mm depth (KOPONEN; NIEMINEN; ILMONIEMI, 2015), along the coil normal axis, from the scalp target (Figure 17). The scalp targets are the mTMS transducer locations; the brain targets are the estimated locations of the peak induced E-field based on the scalp target. Thus, the robot control autonomously positioned the mTMS transducer on the scalp target and applied 5 mTMS pulses, with a randomized time interval between 2 to 4 seconds, for each brain target. The stimulation intensity was kept at 110% of the rest motor threshold. The stimuli were only performed if the mTMS transducer was on the target, i.e., placed within the InVesalius positioning threshold. We set the threshold to 1 mm and 1°. The motor mapping was generated with the average

MEP peak–to–peak amplitude between the 5 pulses. The color scale was normalized over the 27 MEP amplitudes for each volunteer. We implemented a gaussian interpolation method, with 4 mm radius and 3 mm sharpness, to project the color scale on the InVesalius brain mesh.

Figure 16: The yellow arrows are the scalp target, i.e., the physical location for the robotized mTMS positioning. The small blue arrows are the brain targets. There are nine brain targets for each scalp target; mTMS electronically changes the stimulation spot.

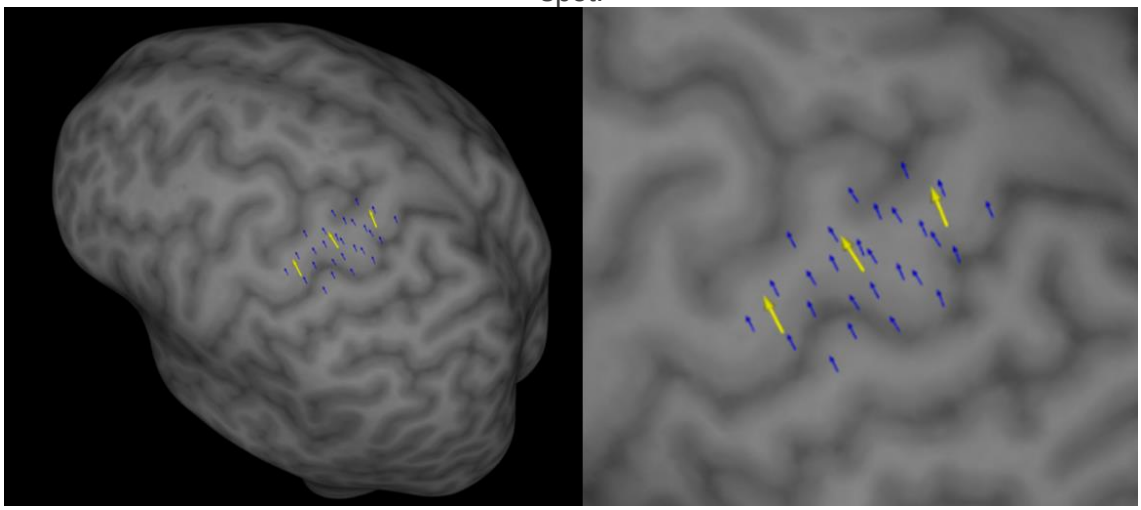

Elaborated by the author

Figure 17: Brain targets are projected 15 mm from the scalp target into the brain. The projection is based on the coil orientation.

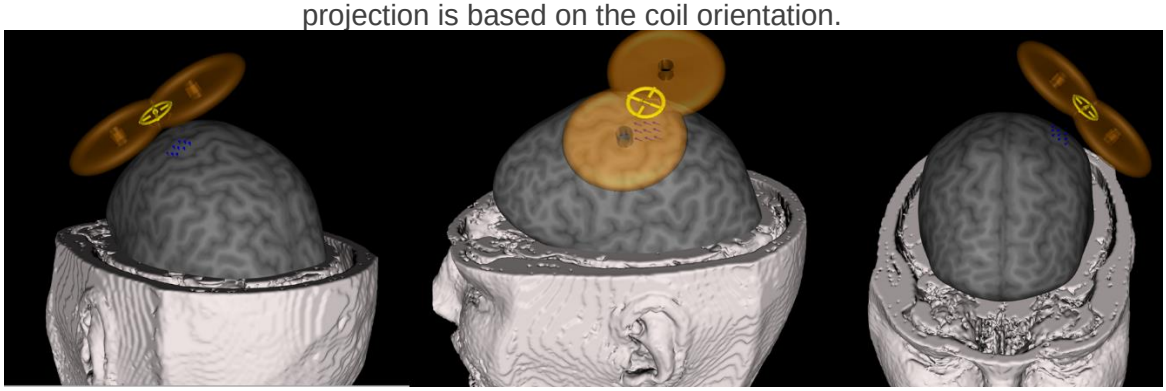

Elaborated by the author

2.3. RESULTS

2.3.1. CHARACTERIZATION

The robot control stability is depicted in Table 1. The difference to target were under 0.20 mm for the translation and between -0.20° and 0.20° for the rotation angles. The stability was ± 0.03 for the Euclidian distance between the translation axis, and an average of ± 0.03° for the rotation angles. No significant difference between was found between the rotation angles ($F_{2,7785} = 0.332$; p = 0.718), Figure 18.

Figure 18: Boxplot of the robot control stability. The translation represents the Euclidian distance between the collected coordinates and the target. On the right side, the difference between each rotation angle to the target.

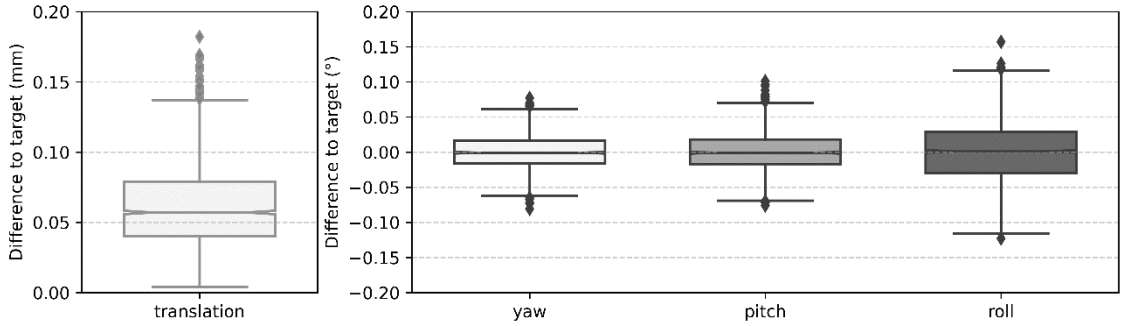

Elaborated by the author

Table 1: Standard deviation and 95th percentile of the difference between the collected coordinates to target.

Stability	Translation (mm)	Yaw (°)	Pitch (°)	Roll (°)
SD	± 0.03	± 0.02	± 0.03	± 0.04
95th percentile	0.06	0.04	0.05	0.08

The accuracy in repositioning the TMS coil on the target was evaluated in two mockups experiments: the TMS coil positioned by the cobot and manually. the robotized positioning was about 1.80 mm and 0.95° more accurate than the manual positioning for the translation axis and rotation angles, respectively ($F_{1,95} = 646.6$; $p < 0.001$; $F_{1,289} = 87.57$; $p < 0.001$). The robotized repositioning accuracy were below 0.30 mm for the translation and in a range of -0.15° to 0.15°

for the rotation angles. No difference was found between the rotation angles ($F_{2,141} = 0.451$, p = 0.638). The manually repositioning accuracy were under 3 mm and between -3° to 3°. The rotation angles have different results in the repositioning accuracy ($F_{2,144} = 16.52$, $p < 0.001$). The roll was 1.10° bigger than the pitch ($p < 0.001$) and the roll is 1.11° smaller than the yaw ($p < 0.001$) (Figure 19). Table 2 depicts the mean, SD, and 95th percentile of the repositioning accuracy.

Figure 19: Boxplots of the accuracy in repositioning the TMS coil on the target with robot control (on the top) and manually (on the bottom); * $p < 0.001$

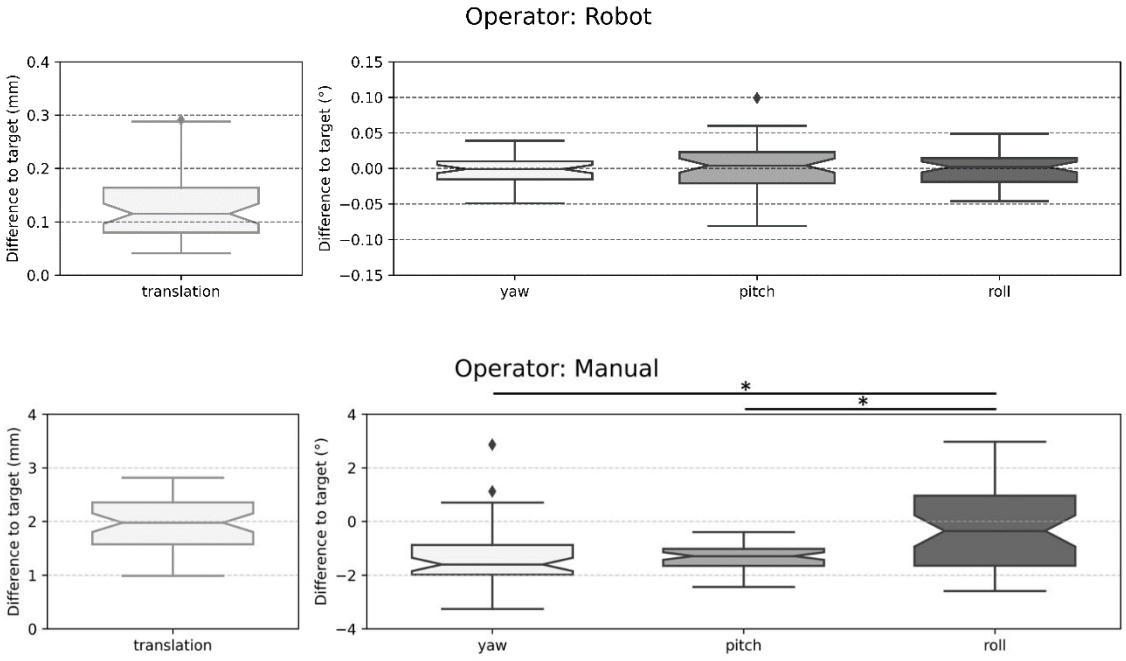

Elaborated by the author

Table 2: Comparison between robotized and manual repositioning on a TMS target

Operator	Accuracy	Translation (mm)	Yaw (°)	Pitch (°)	Roll (°)
Robot	Mean	0.13	0.00	0.01	0.00
	SD	0.06	0.02	0.04	0.02
	95th percentile	0.12	0.04	0.07	0.04
Manual	Mean	1.93	-1.33	-1.31	-0.21
	SD	0.49	1.12	0.49	1.47
	95th percentile	0.96	2.19	0.96	2.88

The E-field distribution is illustrated in Figure 20. The accuracy for the *x*-axis was ± 0.7 and ± 0.1 for the *y*-axis. The E-field variability was 0.5 mm for the *x*-axis and 0.1 mm for the *y*-axis. The mean maximum E-field intensity was 25.2 ± 0.7 V/m. Table 3 depicted the accuracy results.

Figure 20: Average E-field distribution to evaluate the accuracy in repositioning the TMS coil. The purple circles are the E-field centroids of each acquisition. The red axis is the defining the center of the distribution. The white arrows are the E-field orientation given a TMS probe calibrator position. The arrows are overlapped over each acquisition. The black dashed circle (5 mm radius) indicates the spatial extent of the E-field distribution, on the right side.

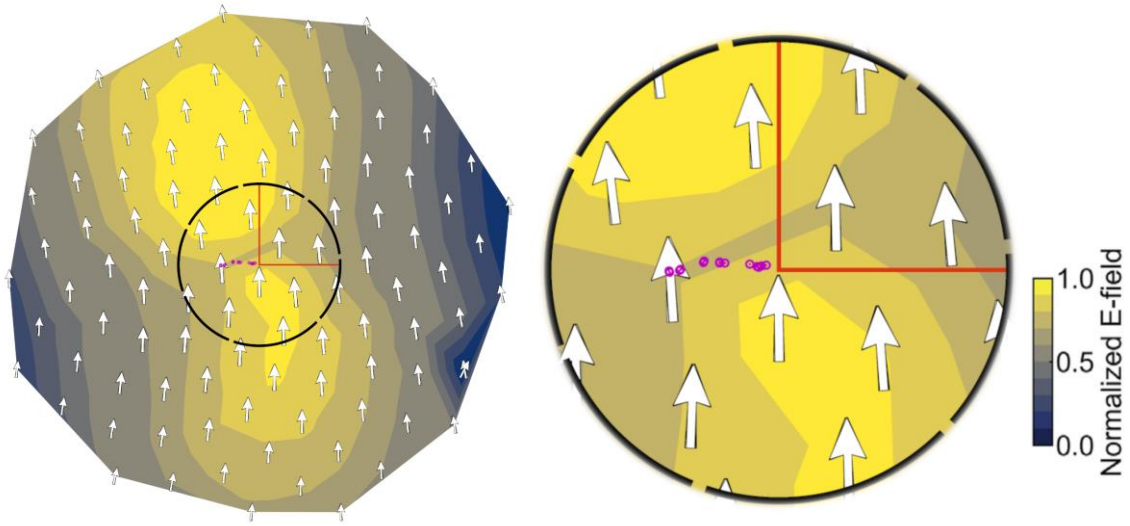

Elaborated by the author

Table 3: Mean, SD, 95th percentile, and average absolute deviation of the maximum E-field intensity and the centroid offset (*x* and *y*) from the TMS calibrator center; evaluation of the accuracy in repositioning the TMS coil.

Difference between E-field centroids	**Offset X (mm)**	**Offset Y (mm)**	**Maximum E-field (V/m)**
Mean	-0.1	-0.1	25.2
SD	± 0.7	± 0.1	± 0.7
95th percentile	1.3	0.2	1.3
Average deviation	0.5	0.1	0.5

2.3.2. ROBOTIZED MULTI–LOCUS TRANSCRANIAL MAGNETIC STIMULATION

Figure 21 illustrates the E-field distribution from the five built-in coils of the mTMS transducer. We did not notice any evident change between the E-field distribution for all coils with or without the cobot attachment. The maximum E-field with the cobot was 3.35 ± 3.22% greater than without the cobot.

Figure 21: E-field distribution from the five built-in coils of the mTMS transducer. On the left side are the coils winding and the corresponding E-field distribution, with and without the cobot, on the right side. The maximum E-field is on the top of each E-field distribution

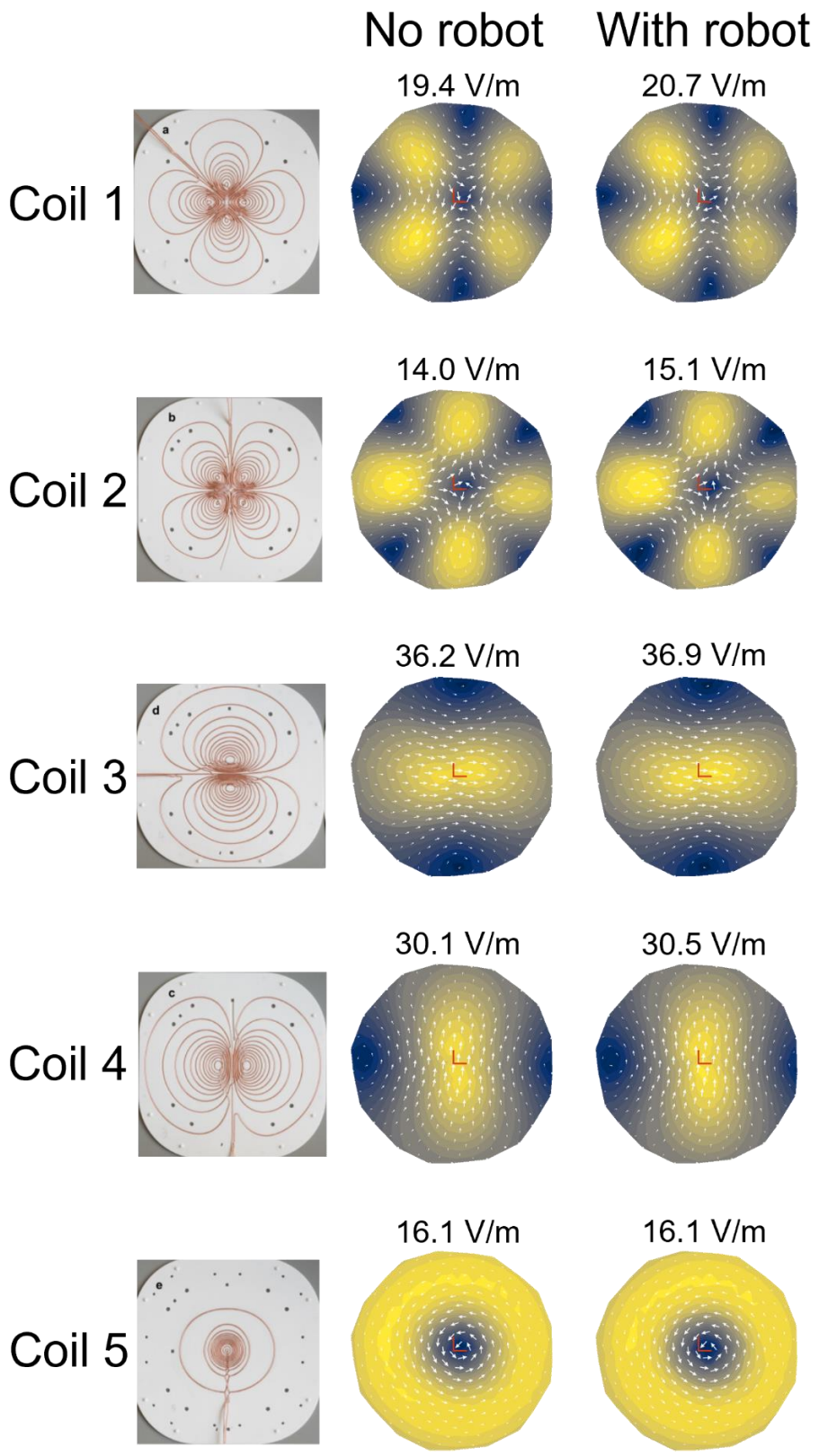

Elaborated by the author, adapted from (NIEMINEN et al., 2022)

The accuracy of the joint mTMS electronic stimulation with the robotic placement is depicted in Table 4. The average E-field distribution is illustrated in Figure 22. The accuracy for the *x* axis and *y* axis were ± 0.7 mm and ± 0.2 mm, respectively. The E-field variability was 0.6 mm for the *x*-axis and 0.2 mm for the *y*-axis. The mean E-field maximum intensity was 27.1 ± 1.0 V/m.

Figure 22: E-field distribution to evaluate the accuracy of the robotized mTMS. The purple circles are the E-field centroids of each acquisition. The red axis is the center of the distribution. The white arrows are the E-field orientation given a TMS probe calibrator position. The arrows are overlapped over each acquisition. The black dashed circle (5 mm radius) indicates the spatial extent of the E-field distribution, on the right side.

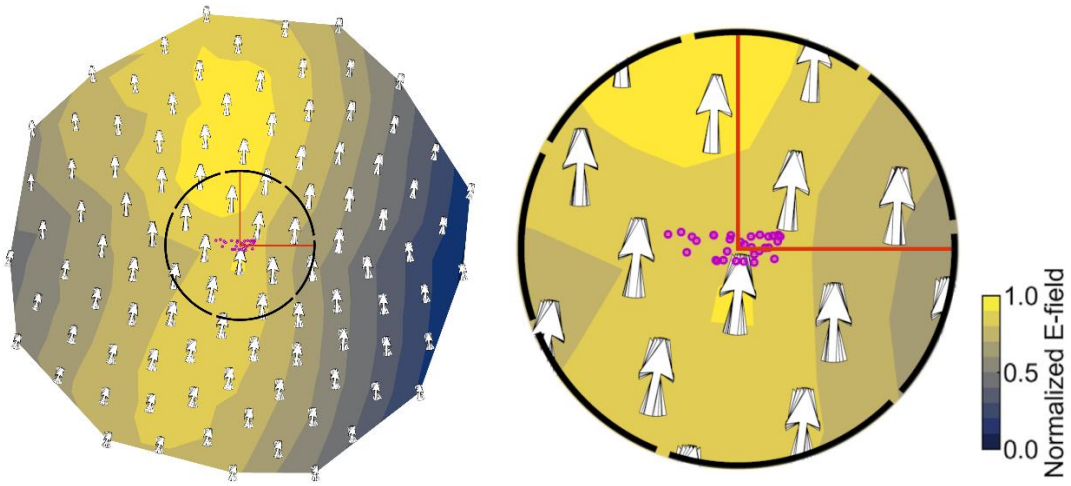

Elaborated by the author

Table 4: Mean, SD, 95th percentile, and average absolute deviation of the maximum E-field intensity and the centroid offset (x and y) from the TMS calibrator center; evaluation of the accuracy in electronically compensate the TMS coil positioning.

Difference between E-field centroids	**Offset X (mm)**	**Offset Y (mm)**	**Maximum E-field (V/m)**
Mean	0.0	0.1	27.1
SD	± 0.7	± 0.2	± 1.0
95th percentile	1.4	0.5	2.0
Average deviation	0.6	0.2	0.8

Figure 23 demonstrates the resulting motor maps obtained with the robotized mTMS for three volunteers. The color scale of the motor mapping is normalized to the maximum MEP amplitude of each individual. The motor mapping for volunteer number one covered the middle and right side of the hand

knob, resulting in a homogeneous motor mapping. The motor mapping for volunteer number two covered an anterior part of the hand knob and slightly the premotor cortex. The higher responses were on the middle part of the hand knob. The motor mapping for volunteer number three the whole hand knob and higher responses were mostly on the left side.

Figure 23: Robotized mTMS motor mapping for three volunteers. The colored dots are the brain stimulated targets on the individualized MRI for each participant. The color map is individually normalized to the maximum MEP amplitude

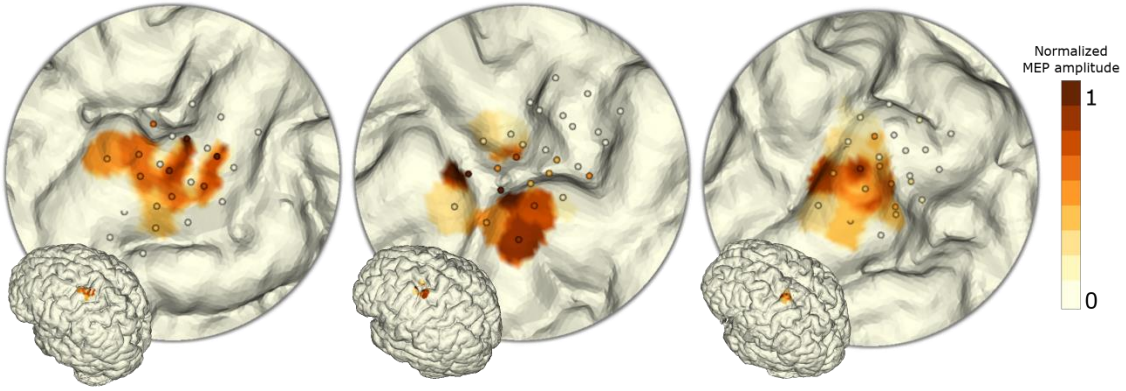

Elaborated by the author

2.4. DISCUSSION

Small variations in the TMS coil positioning cause variations in the evoked responses in the brain (HALLETT, 2000). Neuronavigation systems have been used to increase the precision and accuracy of TMS targeting. However, when the coil is manually positioned, placement inaccuracies may occur. In addition, the stimulator must be manually repositioned every time the patient moves. Also, the TMS coil positioning is challenging for conventional TMS motor mapping; requires a higher expertise form the user to perform small physical displacements and rotations of the TMS coil with precision (BASHIR *et al.*, 2013; SOUZA *et al.*, 2022; WEISS *et al.*, 2013).

To overcome these limitations, we developed a novel methodology of an autonomous robotized mTMS positioning system. We combined the cobot physical positioning with the mTMS electronic positioning enabling the automation of nTMS procedures, such as hotspot hunting and motor mapping.

We can use the robot control not only to positioning the TMS coil on target but also to follow the patient's head, performing an automated head move compensation. The robot control achieves superior accuracy comparing with manual positioning and comparable stability and accuracy to existing robotized TMS system (GRAB *et al.*, 2018; PENNIMPEDE *et al.*, 2013; RICHTER *et al.*, 2010; WAN ZAKARIA, 2012).

The characterization based on the E-field distribution revealed that our system can accurately and precisely change the E-field to stimulate the desired region. Interestingly, in

Figure 20 and Figure 22 the variation for the *y*-axis is higher than for the *x*-axis. This may be related to the shape of the focal area of the induced E-field. The figure-of-eight pattern is narrow on the *x*-axis and wide on the *y*-axis, consequently more susceptible to variations.

Although the cobot has many metallic and electronic components, the E-field distribution with and without the robot showed that there is only a minor interference in the produced E-field, validating the coupling between the cobot end-effector and the TMS coil. Intriguingly, the resulting maximum E-field intensities were slightly higher with the TMS coupled to the robot. A small TMS coil displacement can significantly change the induced E-field, and this may had affected the E-field intensity.

The major limitation of the robot control is that the tracking device and the cobot basis must be stationary over the robotized TMS session. The transformation between the cobot to the tracking device is based on the physical location of the devices. Displacements will nullify the transformation matrix, compromising the robot control accuracy.

The motor mapping experiment demonstrated the system ability to perform high dense motor mapping in a fast and autonomous approach. In the future, we will combine the real time EMG and EEG analyses, enabling the guide of TMS positioning based on the physiological responses.

2.5. CONCLUSION

Our new open-source platform for robotic control of mTMS transducer positioning is an important step to increase the accuracy and reliability of TMS procedures, facilitating the development of new tools and methods for brain investigation, such as the automation of motor mappings.

3. *MARLE*: A MARKERLESS HEAD POSE ESTIMATION FOR NAVIGATED TRANSCRANIAL MAGNETIC STIMULATION

3.1. INTRODUCTION

Neuronavigation uses a tracking device to monitor the movement of the TMS coil relative to the patient's head. Tracking devices utilizes markers or sensors fixed on the patient's head and on the TMS coil for real-time position tracking (Ruohonen and Karhu, 2010). However, marker fixation requires caution, as it must remain static during the entire treatment or experimental protocol. The accuracy of neuronavigation is compromised if the tracking markers move with respect to the brain. Small head-marker displacements can be unnoticed by the operator, leading to critical inaccuracies in monitoring the TMS coil position relative to the brain.

In conventional navigated TMS, head markers are susceptible to displacements during the coil positioning and can be challenging when combined with electroencephalography caps (Lioumis and Rosanova, 2022). A markerless tracking of the head position would increase the reliability of navigation and make the experimental procedure simpler and more accurate.

Face detection and recognition are well-established computer vision techniques. Existing algorithms can identify accurately non-face and face images and can discriminate different faces (Rowley et al., 1998). These techniques have been used for various applications such as surveillance systems and neuroscience studies based on facial expression and behavior recognition (Iancu et al., 2007; Lisetti and Schiano, 2000; Petrov et al., 2008). The combination of face detection and recognition enables real-time head pose estimation based on video recordings by facial landmark detection (Martins and Batista, 2008; Saeed et al., 2015). Automated head pose estimation open a possibility for the development of markerless neuronavigation. Studies have shown that markerless neuronavigation can aid in positron emission tomography (Goddard and Mandelkern, 2019) and neurosurgery (Jiang et al., 2015; Suenaga et al., 2015). However, the ensemble of markerless head pose estimation and TMS is a novel methodology.

To overcome the limitations imposed by physical head tracker displacements, we developed a markerless head tracker neuronavigation method

for TMS, which we call MarLe. Our method is based on a real-time head pose estimation that can be used with low-cost cameras and multiple tracking devices. In this study, we implemented our MarLe algorithm in our open source neuronavigation system InVesalius (Souza et al., 2018a), and characterized the accuracy and reliability of our markerless TMS navigation.

3.2. MATERIALS AND METHODS

The *MarLe* was implemented as a Python library distributed via cross-platform binary wheel files. Apart from conventional Python libraries, such as NumPy, the main dependencies of *MarLe* are:

1. OpenCV library (BRADSKI, 2000) for processing, calibration, and camera communication;
2. Dlib library (KING, 2009) for the face detection and head pose estimation.

MarLe combines head-pose estimation from live video streaming with tool tracking. The live video can be provided by sufficiently high-definition video cameras while the tool tracking is optimally performed by dedicated spatial tracking devices. In this study, we validated and characterized the *MarLe* algorithm with three different video cameras, a built-in live stream video camera (resolution of 2048×1536 pixels; 20 frames per second (FPS)) in the video camera unit (VCU) Polaris Vega VT (Northern Digital Inc., Canada), and two low-cost webcams c270 (Logitech, Switzerland) (resolution of 1280 × 720 pixels; 30 FPS) and c920 (Logitech, Switzerland) (1920 × 1080 pixels; 30 FPS). Tracking of the TMS coil and the fiducials collection probe were performed with the Polaris Vega VT infrared camera and markers.

3.2.1. CAMERA CALIBRATION

The camera calibration converts real-world three-dimensional (3D) position measurements to the camera's coordinate system. Overall, the calibration estimates the intrinsic and extrinsic parameters of the camera. The intrinsic

parameters are the camera geometry and lens distortion. The extrinsic parameters are the camera rotation and translation matrix relative to the tracked object. The intrinsic and extrinsic parameters are input arguments for the *MarLe*. The camera calibration algorithm followed OpenCV checkerboard pattern calibration (BRADSKI; KAEHLER, 2008). First, each camera captured 1000 checkerboard image samples from different viewpoints. Next, the camera parameters are computed based on Zhang's (2000) closed-form solution. Given the camera parameters, we found the coordinates of all checkerboard samples and we transformed them back to the two-dimensional (2D) camera coordinate. Finally, we verified the camera calibration accuracy by computing the re-projection error. The re-projection error was calculated as the absolute norm between the transformed and the found checkerboard's locations. The camera calibration algorithm was developed independently from *MarLe*.

3.2.2. MARLE WORKFLOW

The workflow of *MarLe* has five steps:

1. Establish communication between the camera and the neuronavigation system;
2. Define the transformation matrix between the TMS coil tracking device and the camera;
3. Detect the face;
4. Transform head pose estimation to the tracking device coordinate system;
5. Apply filtering to reduce jittering and measurement errors.

The OpenCV was used to establish the communication between the camera device and *MarLe* software. The user can set which camera will be used if multiple cameras are connected to the computer. The GStreamer backend, along OpenCV, was used to communicate with the VCU Vega VT. Once the camera communication is established, the *MarLe* determines the position and orientation of the head. The *MarLe* algorithm uses Dlib library combined with the pre-trained network of facial landmarks iBUG 300-W dataset (SAGONAS *et al.*, 2013) to estimate the real-time 2D location of 68 facial landmarks (KAZEMI; SULLIVAN,

2014). Then, we use OpenCV, together with the camera calibration parameters, to find the projection of the 2D facial landmark to 3D. The projection was performed using a 3D anthropometric model proposed by Martins and Batista (2008). We selected 14 facial structures for the 3D fitting: inner and outer corners of both eyebrows, inner and outer corners of both eyes, right and left bottom corners of the nostrils, both labial commissure and the middle lower lip of the mouth, and finally the chin as shown in Figure 24B.

We should note that *MarLe* provides only the markerless tracking of the head position, requiring a second device to track the TMS coil position. *MarLe* can be operated with any tracking device supported by the neuronavigation system. The *MarLe* and the secondary tracking device have different coordinates systems. A coregistration is required to operate both trackers at the same coordinate system. The coregistration consists in acquiring simultaneously the head pose in both coordinate systems. The *MarLe* collects the head pose based on the face detection and the secondary tracker collects the pose of a marker attached to the subject's head, following the conventional neuronavigation workflow. We developed a graphical user interface to perform the coregistration between the two camera systems. The coregistration requires at least 500 head positions from each camera. The head pose estimation is transformed to the secondary tracking device coordinate system using a closed-form solution through the equation:

$$\mathrm{T}_{camera}^{tracker}\,\mathrm{T}_{tracker}^{marker} = \mathrm{T}_{camera}^{head\ pose}\mathrm{T}_{head\ pose}^{marker} \qquad (15)$$

where $\mathrm{T}_{camera}^{tracker}$ and $\mathrm{T}_{head\ pose}^{marker}$ are homogeneous transformation matrices from the camera to the tracking device and from the head pose to the head tracker, respectively. The $\mathrm{T}_{tracker}^{marker}$ and $\mathrm{T}_{camera}^{head\ pose}$ matrices are head-pose-paired measurements from both *MarLe* and the secondary tracking device. Based on the least square solution using n pairs of data a function is optimized to solve both unknown matrices, $\mathrm{T}_{tracker}^{marker}$ and $\mathrm{T}_{camera}^{head\ pose}$. Figure 24A illustrates the transformation matrices. Once the coregistration is done, the head marker is removed from the subject's head.

Figure 24: (A) Transforms from camera coordinate system to coil tracker coordinate system. Assuming that the camera and the secondary tracker device are fixed, the transformation $T_{camera}^{tracker}$ and $T_{head\ pose}^{marker}$ are constants. (B) *MarLe* face detection of the first author of this paper; white dots represent the fitting of detected facial structures into the face video recordings. The yellow dot is the tracked coordinate of the head.

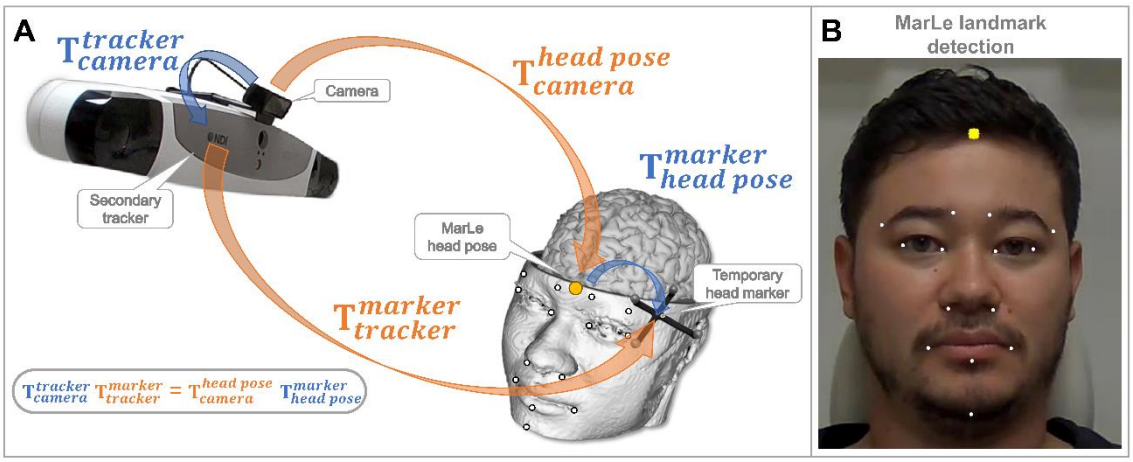

Elaborated by the author

3.2.3. FILTERING

The causes of measurement errors in optical sensors are divided into three categories: intrinsic camera parameters, irregularity, and jitter. Errors associated with the camera's intrinsic parameters are introduced into the camera manufacturing process and remain constant for a long time unless the physical structure of the camera is changed, for example due to a physical shock. The calibration section aimed to reduce the interference of the camera's intrinsic parameters through the calibration process. Irregularity errors are introduced by variations in the operating environment, for example temperature, lighting, or marker position/orientation. Jitter is a momentary deviation caused by random optical or electrical noise in the image capture and analog-to-digital conversion circuits.

The high-frequency noise oscillations, i.e., spatial jittering, in the head pose measurements decreases the head tracking accuracy (ZENG *et al.*, 2022). The final step is the real-time smoothing filter to minimize the head pose estimation jittering. We implemented a Savitzky–Golay filter (LIGORIO; SABATINI, 2013; VIVÓ-TRUYOLS; SCHOENMAKERS, 2006) based on the Python library SciPy (VIRTANEN *et al.*, 2020). The Savitzky–Golay filter uses a convolution process

to fit successive data sub-sets with a low-degree polynomial. The data sub-sets are given by fixed window size. A first-order polynomial filter was used with a window size of 5 frames.

3.2.4. CHARACTERIZATION

We characterized the stability of *MarLe* for different distances between the camera and the subject's head, the jittering, and the accuracy in repositioning the TMS coil. To measure the stability, we used a frontal human face photo printed in an A4 office paper; the printed photo has a neutral facial expression and was printed with the original head size. We collect the head pose in three distances between the camera and the face picture: 100, 125, and 150 cm. Each acquisition was recorded for three minutes every two seconds for each condition. To evaluate the filter effect on the accuracy and stability, we recorded the head pose before and after applying the Savitzky–Golay filter. These measurements were repeated three times for each of the three cameras, Logitech c270, Logitech c920, and VCU from Polaris Vega VT. The jittering was estimated as the 95% interval (1.96 times the standard deviation) of each acquired coordinate. We used the same acquisition of the stability evaluation with 100-cm distance between camera and face, with filtering, and for the three cameras.

For validating the markerless navigation, we implemented *MarLe* on the neuronavigation software platform InVesalius (AMORIM *et al.*, 2015). InVesalius is an open-source and free software for navigated TMS. InVesalius supports multiple tracking devices. We characterized and demonstrated the *MarLe* with the Polaris Vega VT as the secondary tracking device. The accuracy of *MarLe* in repositioning the TMS coil was evaluated in a mockup experiment that followed a conventional TMS procedure (JULKUNEN, 2014) except that no TMS pulses were delivered to the subject. The study was approved by the local ethics committee of the University of São Paulo (CAAE: 54674416.9.0000.5407) in accordance with the Declaration of Helsinki.

Figure 25 depicts the experimental setup. The participant (the first author: 29-year-old man with no known neurological disorders or visible facial deformations) was instructed to sit in a chair and to stay relaxed and with a neutral

facial expression. For neuronavigation, we used a T1-weighted magnetic resonance imaging acquired with a volumetric gradient echo sequence (voxel size 1×1×1 mm^3; 240×240×240 acquisition matrix) in an Achieva 3 T scanner (Philips Healthcare, Netherlands). A figure-of-eight TMS coil (Neurosoft, Russia) was placed over the scalp directly above the left hand-knob of the primary motor cortex and the scalp coordinate set as the target in InVesalius. The coil was oriented approximately perpendicular to the central sulcus. The revisiting experimental procedure included three steps: 1) coregistration between *MarLe* and the secondary tracker device, 2) neuronavigation coregistration, and 3) repositioning of the TMS coil. For the coregistration of the trackers, we collected 500 paired poses. The neuronavigation coregistration was performed using three fiducial landmarks: nasion, right and left ear tragus (SOUZA *et al.*, 2018a). The TMS coil was initially placed on a side table, which was defined as the home position. The coil was repositioned 10 times, alternating between the home and the scalp target. The InVesalius guiding interface was used to place the coil at the target and the coil coordinates were saved when the user reached the target within a 3 mm and 3° range. The experimental procedure was repeated three times for each of the three cameras. The experimental procedures followed our previous characterization protocol employed for the InVesalius Navigator (SOUZA *et al.*, 2018a).

Figure 25: Experimental setup. The MarLe head pose estimation and the TMS coil pose are collected simultaneously. The head pose is transformed to the TMS coil tracker coordinate system and sent to the neuronavigator InVesalius

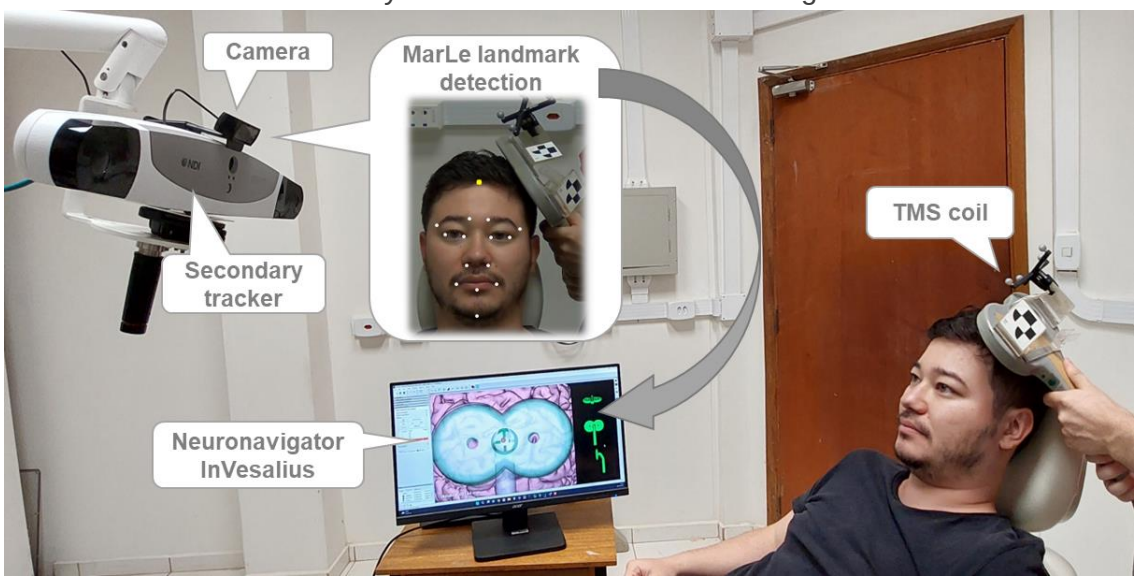

Elaborated by the author

3.2.5. STATISTICAL ANALYSIS

The stability was evaluated as the standard deviation (SD) of the difference of the translation (Euclidean distance) and three orientation vectors from the average pose coordinates during the acquisition. The effect of camera model, the camera–face distance, and the presence of filter were assessed with a two-way analysis of variance (ANOVA). The jittering of translation axis and rotation angles were evaluated with one-way ANOVA. The accuracy for revisiting a TMS coil repositioning was estimated as the average Euclidian distance and angles difference between the acquired coil pose and the predefined coil target. We used two-way ANOVA to evaluate if the camera model and the coordinates axes (translation, yaw, pitch, and roll) affects the revisiting target accuracy. Tukey HSD post-hoc multiple comparisons were performed for stability, jittering, and repeatability of coil positioning; The threshold for statistical significance was set at $p = 0.05$. The software R 4.2 (R Core Team, Austria) was used for all statistical analysis.

3.3. RESULTS

3.3.1. MARLE STABILITY AND JITTERING

The measured stability for each distance, presence of filter, and for all tested cameras are depicted in Table 5. We observed that the stability, with filtering, varied across the camera model ($F_{2,16191} = 7.88$; $p < 0.001$). The c270's average standard deviation was 0.02 mm ($p < 0.001$) smaller than the VCU Vega VT and 0.01 mm ($p = 0.02$) higher than the camera c920. The average standard deviation for the non-filtered coordinates was 68 ± 5% higher than the filtered coordinates for the camera C270, 70 ± 2% higher for the camera C920 and 37 ± 9% higher for the built-in camera Vega VT. The filtered coordinates did not reveal relevant differences between the camera–face distances ($F_{2,16191} = 0.94$; $p = 0.39$). The unfiltered coordinates did not reveal relevant differences between the cameras ($F_{2,16191} = 2.22$; $p = 0.11$) or for the camera–face distances ($F_{2,16191} = 0.10$; $p = 0.90$). No difference was found between the three trials ($p = 0.99$).

Table 5: The stability results for the distance between the camera and face, for the camera model, with and without filtering for each translation and rotation axis.

Camera	Distance	± SD X (mm)	± SD Y (mm)	± SD Z (mm)	± SD Yaw (°)	± SD Pitch (°)	± SD Roll (°)
		with / without filter	with / without filter	with / without filter	with / without filter	with / without filter	with / without filter
C270	100 cm	0.14 / 0.37	0.10 / 0.23	0.36 / 1.22	0.09 / 0.34	0.11 / 0.37	0.04 / 0.14
	125 cm	0.14 / 0.37	0.10 / 0.23	0.36 / 1.22	0.09 / 0.34	0.11 / 0.37	0.04 / 0.14
	150 cm	0.13 / 0.43	0.08 / 0.22	0.39 / 1.14	0.10 / 0.30	0.14 / 0.51	0.04 / 0.13
C920	100 cm	0.07 / 0.25	0.07 / 0.19	0.28 / 0.90	0.08 / 0.27	0.10 / 0.32	0.03 / 0.10
	125 cm	0.09 / 0.31	0.07 / 0.22	0.41 / 1.37	0.10 / 0.37	0.10 / 0.32	0.03 / 0.11
	150 cm	0.10 / 0.35	0.07 / 0.22	0.31 / 1.06	0.08 / 0.27	0.14 / 0.45	0.03 / 0.12
VCU Vega VT	100 cm	0.16 / 0.27	0.12 / 0.18	0.62 / 0.87	0.26 / 0.32	0.16 / 0.27	0.07 / 0.12
	125 cm	0.18 / 0.32	0.14 / 0.23	0.91 / 1.31	0.32 / 0.41	0.17 / 0.32	0.08 / 0.14
	150 cm	0.18 / 0.34	0.15 / 0.23	0.85 / 1.24	0.28 / 0.37	0.22 / 0.41	0.08 / 0.14

MarLe jittering was estimated with a camera–head distance of 100 cm; the results are illustrated in Figure 26. The chart points (black circles) are the distance between the measured head pose to the average head pose coordinate, recorded along 180 seconds for each translation axis (*x*, *y*, *z*) and rotation angle (yaw, pitch, roll). The red dashed lines represent the jittering, i.e., the 95% intervals

(1.96 times the standard deviation) of the static head pose estimation. The largest deviation was ± 1.78 mm obtained for the *z* axis and ± 0.62° obtained for yaw rotation, both for the Vega VT camera. The smallest deviation was found for c920, ± 0.12 mm for the *y* axis and ± 0.06° for roll rotation. The 95% intervals were within the range of ± 2 mm and ± 1° for all cameras. The camera c270 has a significant difference between the translation axis ($p < 0.001$; $F_{2,897} = 21.30$). The jittering for the *x* axis is 0.11 mm smaller than for the *y* axis ($p < 0.001$) and 0.14 mm smaller than the *z* axis ($p < 0.001$). No difference was found for the rotation angles ($p = 0.71$; $F_{2,897} = 0.34$). We did not find any difference for the translation axis and rotation angles for the cameras c920 (translation: $p = 0.84$; $F_{2,897} = 0.18$; rotation: $p = 0.39$; $F_{2,897} = 0.94$) and VCU Vega VT (translation: $p = 0.19$; $F_{2,897} = 1.67$; rotation: $p = 0.52$; $F_{2,897} = 0.61$).

Figure 26: Jittering for translation axes (x, y, y) and rotation angles (yaw, pitch, roll), evaluated for cameras c270, c920, and VCU Polaris Vega VT. Data points were sampled every 2 s for 180 s, from a frontal human face photo. The black solid line is the average, and the red dashed lines are the 95% intervals (1.96 times the standard deviation)

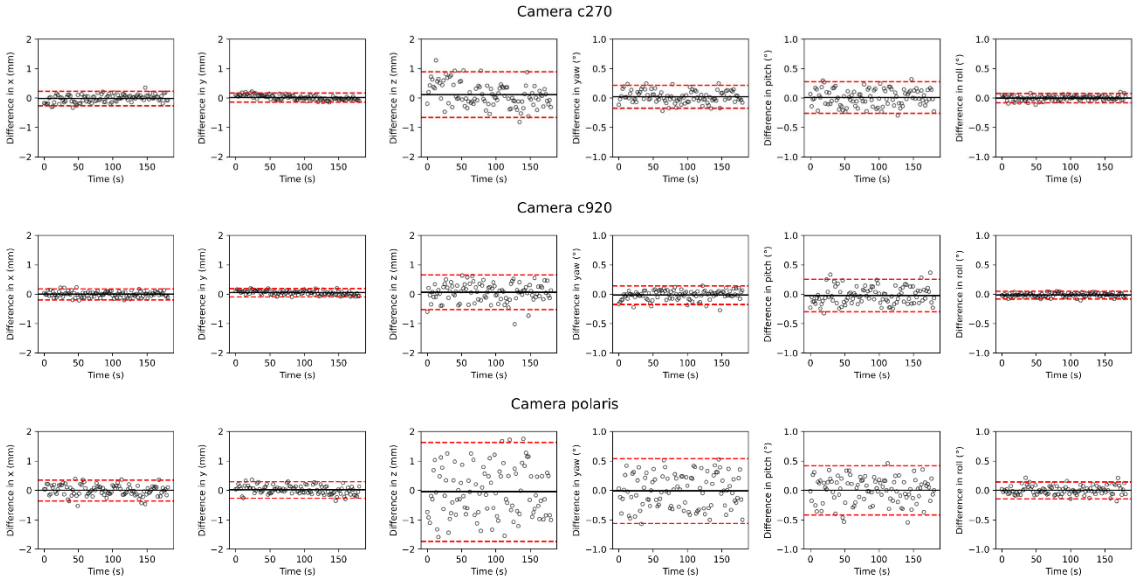

Elaborated by the author

3.3.2. ACCURACY FOR REVISITING A TMS TARGET

We evaluated the accuracy of *MarLe* for revisiting a TMS coil placement in the mockup navigated TMS experiment. The coregistration error between the

camera and the TMS coil tracker was 1.56 ± 0.96 mm for the built-in Vega VT, the low-cost camera c270 returned an error of 1.48 ± 1.10 mm and 1.38 ± 0.84 for the camera c920. The neuronavigation fiducial registration error was lower than 3 mm for all cameras and trials. The comparison of the translation vector and the rotation angles between the three cameras is ilustrated in Figure 27. The difference between the collected coordinates to the target varied depending on the rotation angle ($F_{2,288} = 12.32$; $p < 0.001$) and the camera model ($F_{2,288} = 4.63$; $p = 0.01$). However, the camera model had no significant effect on the translation vector ($F_{2,96} = 1.79$; $p = 0.17$). *MarLe* has a significantly deviation of 0.43° between pitch and roll ($p < 0.001$), 0.55° between yaw and roll ($p < 0.001$), and 0.86° in pitch between the cameras c270 and c920 ($p = 0.002$).

Figure 27: The difference to the target in translation and rotation angles for cameras c270 (white boxes), c920 (light gray boxes), and VCU Polaris Vega VT (dark gray boxes) obtained in the mockup navigated TMS experiment. * p <= 0.001.

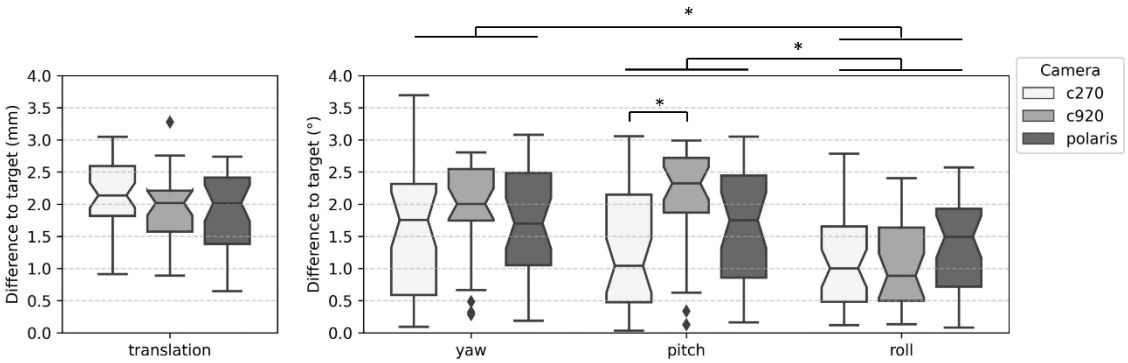

Elaborated by the author

3.4. DISCUSSION

During conventional navigated TMS, the markers or sensors fixed on the patient's head are susceptible to displacements. Uncontrollable factors, such as patients sweating or oily skin can cause the markers to move from the initial fixed position or the skin may move due to head muscle activation, leading to neuronavigation inaccuracies. Neuronavigation systems cannot distinguish head marker displacements; the mismatch detection depends on the user's expertise (SCHÖNFELDT-LECUONA *et al.*, 2005).

To overcome these limitations, we developed a markerless head tracking algorithm, named *MarLe*, for navigated TMS that can estimate the head pose based on real-time video processing. We combined, in a single device, the optimal accuracy of infrared marker tracking for the TMS coil with the *MarLe* based on the built-in video camera. Nevertheless, we can use standalone low-cost cameras to perform the head-pose estimation. In a simulated TMS experiment, neuronavigation with *MarLe* achieves acceptable accuracy and stability with the built-in Vega VT camera and with two low-cost webcams, comparable to dedicated tracking devices supported by InVesalius (SOUZA *et al.*, 2018a).

We developed an intuitive pipeline to establish the connection between *MarLe*, the camera, and InVesalius. We can use any TMS coil tracker supported by InVesalius. Currently, provides support for four commercial tracking devices. The estimation of the transformation matrix between the TMS coil tracker and the camera is done through a graphical user interface developed for InVesalius. The transformation matrix can be saved and imported for the next session.

The camera calibration errors were below 1 mm for all cameras. Camera calibration is a critical component in performing accurate tracking (BRADSKI; KAEHLER, 2008). Our *MarLe* algorithm estimates the head pose by relating the camera units (pixels) to the physical world (meters) based on the camera calibration parameters. Therefore, the camera calibration error affects the navigation accuracy. The neuronavigation error is mainly due to the coregistration variability, tracking device inaccuracy, and distortions in the anatomical images (STEINMEIER *et al.*, 2000). The recommended error limits for neuronavigation systems are 3 mm and 3° for localization positional accuracy, i.e., the inherent error of a neuronavigation system to reach a target (KUEHN *et al.*, 2008; ORRINGER; GOLBY; JOLESZ, 2012; RUOHONEN; KARHU, 2010). Some studies define the neuronavigation error based on the 95th percentile distribution of Euclidean distances between the target and the collected coordinate. In this approach, the acceptance neuronavigation error is up to 3–4 mm (MASCOTT, 2006; POGGI *et al.*, 2003; SOUZA *et al.*, 2018a). The stability and jittering experiments enabled the assessment of the tracking device accuracy while

revisiting a TMS coil placements assessed the overall neuronavigation error with *MarLe*.

Our measurements revealed that the distance between camera and face, a distance ranging from 100 to 150 cm, did not affect the *MarLe* stability to estimate a head pose. One likely explanation is that we are operating in the camera's optimal measurement volume. The *MarLe* operational distance range provides setup flexibility for the users, reducing the time spent with tracker arrangement for navigated TMS. *MarLe* stability, for filtered coordinates, depends on the resolution and acquisition frame of the camera. VCU Vega VT has the highest resolution (2048 × 1536 pixels), followed by c920 (1920 × 1080), and c270 has the lowest resolution (1280 × 720); the resolution affects the accuracy of head-pose determination (BRADSKI; KAEHLER, 2008). Higher resolution means that the pixel size is smaller, providing a better capability to detect small head movements. *MarLe* head-pose estimation stability seems to be the same for cameras with resolutions of 2048 × 1536 pixels and 1920 × 1080 pixels, but a lower resolution may affect the *MarLe* stability.

The stability for the non-filtered coordinates is not affected by the camera device or the camera–face distance. Then, filtering can increase stability, but this depends on frame rate. Namely, the Savitzky–Golay filter is affected by the amount of input data over time (SAVITZKY; GOLAY, 1964). A high acquisition rate results in a stronger filter effect, increasing the smoothing and stability of the head–pose estimation. However, the resolution seems to have no effect on the filtering. For example, the built-in camera Vega VT has the lowest frame rate (20 Hz), and it has the lowest increase in stability (37 ± 9%) after filtering. The cameras c270 and c920 have a 30-Hz acquisition rate; both have similar stability increases after filtering, 68 ± 5% and 70 ± 2%, respectively. The Savitzky–Golay filter has an important contribution to increasing the stability and consequently the accuracy of *MarLe*. It should be noted that the Savitzky–Golay filter parameters were optimized to have the lowest delay in terms of smoothness. The first-order polynomial is used due to the good response, in terms of smoothness, for low frequencies (less than 100 Hz) (SEO; MA; SAHA, 2018). The window size affects the time response; a big window size includes delays to filtered signals.

We found five frames to be optimal: there was no noticeable visual delay, and a good filter response was obtained.

The *MarLe* jittering for all cameras was less than 2 mm and 1° for translation and rotation, i.e., lower than the acceptance limit of 3 mm or 3°. Interestingly, fluctuations when using the *MarLe* algorithm are clearly smaller than those obtained with other head-pose estimation algorithms published up to now (DARBY *et al.*, 2016; MARTINS; BATISTA, 2008; SAEED; AL-HAMADI; GHONEIM, 2015). Martins and Batista (2008) found a jitter of 1 cm and 2°. This discrepancy may be caused by the face-detection algorithm. Martins and Batista (2008) used a statistical matching method (active appearance mode) to track facial characteristics. We are using a pre-trained network based on the 300–W face dataset to perform face detection. This dataset has 300 indoor and 300 outdoors in-the-wild images, including a variety of facial expressions, face sizes, illumination conditions, and occlusions (SAGONAS *et al.*, 2013).

The *z* translation axis has the higher deviation, illustrated in Figure 3. The *z* direction defines the distance between the source, i.e., the camera, to the tracked object, i.e., the face. The head-pose estimation algorithm is based on a face model; once the algorithm detects a face, we use a closed-form solution to find the required scaling to fit the face model to the detected face. The translation *z* is based on the scaling factor, and it is more susceptible to fluctuations than the *x* and *y* axis (BRADSKI; KAEHLER, 2008). However, no significant difference was found between the translation axis (*x*, *y*, *z*) and between the rotation angles (yaw, pitch, roll) for the c920 and built-in Vega VT. The camera c270 has a deviation only between the translation axes. This might be caused by the low camera resolution (BRADSKI; KAEHLER, 2008).

Finally, the *MarLe* accuracy for revisiting a coil placement was in a range of 3–4 mm and 3–4° for the 95th percentile, corroborating previous findings (MASCOTT, 2006; POGGI *et al.*, 2003; SOUZA *et al.*, 2018a). As was expected, *MarLe* connected to c270 showed the highest deviations between the TMS target. Again, this association might point toward low camera resolution (BRADSKI; KAEHLER, 2008).

It is important to highlight that the TMS coil tracker and the camera must be stationary over the TMS session. The transformation between the camera to the

coil tracker is based on the physical location of the devices. Displacements will nullify the transformation matrix and the coregistration must be redone. However, we could overcome this limitation with the Polaris Vega VT. Regarding face detection, we noticed that *MarLe* becomes more unstable when the volunteer smiles or talks. Therefore, the *MarLe* characterization and the simulated TMS experiment were performed with neutral facial expressions. In the future, we will combine facial expression recognition with face detection, which might enable us to perform the head pose estimation only with a neutral expression and warn the user when a different expression is detected, avoiding unstable pose estimations. One might also be able to teach the algorithm to use features in the face that do not move when facial expressions change.

3.5. CONCLUSION

We developed a markerless head-pose estimation algorithm for navigated transcranial magnetic stimulation. *MarLe* has a potential to improve the reliability and ease of TMS targeting, simplifying, and reducing the time to perform the determination of head pose.

4. FINAL REMARKS

This thesis presents methods that automate and improve the accuracy of TMS procedures. The developed robot control brings a novel approach for TMS positioning by combining the physical and electronic control of the stimulation target. The developed tools open new possibilities for TMS protocol, such as the robotized mTMS motor mapping, and provide new approaches to investigate and understand complex brain mechanisms. Finally, the markerless head tracker, *MarLe*, might improve the TMS reliability, ease of nTMS targeting, and simplifying neuronavigation procedures.

In the future, we are planning to implement new automations for TMS interventions, for example, using closed-loop hotspot and resting motor threshold hunting, and a closed-loop brain stimulation based on the real-time physiological data analyses. In addition, *MarLe* can be a useful platform to combine facial expression recognition with face detection, allowing, for instance, brain studies involving behavior analysis.

5. REFERENCES

AMORIM, P.; MORAES, T.; SILVA, J.; PEDRINI, H. InVesalius: An Interactive Rendering Framework for Health Care Support. *Em*: Lecture Notes in Computer Science. Springer International Publishing, 2015. p. 45–54.

BARKER, A. T.; JALINOUS, R.; FREESTON, I. L. Non-invasive magnetic stimulation of human motor cortex. **The Lancet**, v. 325, n. 8437, p. 1106–1107, 1985.

BASHIR, S.; PEREZ, J. M.; HORVATH, J. C.; PASCUAL-LEONE, A. Differentiation of Motor Cortical Representation of Hand Muscles by Navigated Mapping of Optimal TMS Current Directions in Healthy Subjects. **Journal of Clinical Neurophysiology**, v. 30, n. 4, p. 390–395, ago. 2013. Disponível em: <https://journals.lww.com/00004691-201308000-00012>.

BOROOJERDI, B.; FOLTYS, H.; KRINGS, T.; SPETZGER, U.; THRON, A.; TÖPPER, R. Localization of the motor hand area using transcranial magnetic stimulation and functional magnetic resonance imaging. **Clinical Neurophysiology**, v. 110, n. 4, p. 699–704, abr. 1999. Disponível em: <https://linkinghub.elsevier.com/retrieve/pii/S1388245798000273>.

BRADSKI, G. The OpenCV Library. **Dr. Dobb's Journal of Software Tools**, 2000.

BRADSKI, G.; KAEHLER, A. Learning OpenCV: Computer Vision with the OpenCV Library. **O'Reilly Media, Inc.**, set. 2008.

BRASIL-NETO, J. P.; COHEN, L. G.; PANIZZA, M.; NILSSON, J.; ROTH, B. J.; HALLETT, M. Optimal focal transcranial magnetic activation of the human motor cortex: Effects of coil orientation, shape of the induced current pulse, and stimulus intensity. **Journal of Clinical Neurophysiology**, v. 9, n. 1, p. 132–136, 1992.

CHIARELLI, A. M.; MACLIN, E. L.; LOW, K. A.; FABIANI, M.; GRATTON, G. Comparison of procedures for co-registering scalp-recording locations to anatomical magnetic resonance images. **Journal of Biomedical Optics**, v. 20, n. 1, p. 016009, 2015. Disponível em: <http://biomedicaloptics.spiedigitallibrary.org/article.aspx?doi=10.1117/1.JBO.20.1.016009>.

CINCOTTA, M.; GIOVANNELLI, F.; BORGHERESI, A.; BALESTRIERI, F.; TOSCANI, L.; ZACCARA, G.; CARDUCCI, F.; VIGGIANO, M. P.; ROSSI, S. Optically tracked neuronavigation increases the stability of hand-held focal coil positioning: Evidence from "transcranial" magnetic stimulation-induced electrical field measurements. **Brain Stimulation**, v. 3, n. 2, p. 119–123, 2010. Disponível em: <http://dx.doi.org/10.1016/j.brs.2010.01.001>.

CONFORTO, A. B.; Z'GRAGGEN, W. J.; KOHL, A. S.; RÖSLER, K. M.; KAELIN-LANG, A. Impact of coil position and electrophysiological monitoring on determination of motor thresholds to transcranial magnetic stimulation. **Clinical Neurophysiology**, v. 115, n. 4, p. 812–819, 2004.

DARBY, J.; SÁNCHEZ, M. B.; BUTLER, P. B.; LORAM, I. D. An evaluation of 3D head pose estimation using the Microsoft Kinect v2. **Gait and Posture**, v. 48, p. 83–88, 2016.

ETTINGER, G. J.; LEVENTON, M. E.; GRIMSON, W. E.; KIKINIS, R.; GUGINO, L.; COTE, W.; SPRUNG, L.; AGLIO, L.; SHENTON, M. E.; POTTS, G.; HERNANDEZ, V. L.; ALEXANDER, E. Experimentation with a transcranial magnetic stimulation system for functional brain mapping. **Medical image analysis**, v. 2, n. 2, p. 133–142, 1998.

EVANS, A. C.; COLLINS, D. L.; MILLS, S. R.; BROWN, E. D.; KELLY, R. L.; PETERS, T. M. 3D statistical neuroanatomical models from 305 MRI volumes. **1993 IEEE Conference Record Nuclear Science Symposium and Medical Imaging Conference**, p. 1813–1817, 1993. Disponível em: <http://ieeexplore.ieee.org/lpdocs/epic03/wrapper.htm?arnumber=373602>.

FEDOROV, A.; BEICHEL, R.; KALPATHY-CRAMER, J.; FINET, J.; FILLION-ROBIN, J.-C.; PUJOL, S.; BAUER, C.; JENNINGS, D.; FENNESSY, F.; SONKA, M.; BUATTI, J.; AYLWARD, S.; MILLER, J. v; PIEPER, S.; KIKINIS, R. 3D Slicer as an image computing platform for the Quantitative Imaging Network. **Magnetic resonance imaging**, v. 30, n. 9, p. 1323–41, nov. 2012.

GARCIA, M. A. C.; SOUZA, V. H.; LINDOLFO-ALMAS, J.; MATSUDA, R. H.; NOGUEIRA-CAMPOS, A. A. Motor potential evoked by transcranial magnetic stimulation depends on the placement protocol of recording electrodes: a pilot study. **Biomedical Physics & Engineering Express**, v. 6, n. 4, p. 047003, 12 jun. 2020. Disponível em: <https://iopscience.iop.org/article/10.1088/2057-1976/ab950a>.

GARCIA, M. A. C.; SOUZA, V. H.; VARGAS, C. D. Can the Recording of Motor Potentials Evoked by Transcranial Magnetic Stimulation Be Optimized? **Frontiers in Human Neuroscience**, v. 11, n. August, p. 1–4, 2017. Disponível em: <http://journal.frontiersin.org/article/10.3389/fnhum.2017.00413/full>.

GERING, D. T.; NABAVI, A.; KIKINIS, R.; HATA, N.; O'DONNELL, L. J.; GRIMSON, W. E. L.; JOLESZ, F. A.; BLACK, P. M.; WELLS, W. M. An integrated visualization system for surgical planning and guidance using image fusion and an open MR. **Journal of Magnetic Resonance Imaging**, v. 13, n. 6, p. 967–975, jun. 2001. Disponível em: <https://onlinelibrary.wiley.com/doi/10.1002/jmri.1139>.

GIUFFRE, A.; KAHL, C. K.; ZEWDIE, E.; WRIGHTSON, J. G.; BOURGEOIS, A.; CONDLIFFE, E. G.; KIRTON, A. Reliability of robotic transcranial magnetic stimulation motor mapping. **Journal of Neurophysiology**, v. 125, n. 1, p. 74–85, 1 jan. 2021. Disponível em: <https://journals.physiology.org/doi/10.1152/jn.00527.2020>.

GOETZ, S. M.; KOZYRKOV, I. C.; LUBER, B.; LISANBY, S. H.; MURPHY, D. L. K.; GRILL, W. M.; PETERCHEV, A. v. Accuracy of robotic coil positioning during transcranial magnetic stimulation. **Journal of Neural Engineering**, v. 16, n. 5, p. 054003, 17 set. 2019. Disponível em: <https://iopscience.iop.org/article/10.1088/1741-2552/ab2953>.

GRAB, J. G.; ZEWDIE, E.; CARLSON, H. L.; KUO, H.-C.; CIECHANSKI, P.; HODGE, J.; GIUFFRE, A.; KIRTON, A. Robotic TMS mapping of motor cortex in the developing brain. **Journal of Neuroscience Methods**, v. 309, n. August, p. 41–54, 2018. Disponível em: <https://linkinghub.elsevier.com/retrieve/pii/S0165027018302437>.

GRUNERT, P.; DARABI, K.; ESPINOSA, J.; FILIPPI, R. **Computer-aided navigation in neurosurgeryNeurosurgical Review**2003.

HAASE, J. Neuronavigation. **Child's Nervous System**, v. 15, n. 11–12, p. 755–757, 1999. Disponível em: <<Go to ISI>://WOS:000083862700018>.

HAIDEGGER, T. Autonomy for Surgical Robots: Concepts and Paradigms. **IEEE Transactions on Medical Robotics and Bionics**, v. 1, n. 2, p. 65–76, 2019.

HALLETT, M. Transcranial magnetic stimulation and the human brain. **Nature**, v. 406, n. 6792, p. 147–150, 2000.

JULKUNEN, P. Methods for estimating cortical motor representation size and location in navigated transcranial magnetic stimulation. **Journal of Neuroscience Methods**, v. 232, p. 125–133, 2014.

KALLIONIEMI, E.; KÖNÖNEN, M.; JULKUNEN, P. Repeatability of functional anisotropy in navigated transcranial magnetic stimulation – coil-orientation versus response. **NeuroReport**, v. 26, n. 9, p. 515–521, 2015. Disponível em: <http://content.wkhealth.com/linkback/openurl?sid=WKPTLP:landingpage&an=00001756-201506020-00005>.

KAMMER, T.; BECK, S.; THIELSCHER, A.; LAUBIS-HERRMANN, U.; TOPKA, H. Motor Thresholds in Humans: A Transcranial Magnetic Stimulation Study Comparing Different Pulse Waveforms, Current Directions and Stimulator Types. **Clinical Neurophysiology**, v. 112, p. 250–258, 2001.

KAZEMI, V.; SULLIVAN, J. One millisecond face alignment with an ensemble of regression trees. Em: 2014 IEEE Conference on Computer Vision and Pattern Recognition, 2014, [...]. IEEE, 2014. p. 1867–1874.

KING, D. E. Dlib-ml: A machine learning toolkit. **Journal of Machine Learning Research**, v. 10, p. 1755–1758, 2009.

KOPONEN, L. M.; NIEMINEN, J. O.; ILMONIEMI, R. J. Minimum-energy coils for transcranial magnetic stimulation: Application to focal stimulation. **Brain Stimulation**, v. 8, n. 1, p. 124–134, 2015. Disponível em: <http://dx.doi.org/10.1016/j.brs.2014.10.002>.

KOPONEN, L. M.; NIEMINEN, J. O.; ILMONIEMI, R. J. Multi-locus transcranial magnetic stimulation—theory and implementation. **Brain Stimulation**, v. 11, n. 4, p. 849–855, 2018. Disponível em: <https://doi.org/10.1016/j.brs.2018.03.014>.

KUEHN, B.; MULARSKI, S.; SCHOENHERR, S.; HAMMERSEN, S.; STENDEL, R.; KOMBOS, T.; SUESS, S.; SUESS, O. Sensor-based neuronavigation: Evaluation of a large continuous patient population. **Clinical Neurology and Neurosurgery**, v. 110, n. 10, p. 1012–1019, 2008.

LEFAUCHEUR, J.-P. Why image-guided navigation becomes essential in the practice of transcranial magnetic stimulation. **Neurophysiologie clinique = Clinical neurophysiology**, v. 40, p. 1–5, 2010.

LIGORIO, G.; SABATINI, A. M. Extended Kalman filter-based methods for pose estimation using visual, inertial and magnetic sensors: Comparative analysis and performance evaluation. **Sensors (Switzerland)**, v. 13, n. 2, p. 1919–1941, 2013.

LITTLE, G.; BOE, S.; BARDOUILLE, T. Head movement compensation in real-time magnetoencephalographic recordings. **MethodsX**, v. 1, p. e275–e282, 2014. Disponível em: <http://dx.doi.org/10.1016/j.mex.2014.10.008>.

MARTINS, P.; BATISTA, J. Single view head pose estimation. Em: 2008 15th IEEE International Conference on Image Processing, 2008, [...]. IEEE, 2008. p. 1652–1655.

MASCOTT, C. R. In vivo accuracy of image guidance performed using optical tracking and optimized registration. **Journal of Neurosurgery**, v. 105, n. 4, p. 561–567, 2006. Disponível em: <http://thejns.org/doi/10.3171/jns.2006.105.4.561>.

MATSUDA, R. H.; TARDELLI, G. P.; GUIMARÃES, C. O.; SOUZA, V. H.; BAFFA FILHO, O. Estimulação magnética transcraniana: uma breve revisão dos princípios e aplicações. **Revista Brasileira de Física Médica**, v. 13, n. 1, p. 49, 1 set. 2019. Disponível em: <http://www.rbfm.org.br/rbfm/article/view/497>.

MATTHÄUS, L.; TRILLENBERG, P.; BODENSTEINER, C.; GIESE, A.; SCHWEIKARD, A. Robotized TMS for motion compensated navigated brain stimulation. **International Journal of Computer Assisted Radiology and Surgery**, v. 1, n. SUPPL. 7, p. 139–141, 2006.

MURTHY, S. V. K.; MACLELLAN, M.; BEYEA, S.; BARDOUILLE, T. Faster and improved 3-D head digitization in MEG using Kinect. **Frontiers in Neuroscience**, v. 8, n. OCT, p. 1–7, 2014.

NIEMINEN, J. O.; KOPONEN, L. M.; ILMONIEMI, R. J. Experimental characterization of the electric field distribution induced by TMS devices. **Brain Stimulation**, v. 8, n. 3, p. 582–589, 2015. Disponível em: <http://dx.doi.org/10.1016/j.brs.2015.01.004>.

NIEMINEN, J. O.; KOPONEN, L. M.; MÄKELÄ, N.; SOUZA, V. H.; STENROOS, M.; ILMONIEMI, R. J. Short-interval intracortical inhibition in human primary motor cortex: A multi-locus transcranial magnetic stimulation study. **NeuroImage**, v. 203, n. September, 2019.

NIEMINEN, J. O.; SINISALO, H.; SOUZA, V. H.; MALMI, M.; YURYEV, M.; TERVO, A. E.; STENROOS, M.; MILARDOVICH, D.; KORHONEN, J. T.; KOPONEN, L. M.; ILMONIEMI, R. J. Multi-locus transcranial magnetic stimulation system for electronically targeted brain stimulation. **Brain Stimulation**, v. 15, n. 1, p. 116–124, jan. 2022. Disponível em: <https://linkinghub.elsevier.com/retrieve/pii/S1935861X21008299>.

NOCCARO, A.; MIOLI, A.; PINARDI, M.; PINO, G. di; FORMICA, D. Development and validation of a novel calibration methodology and control approach for robot-aided Transcranial Magnetic Stimulation (TMS). v. 9294, n. c, p. 1–12, 2021.

ORRINGER, D. A.; GOLBY, A.; JOLESZ, F. Neuronavigation in the surgical management of brain tumors: current and future trends. **Expert Review of Medical Devices**, v. 9, n. 5, p. 491–500, 9 set. 2012. Disponível em: <http://www.tandfonline.com/doi/full/10.1586/erd.12.42>.

PELL, G. S.; ROTH, Y.; ZANGEN, A. Modulation of cortical excitability induced by repetitive transcranial magnetic stimulation: Influence of timing and geometrical parameters and underlying mechanisms. **Progress in Neurobiology**, v. 93, n. 1, p. 59–98, 2011. Disponível em: <http://dx.doi.org/10.1016/j.pneurobio.2010.10.003>.

PENNIMPEDE, G.; SPEDALIERE, L.; FORMICA, D.; DI PINO, G.; ZOLLO, L.; PELLEGRINO, G.; DI LAZZARO, V.; GUGLIELMELLI, E. Hot spot hound: A novel robot-assisted platform for enhancing TMS performance. **Proceedings of the Annual International Conference of the IEEE Engineering in Medicine and Biology Society, EMBS**, p. 6301–6304, 2013.

PERES, A. S. C.; SOUZA, V. H. O.; RODRIGUES, E. M.; SALMON, C. E. G.; DE ARAUJO, D. B.; BAFFA, O. Real-time spatial localization system of brain regions for TMS application by co-registration with fMRI. **IFMBE Proceedings**, v. 28, p. 92–96, 2010.

PESHKIN, M.; COLGATE, J. E. Cobots. **Industrial Robot: An International Journal**, v. 26, n. 5, p. 335–341, 1 jul. 1999. Disponível em: <https://www.emerald.com/insight/content/doi/10.1108/01439919910283722/full/html>.

POGGI, S.; PALLOTTA, S.; RUSSO, S.; GALLINA, P.; TORRESIN, A.; BUCCIOLINI, M. Neuronavigation accuracy dependence on CT and MR imaging parameters: A phantom-based study. **Physics in Medicine and Biology**, v. 48, n. 14, p. 2199–2216, 2003.

RICHTER, L.; MATTHÄUS, L.; SCHLAEFER, A.; SCHWEIKARD, A. Fast robotic compensation of spontaneous head motion during Transcranial Magnetic Stimulation (TMS). **UKACC International Conference on CONTROL 2010**, p. 872–877, 2010. Disponível em: <http://digital-library.theiet.org/content/conferences/10.1049/ic.2010.0396>.

ROMERO, J. R.; RAMIREZ, D. M.; AGLIO, L. S.; GUGINO, L. D. Brain mapping using transcranial magnetic stimulation. **Neurosurgery Clinics of North America**, v. 22, n. 2, p. 141–152, 2011. Disponível em: <http://dx.doi.org/10.1016/j.nec.2010.11.002>.

ROSLER, J.; NIRAULA, B.; STRACK, V.; ZDUNCZYK, A.; SCHILT, S.; SAVOLAINEN, P.; LIOUMIS, P.; MAKELA, J.; VAJKOCZY, P.; FREY, D.; PICHT, T. Language mapping in healthy volunteers and brain tumor patients with a novel navigated TMS system: Evidence of tumor-induced plasticity. **Clinical Neurophysiology**, v. 125, n. 3, p. 526–536, 2014.

ROSSINI, P. M.; BURKE, D.; CHEN, R.; COHEN, L. G.; DASKALAKIS, Z.; DI IORIO, R.; DI LAZZARO, V.; FERRERI, F.; FITZGERALD, P. B.; GEORGE, M. S.; HALLETT, M.; LEFAUCHEUR, J. P.; LANGGUTH, B.; MATSUMOTO, H.; MINIUSSI, C.; NITSCHE, M. A.; PASCUAL-LEONE, A.; PAULUS, W.; ROSSI, S.; ROTHWELL, J. C.; SIEBNER, H. R.; UGAWA, Y.; WALSH, V.; ZIEMANN, U. Non-invasive electrical and magnetic stimulation of the brain, spinal cord, roots and peripheral nerves: Basic principles and procedures for routine clinical and research application: An updated report from an I.F.C.N. Committee. **Clinical Neurophysiology**, v. 126, n. 6, p. 1071–1107, 2015. Disponível em: <http://dx.doi.org/10.1016/j.clinph.2015.02.001>.

ROSSINI, P. M.; ROSSI, S. Clinical applications of motor evoked potentials. **Electroencephalography and clinical neurophysiology**, v. 106, n. 3, p. 180–94, mar. 1998. Disponível em: <http://www.ncbi.nlm.nih.gov/pubmed/9743275>.

ROTH, B. J.; BASSER, P. J. Electromagnetic Induction. v. 37, n. 6, 1990.

RUOHONEN, J.; KARHU, J. Navigated transcranial magnetic stimulation. **Neurophysiologie clinique = Clinical neurophysiology**, v. 40, n. 1, p. 7–17, 2010. Disponível em: <http://dx.doi.org/10.1016/j.neucli.2010.01.006>.

SAEED, A.; AL-HAMADI, A.; GHONEIM, A. Head Pose Estimation on Top of Haar-Like Face Detection: A Study Using the Kinect Sensor. **Sensors**, v. 15, n. 9, p. 20945–20966, 26 ago. 2015. Disponível em: <http://www.mdpi.com/1424-8220/15/9/20945>.

SAGONAS, C.; TZIMIROPOULOS, G.; ZAFEIRIOU, S.; PANTIC, M. 300 faces in-the-wild challenge: The first facial landmark Localization Challenge. **Proceedings of the IEEE International Conference on Computer Vision**, p. 397–403, 2013.

SÄISÄNEN, L.; PIRINEN, E.; TEITTI, S.; KÖNÖNEN, M.; JULKUNEN, P.; MÄÄTTÄ, S.; KARHU, J. Factors influencing cortical silent period: Optimized stimulus

location, intensity and muscle contraction. **Journal of Neuroscience Methods**, v. 169, n. 1, p. 231–238, 2008.

SAVITZKY, A.; GOLAY, M. J. E. Smoothing and Differentiation of Data by Simplified Least Squares Procedures. **Analytical Chemistry**, v. 36, n. 8, p. 1627–1639, 1964.

SCHÖNFELDT-LECUONA, C.; THIELSCHER, A.; FREUDENMANN, R. W.; KRON, M.; SPITZER, M.; HERWIG, U. Accuracy of stereotaxic positioning of transcranial magnetic stimulation. **Brain Topography**, v. 17, n. 4, p. 253–259, 2005.

SEO, J.; MA, H.; SAHA, T. K. On savitzky-golay filtering for online condition monitoring of transformer on-load tap changer. **IEEE Transactions on Power Delivery**, v. 33, n. 4, p. 1689–1698, 2018.

SOUZA, V. H.; MATSUDA, R. H.; PERES, A. S. C.; AMORIM, P. H. J.; MORAES, T. F.; SILVA, J. V. L.; BAFFA, O. Development and characterization of the InVesalius Navigator software for navigated transcranial magnetic stimulation. **Journal of Neuroscience Methods**, v. 309, n. June, p. 109–120, 2018a. Disponível em: <https://linkinghub.elsevier.com/retrieve/pii/S0165027018302577>.

SOUZA, V. H.; NIEMINEN, J. O.; TUGIN, S.; KOPONEN, L. M.; BAFFA, O.; ILMONIEMI, R. J. TMS with fast and accurate electronic control: Measuring the orientation sensitivity of corticomotor pathways. **Brain Stimulation**, v. 15, n. 2, p. 306–315, 1 mar. 2022. Disponível em: <https://linkinghub.elsevier.com/retrieve/pii/S1935861X22000109>.

SOUZA, V. H.; VIEIRA, T. M.; PERES, A. S. C.; GARCIA, M. A. C.; VARGAS, C. D.; BAFFA, O. Effect of TMS coil orientation on the spatial distribution of motor evoked potentials in an intrinsic hand muscle. **Biomedical Engineering / Biomedizinische Technik**, v. 63, n. 6, p. 635–645, 27 nov. 2018b. Disponível em: <http://www.degruyter.com/view/j/bmte.ahead-of-print/bmt-2016-0240/bmt-2016-0240.xml>.

STEINMEIER, R.; RACHINGER, J.; KAUS, M.; GANSLANDT, O.; HUK, W.; FAHLBUSCH, R. Factors influencing the application accuracy of neuronavigation systems. **Stereotactic and Functional Neurosurgery**, v. 75, n. 4, p. 188–202, 2000.

TARDELLI, G. P.; SOUZA, V. H.; MATSUDA, R. H.; GARCIA, M. A. C.; NOVIKOV, P. A.; NAZAROVA, M. A.; BAFFA, O. Forearm and Hand Muscles Exhibit High Coactivation and Overlapping of Cortical Motor Representations. **Brain Topography**, v. 35, n. 3, p. 322–336, 1 maio 2022.

TSUZUKI, D.; DAN, I. Spatial registration for functional near-infrared spectroscopy: From channel position on the scalp to cortical location in individual and group analyses. **NeuroImage**, v. 85, p. 92–103, 2014. Disponível em: <http://dx.doi.org/10.1016/j.neuroimage.2013.07.025>.

VIRTANEN, P.; GOMMERS, R.; OLIPHANT, T. E.; HABERLAND, M.; REDDY, T.; COURNAPEAU, D.; BUROVSKI, E.; PETERSON, P.; WECKESSER, W.; BRIGHT, J.; VAN DER WALT, S. J.; BRETT, M.; WILSON, J.; MILLMAN, K. J.; MAYOROV, N.; NELSON, A. R. J.; JONES, E.; KERN, R.; LARSON, E.; CAREY, C. J.; POLAT, İ.; FENG, Y.; MOORE, E. W.; VANDERPLAS, J.; LAXALDE, D.; PERKTOLD, J.; CIMRMAN, R.; HENRIKSEN, I.; QUINTERO, E. A.; HARRIS, C. R.; ARCHIBALD, A. M.; RIBEIRO, A. H.; PEDREGOSA, F.; VAN MULBREGT, P.; VIJAYKUMAR, A.; BARDELLI, A. Pietro; ROTHBERG, A.; HILBOLL, A.; KLOECKNER, A.; SCOPATZ, A.; LEE, A.; ROKEM, A.;

WOODS, C. N.; FULTON, C.; MASSON, C.; HÄGGSTRÖM, C.; FITZGERALD, C.; NICHOLSON, D. A.; HAGEN, D. R.; PASECHNIK, D. V.; OLIVETTI, E.; MARTIN, E.; WIESER, E.; SILVA, F.; LENDERS, F.; WILHELM, F.; YOUNG, G.; PRICE, G. A.; INGOLD, G.-L.; ALLEN, G. E.; LEE, G. R.; AUDREN, H.; PROBST, I.; DIETRICH, J. P.; SILTERRA, J.; WEBBER, J. T.; SLAVIČ, J.; NOTHMAN, J.; BUCHNER, J.; KULICK, J.; SCHÖNBERGER, J. L.; DE MIRANDA CARDOSO, J. V.; REIMER, J.; HARRINGTON, J.; RODRÍGUEZ, J. L. C.; NUNEZ-IGLESIAS, J.; KUCZYNSKI, J.; TRITZ, K.; THOMA, M.; NEWVILLE, M.; KÜMMERER, M.; BOLINGBROKE, M.; TARTRE, M.; PAK, M.; SMITH, N. J.; NOWACZYK, N.; SHEBANOV, N.; PAVLYK, O.; BRODTKORB, P. A.; LEE, P.; MCGIBBON, R. T.; FELDBAUER, R.; LEWIS, S.; TYGIER, S.; SIEVERT, S.; VIGNA, S.; PETERSON, S.; MORE, S.; PUDLIK, T.; OSHIMA, T.; PINGEL, T. J.; ROBITAILLE, T. P.; SPURA, T.; JONES, T. R.; CERA, T.; LESLIE, T.; ZITO, T.; KRAUSS, T.; UPADHYAY, U.; HALCHENKO, Y. O.; VÁZQUEZ-BAEZA, Y. SciPy 1.0: fundamental algorithms for scientific computing in Python. **Nature Methods**, v. 17, n. 3, p. 261–272, 2 mar. 2020.

VIVÓ-TRUYOLS, G.; SCHOENMAKERS, P. J. Automatic selection of optimal Savitzky-Golay smoothing. **Analytical Chemistry**, v. 78, n. 13, p. 4598–4608, 2006.

WAN ZAKARIA, W. N. Force-Controlled Transcranial Magnetic Stimulation (Tms) Robotic System. n. July, p. 273, 2012. Disponível em: <https://theses.ncl.ac.uk/dspace/handle/10443/1517>.

WAN ZAKARIA, W. N.; TOMARI, R.; NGADENGON, R. Active Head Motion Compensation of TMS Robotic System Using Neuro-Fuzzy Estimation. **MATEC Web of Conferences**, v. 56, p. 1–5, 2016.

WASSERMANN, E. M.; MCSHANE, L. M.; HALLETT, M.; COHEN, L. G. Noninvasive mapping of muscle representations in human motor cortex. **Electroencephalography and Clinical Neurophysiology/ Evoked Potentials**, v. 85, n. 1, p. 1–8, 1992.

WASSERMANN, E. M.; ZIMMERMANN, T. Transcranial magnetic brain stimulation: Therapeutic promises and scientific gaps. **Pharmacology and Therapeutics**, v. 133, n. 1, p. 98–107, 2012.

WEISS, C.; NETTEKOVEN, C.; REHME, A. K.; NEUSCHMELTING, V.; EISENBEIS, A.; GOLDBRUNNER, R.; GREFKES, C. Mapping the hand, foot and face representations in the primary motor cortex - retest reliability of neuronavigated TMS versus functional MRI. **NeuroImage**, v. 66, p. 531–42, fev. 2013.

ZENG, A.; YANG, L.; JU, X.; LI, J.; WANG, J.; XU, Q. SmoothNet: A plug-and-play network for refining human poses in videos. **European Conference on Computer Vision**, 27 dez. 2022. Disponível em: <http://arxiv.org/abs/2112.13715>.

ZHANG, Z. A flexible new technique for camera calibration. **IEEE Transactions on Pattern Analysis and Machine Intelligence**, v. 22, n. 11, p. 1330–1334, 2000. Disponível em: <http://ieeexplore.ieee.org/document/888718/>.

ZIEMANN, U. Transcranial magnetic stimulation: Its Current Role in the Evaluation of Patients Post-Stroke. **Neurology Report**, v. 24, n. 3, 2000.

APPENDIX A – FOREARM AND HAND MUSCLES EXHIBIT HIGH COACTIVATION AND OVERLAPPING OF CORTICAL MOTOR REPRESENTATIONS

This article is published at the journal Brain Topography (DOI: 10.1007/s10548-022-00893-1). The reuse of this article in my thesis is in compliance with Springer Copyright policy.

Title: Forearm and hand muscles exhibit high coactivation and overlapping of cortical motor representations

Authors: Gabriela P. Tardelli[a*], Victor Hugo Souza[a,b,c], Renan H. Matsuda[a,b], Marco A. C. Garcia[a,c,d] , Pavel A. Novikov[e], Maria A. Nazarova[e,f] , Oswaldo Baffa[a*]

[a] Department of Physics, School of Philosophy, Science and Literature of Ribeirão Preto, University of São Paulo, Ribeirão Preto, Brazil

[b] Department of Neuroscience and Biomedical Engineering, Aalto University School of Science, Espoo, Finland

[c] Graduate Program in Rehabilitation Sciences and Functional Physical Performance, School of Physiotherapy, Federal University of Juiz de Fora, Juiz de Fora, Brazil

[d] Neuro Biomechanics Group, School of Physiotherapy, Federal University of Juiz de Fora, Juiz de Fora, Brazil

[e] Centre for Cognition and Decision Making, Institute for Cognitive Neuroscience, National Research University Higher School of Economics, Moscow, Russia

[f] Federal State Budgetary Institution «Federal center of brain research and neurotechnologies» of the Federal Medical Biological Agency, Moscow, Russian Federation

Abstract

Most of the motor mapping procedures using navigated transcranial magnetic stimulation (nTMS) follow the conventional somatotopic organization of the primary motor cortex (M1) by assessing the representation of a particular target muscle, disregarding the possible coactivation of synergistic muscles. In turn, multiple reports describe a functional organization of the M1 with an overlapping among motor representations acting together to execute

movements. In this context, the overlap degree among cortical representations of synergistic hand and forearm muscles remains an open question. This study aimed to evaluate the muscle coactivation and representation overlapping common to the grasping movement and its dependence on the stimulation parameters. The nTMS motor maps were obtained from one carpal muscle and two intrinsic hand muscles during rest. We quantified the overlapping motor maps in size (area and volume overlap degree) and topography (similarity and centroid's Euclidean distance) parameters. We demonstrated that these muscle representations are highly overlapped and similar in shape. The overlap degrees involving the forearm muscle were significantly higher than only among the intrinsic hand muscles. Moreover, the stimulation intensity had a stronger effect on the size compared to the topography parameters. Our study contributes to a more detailed cortical motor representation towards a synergistic, functional arrangement of M1. Understanding the muscle group coactivation may provide more accurate motor maps when delineating the eloquent brain tissue during pre-surgical planning.

Keywords

Motor mapping, Transcranial magnetic stimulation, TMS, Motor evoked potential, Neuronavigation, Synergy

Introduction

A fundamental debate on primary motor cortex (M1) organization is whether different body parts rely on a discrete somatotopic or functionally-specific representation on the cortical surface (SCHIEBER, 2001). In the M1, the somatotopic organization associates a cortical site to the control of a specific muscle (PENFIELD; RASMUSSEN, 1950), whereas the functional organization suggests the cortical representation of limb movements (GENTNER *et al.*, 2010; STROTHER *et al.*, 2012). Several studies have demonstrated that the high complexity of central movement generation can be derived from an extensive overlap and redundancy between adjacent cortical area representations (DEVANNE *et al.*, 2006; GENTNER; CLASSEN, 2006; MELGARI *et al.*, 2008; SCHIEBER, 2001). The overlapping areas can be related to specific movements involving more than one adjacent single joint and, therefore, a complex synergy among different muscles (LEO *et al.*, 2016; STROTHER *et al.*, 2012), which

corroborates a hypothesis of the functional organization of M1. In this context, the overlap degree (OD) in the cortical representation of synergistic hand and forearm muscles remains an open question.

In navigated transcranial magnetic stimulation (nTMS), a coil placed on the scalp over M1 produces magnetic pulses that induce electric fields in the cortical tissue. The neuronal excitation results in action potentials that propagate through the corticospinal tract generating motor evoked potentials (MEP). The MEP amplitude combined with the TMS coil coordinates of the individual's brain enables one to delimit the extension and location of the motor cortical representations of the body parts (ROMERO *et al.*, 2011). The nTMS mapping is widely used for delineating eloquent motor function in a preoperative setting (KRIEG *et al.*, 2017; LEFAUCHEUR; PICHT, 2016). An approach that accounts for the functional overlap in cortical motor representations can lead to more selective cortical maps with the potential to improve patient prognostics (FREY *et al.*, 2014; PICHT *et al.*, 2016).

A few studies claim that the overlap in cortical representation may partially represent a cortical manifestation for synergies (CHEUNG *et al.*, 2012; HUFFMASTER *et al.*, 2018; LATASH; SCHOLZ; SCHÖNER, 2007; LEO *et al.*, 2016; OVERDUIN *et al.*, 2012; PEARCE *et al.*, 2000; RAFFIN; SIEBNER, 2019; TYC; BOYADJIAN, 2005). In this model, multiple muscle groups form different synergy patterns producing complex movements (FRICKE *et al.*, 2020). To the best of our knowledge, most conventional motor mapping procedures assess the cortical representation of a particular target muscle (KRIEG *et al.*, 2017), disregarding the possible synergistic activation of the adjacent muscles. This coactivation of muscle groups may provide further information about how and to what degree synergistic muscles are represented at the cortical level (LEO *et al.*, 2016).

The aim of our study was to quantify the OD between the cortical motor representation of two intrinsic hand muscles and one carpal forearm muscle in rest conditions. Using nTMS mapping, we delineated the motor representation of the selected muscles considering their synergistic activation. We hypothesized that these representations would be highly overlapped due to the muscles' extensive coactivation in several hand movements, e.g., grasping. Also, the OD

would differ between adjacent and target muscles from different body parts and would increase with the TMS intensity. Our results provide novel evidence on the functional cortical motor organization of the human brain.

Material and Methods

Participants

The experiment was performed with 12 right-handed (Edinburgh handedness inventory (Oldfield 1971), mean score: +75; range: +55 to +95) young male volunteers (mean age: 31.3 ± 2.5 years; range: 27–35 years). Participants were asymptomatic to neurological and psychiatric disorders, without recurrent headaches, and free of medication during the data collection phase. The experimental procedure followed the Declaration of Helsinki and was approved by the local ethical committee (CAAE: 54674416.9.0000.5407). Before the testing procedures, all participants signed a consent form.

Experimental procedure

Subjects underwent a magnetic resonance imaging (MRI) scan (Achieva 3T; Philips Healthcare, Netherlands) with a T1-weighted gradient-echo sequence (acquisition matrix 240x240x240, voxel size 1x1x1 mm^3, 6.7 ms repetition time, and 3.1 ms echo time). The gray matter surface of the brain was segmented using SPM 12 software (FRISTON *et al.*, 2006) for guiding the nTMS coil placement. Surface EMG electrodes (circular 10-mm diameter; model 2223 BRQ, 3M Brazil Ltd., Sumaré, Brazil) were placed in a pseudo-monopolar montage, with one electrode over the innervation zone and the other over the closest bone eminence (GARCIA *et al.*, 2020; GARCIA; SOUZA; VARGAS, 2017). The selected muscles were one right carpal forearm muscle (*flexor carpi radialis;* FCR), and two right intrinsic hand muscles, a thenar (*flexor pollicis brevis*; FPB) and a hypothenar muscle (*abductor digiti minimi;* ADM). EMG data were continuously recorded from the three muscles and digitized with the EMG 410C amplifier (gain: 2000 x, sampling frequency: 3.5 kHz per channel, band-pass 4^{th}-order Butterworth filter: 20-500 Hz, A/D converter: 12 bits; EMG System do Brasil, São José dos Campos, Brazil).

The participants sat in a reclining chair and were instructed to stay fully relaxed with their right hand in a neutral posture during the nTMS session. TMS biphasic pulses were delivered with a figure-of-eight coil (10 cm diameter

windings) connected to a Neuro-MS stimulator (Neurosoft, Ivanovo, Russia). The coil placement was guided by the neuronavigation software InVesalius Navigator (SOUZA *et al.*, 2018b) connected to the MicronTracker Sx60 (ClaroNav, Toronto, Canada) spatial tracker. Figure 1A depicts the experimental setup. The following procedure was applied separately for each muscle (FCR, FPB, and ADM). First, the hotspot was defined as the coil location showing the highest MEP amplitudes with the coil tangential to the scalp and approximately perpendicular to the central sulcus (BASHIR *et al.*, 2013b; SOUZA *et al.*, 2017). Second, the resting motor threshold (rMT) was defined as the minimum stimulator intensity at which the MEP amplitudes were greater than 100 μV in 5 out of 10 pulses (NIELSEN, 1996; NOGUEIRA-CAMPOS *et al.*, 2014). A higher threshold amplitude than the usual 50 μV (CONFORTO *et al.*, 2004b) was selected to provide stable MEP measurements desired when using a relatively small number of trials per stimulation site during motor mapping (PELLEGRINI; ZOGHI; JABERZADEH, 2018).

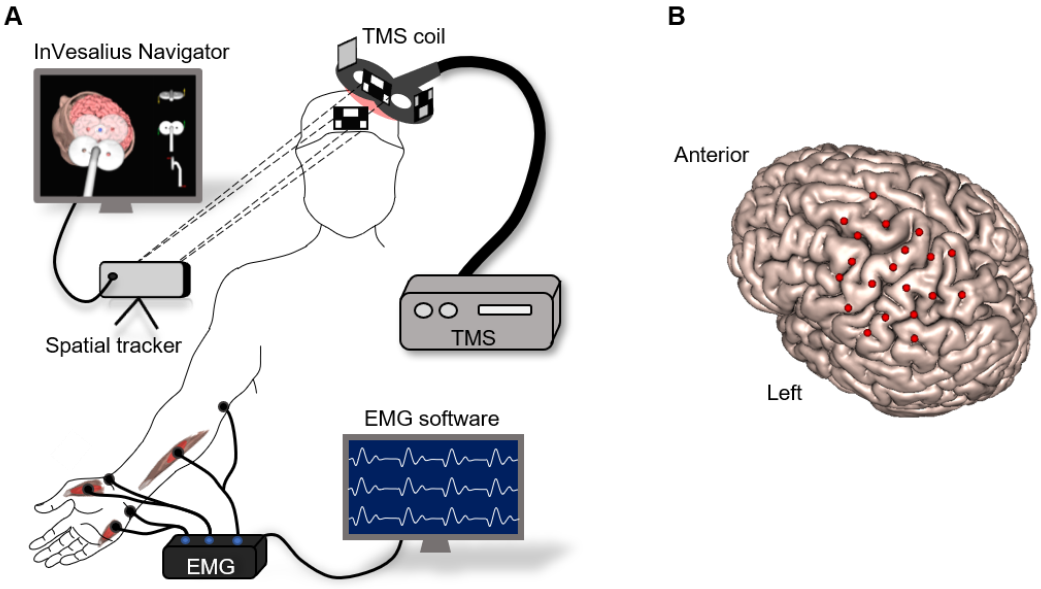

Fig. 1 A) Schematic representation of the experimental setup. The MEPs were recorded simultaneously from the hand and forearm muscles while TMS was applied over the left hemisphere guided by the InVesalius Navigator software. B) Grid of coil center locations relative to the cortical surface. This motor map was recorded at a stimulation intensity of 120% of rMT of the FCR muscle

on a representative subject. The grid was centered on the muscle's hotspot, and each coil location is the average across three trials.

Motor mapping was performed following the pseudo-random walk method with three consecutive TMS pulses in each of the 20 sites around the target muscle's hotspot (CAVALERI; SCHABRUN; CHIPCHASE, 2018; JONKER *et al.*, 2018; VAN DE RUIT; PERENBOOM; GREY, 2015). Each motor map composed an unevenly spaced grid centered on the hotspot for each individual, as illustrated for a representative subject in Fig 1B. The distance between adjacent stimulation sites was approximately 14.5 ± 3.6 mm, and interpulse intervals were pseudo-randomized between 5 and 10 s. EMG signal was recorded from the three muscles simultaneously, and the coordinates of the coil center were recorded with the neuronavigation software. A trigger signal synchronized the EMG and the neuronavigation software. The target muscle was defined as the one whose stimulation intensity was set relative to its rMT, and the stimuli were delivered over a region centered at the hotspot. The remaining muscles were defined as adjacent. The experiment was repeated for each target muscle (ADM, FCR, and FPB) and with stimulation intensities of 110% and 120% of the rMT, scaled according to the maximum stimulator output (MSO).

Motor map processing

The EMG signals were processed using the Signal Hunter software written in Matlab R2017a (MathWorks Inc., Natick, USA). The peak-to-peak amplitude was computed for MEPs extracted from the EMG signal in a time window 10–60 ms after the TMS pulse. The EMG signal was visually inspected, and trials with muscle pre-activation, artifacts, or noise over ± 20 μV up to 300 ms before the TMS pulse in amplitude were rejected. After the preprocessing, all subjects had three trials in each of the 20 cortical targets per motor map, except for one subject in which three out of the 60 stimulations were rejected due to muscle pre-activation and noisy EMG signals. The coil center coordinates obtained from InVesalius Navigator were imported into Signal Hunter and aligned to the corresponding MEP amplitude and the latency of the three muscles. One participant was removed from the data analysis due to technical problems in the TMS–EMG synchronization.

The cortical motor maps were created in the TMSmap software (NOVIKOV; NAZAROVA; NIKULIN, 2018) with the individuals' MRI, stimulation coordinates, and the correspondent MEP amplitudes. The software creates the maps with the mean coordinates and the median peak-to-peak MEP amplitudes of the merged closely spaced coordinates, resulting in a cortical motor map with 20 MEP amplitudes and coil locations per tested condition for each subject. The technical details of the map processing steps performed in the TMSmap software are described in Appendix 1. For each target muscle, we constructed two overlaps: the target with each of the adjacent muscles (two maps) and the target with both adjacent muscles together (three maps). The area, volume, and centroid were computed for all maps from each subject and stimulation intensity. The area represents the extent of the cortical motor representation, and the volume represents the area weighted by the motor response amplitude. To quantify the topographic similarity between two (or three) maps, we computed the Earth's movers distance (EMD), which estimates the work required to move one spatial distribution to another (RUBNER; TOMASI; GUIBAS, 1998). The Euclidean distance between the target muscle and the overlap map centroids of the corresponding target and its adjacent muscles was computed to evaluate differences in the spatial distribution of the muscle of interest when overlapped with another map. We defined the EMD and the Euclidean distance as topography parameters.

To evaluate the coactivation between the muscle representations, we defined the size parameters as area and volume OD. The OD was computed as the percentage of the area (or volume) that evoked two or three muscles relative to the total area (or volume) that evoked at least one of the assessed muscles (MELGARI *et al.*, 2008; NAZAROVA *et al.*, 2021):

$$\mathrm{X}_{\mathrm{OD-2\ muscles}} = \frac{\mathrm{X}_{12}.100\%}{\mathrm{X}_1 + \mathrm{X}_2 - \mathrm{X}_{12}} \quad (1)$$

Where X can be area or volume, and the indices 1, 2, and 3 (equation below) refer to each of the muscle maps (target and adjacent) and their corresponding overlaps (pairs of indices). The OD was categorized as: 0-20% (negligible); 21-40% (low); 41-60% (medium); 61-80% (high); 81-100% (very high). The relative

number of subjects with OD in each of these categories was calculated for all overlap maps. Similarly, the OD of three muscle motor maps were computed as:

$$X_{\text{OD–3 muscles}} = \frac{X_{123} \cdot 100\%}{X_1 + X_2 + X_3 - (X_{12} + X_{13} + X_{23}) + X_{123}} \quad (2)$$

Statistical analysis

All parameters were normalized relative to their maximum values within each individual to enable a direct comparison between conditions and subjects. The stimulation intensity, target, and adjacent muscle and each map parameter (area and volume OD, EMD, and the centroid Euclidean distance) were modeled as fixed effects. In turn, the subjects were modeled as a random effect in a linear mixed-effects model. A random structure of the model was selected based on hierarchical sequential testing with each model fit using likelihood-ratio tests. The chosen model was recomputed using restricted maximum likelihood estimation and the p-values for fixed effects derived with Satterthwaite approximations in a Type III Analysis of Variance table. When appropriate, posthoc multiple comparisons were performed with estimated marginal means with p-value correction for the false discovery rate. The rMT across subjects (random) and muscles (fixed) were also analyzed using a linear mixed-effects model, and multiple comparisons were performed using the Tukey simultaneous tests for the difference of means. Critical deviations from normality were assessed with the residuals' Q–Q plots, and homoscedasticity was inspected with a standard versus fitted values plot. Statistical analysis was performed in R 3.6 (R Core Team, Vienna, Austria) using the *lme4* 1.1, *afex* 0.25 packages, and *emmeans* 1.4 packages. The level of statistical significance was set at 0.05.

Results

Overlap degree and rMT

The rMT varied across muscles ($p = 0.039$) and within subjects ($p = 0.015$), being higher for the FCR compared to the FPB muscle ($p = 0.042$) and similar when comparing ADM with FCR ($p = 0.120$) or FPB ($p = 0.852$) muscles. We computed nine overlap maps for each subject: six overlap maps of two muscles and three overlaps of three muscles. The subscript [*tg*] refers to the target and [*adj*] to the adjacent muscles. The relative number of subjects for each OD

category is illustrated in Figure 2. More than 60% of the subjects had medium to very high area OD but negligible to low volume OD. Maps of two muscles had more subjects with higher ODs than those of three muscles at both stimulation intensities. The number of subjects with high area OD of all maps was higher at 120% than at 110% rMT stimulation intensity.

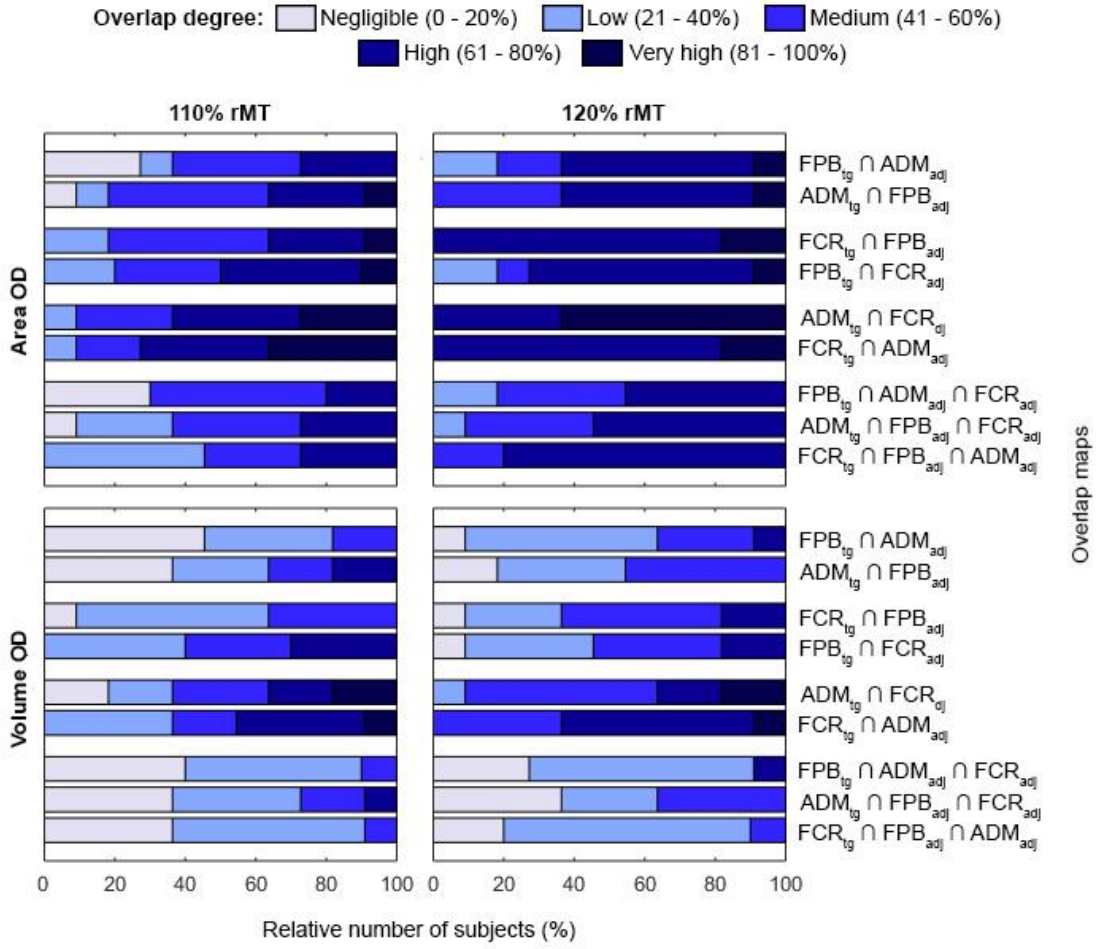

Fig. 2 Relative number of subjects with OD distributed in 5 categories (negligible, low, medium, high and very high) for all overlap maps and at stimulation intensities of 110% (left) and 120% (right) of rMT. The length of the horizontal bars indicates the relative number of subjects with each OD, and the ∩ (intersection) symbol represents the overlap between muscles.

The effect of stimulation intensity, target and adjacent muscle on map size and topography

Table 1 presents the results of the linear mixed-effects model. The size parameters (area and volume OD) were significantly affected by the stimulation intensity, the target and adjacent muscle individually, and their interaction. In turn,

the topography parameters (EMD and the centroid Euclidean distance) were significantly affected only by the adjacent muscle but not by the stimulation intensity nor the target muscle. The interaction between stimulation intensity and target muscle affected both topography parameters, while the interaction between target and adjacent muscles affected only the EMD.

Table 1 The linear mixed-effects model results for size (area and volume OD) and topography (EMD and centroid Euclidean distance) parameters. Abbreviations: degrees of freedom (DoF), stimulation intensity (SI), target (M_{tg}), and adjacent muscle (M_{adj}). The * indicates *p*-value < 0.05

Effect	**DoF (numerator, denominator)**	***F*-value**	***p*-value**	**DoF (numerator, denominator)**	***F*-value**	***p*-value**
	Area OD			**Volume OD**		
SI	(1, 10.0)	19.99	0.001*	(1, 9.96)	5.85	0.036*
M_{tg}	(2, 10.7)	8.61	0.006*	(2, 10.9)	11.82	0.002*
M_{adj}	(3, 137.4)	45.77	<0.001*	(3, 136.0)	70.35	<0.001*
SI x M_{tg}	(2, 137.9)	0.82	0.444	(2, 136.6)	0.06	0.945
SI x M_{adj}	(3, 137.4)	0.09	0.964	(3, 135.9)	1.11	0.348
M_{tg} x M_{adj}	(3, 137.4)	7.02	<0.001*	(3, 136.0)	13.01	0.000*
SI x M_{tg} x M_{adj}	(3, 137.5)	1.30	0.276	(3, 136.0)	0.70	0.553
	Centroid Euclidean distance			**EMD**		
SI	(1, 11.0)	0.02	0.890	(1, 10.1)	1.65	0.228
M_{tg}	(2, 11.1)	0.39	0.688	(2, 14.5)	2.76	0.096
M_{adj}	(3, 146.9)	4.49	0.005*	(3, 147.5)	5.57	0.001*
SI x M_{tg}	(2, 147.1)	4.06	0.019*	(2, 147.9)	3.16	0.045*
SI x M_{adj}	(3, 146.9)	0.31	0.819	(3, 147,4)	0.28	0.836
M_{tg} x M_{adj}	(3, 146.9)	1.32	0.270	(3, 147.5)	4.82	0.003*
SI x M_{tg} x M_{adj}	(3, 146.9)	1.41	0.241	(3, 147.6)	0.55	0.646

The multiple comparisons are presented in Tables 2-4, and the means and standard deviations across subjects for each parameter of all overlap maps area are illustrated in Figure 3. For most overlaps, the area OD was significantly higher at 120% than at 110% rMT of stimulation intensity. The intensity effect was only significant at the volume OD factor level, whereas none of the multiple comparisons displayed any significant differences. When comparing different target or adjacent muscles, the highest area and volume ODs were between ADM

and FCR. In turn, overlaps involving FPB did not show any significant differences when compared to the overlap between the three muscles together. This result applies to both stimulation intensities in most cases. Lastly, the EMD and centroid Euclidean distance were similar for both tested stimulation intensities and all comparisons across adjacent and target muscles.

Table 2 Multiple comparisons of area OD, volume OD, centroid's Euclidean distance, and EMD between the stimulation intensities (110% compared with 120% of rMT) for each combination of target and adjacent muscles.

Target Muscle	**Adjacent Muscle**							
	Area OD				**Volume OD**			
	ADM	FPB	FCR	ALL	ADM	FPB	FCR	ALL
ADM	x	0.937	0.016*	0.062	x	1.000	0.411	1.000
FPB	0.003*	x	0.073	0.006*	0.074	x	1.000	0.327
FCR	0.044*	0.003*	x	0.004*	0.090	0.573	x	1.000
	Centroid's Euclidean Distance				**EMD**			
	ADM	FPB	FCR	ALL	ADM	FPB	FCR	ALL
ADM	x	0.698	1.000	0.522	x	1.000	1.000	1.000
FPB	1.000	x	1.000	1.000	0.587	x	1.000	0.588
FCR	1.000	1.000	x	0.925	1.000	0.588	x	0.588

Table 3 Multiple comparisons of area OD, volume OD, centroid's Euclidean distance, and EMD between different target muscles for each adjacent muscle and stimulation intensity (% of rMT).

Muscles			**Area OD**		**Volume OD**		**Centroid's Euclidean distance**		**EMD**	
			Intensity (% rMT)							
Target 1	**Target 2**	**Adjacent**	**110**	**120**	**110**	**120**	**110**	**120**	**110**	**120**
FPB	FCR	ADM	0.001*	0.006*	<0.001*	<0.001*	1.000	1.000	0.053	0.157
ADM	FCR	FPB	1.000	0.102	1.000	0.662	0.878	0.826	1.000	0.253
ADM	FPB	FCR	0.011*	0.003*	0.444	0.115	1.000	1.000	0.697	1.000

ADM	FPB	ALL	0.212	0.890	0.513	1.000	1.000	0.826	1.000	1.000
ADM	FCR	ALL	1.000	0.434	1.000	1.000	0.826	0.801	1.000	1.000
FPB	FCR	ALL	0.307	0.230	0.513	1.000	1.000	1.000	1.000	1.000

Table 4 Multiple comparisons of area OD, volume OD, centroid's Euclidean distance, and EMD between different adjacent muscles for each target muscle and stimulation intensity (% of rMT).

Muscles			Area OD		Volume OD		Centroid's Euclidean distance		EMD	
			Intensity (% rMT)							
Target	**Adjacent 1**	**Adjacent 2**	**110**	**120**	**110**	**120**	**110**	**120**	**110**	**120**
ADM	FPB	FCR	0.001*	<0.001*	<0.001*	<0.001*	1.000	0.522	1.000	0.253
ADM	FPB	ALL	0.309	0.503	0.444	0.345	1.000	1.000	1.000	0.209
ADM	FCR	ALL	<0.001*	<0.001*	<0.001*	<0.001*	1.000	0.449	1.000	1.000
FPB	ADM	FCR	0.062	1.000	<0.001*	0.066	0.826	1.000	0.209	0.588
FPB	ADM	ALL	0.503	0.212	0.899	0.327	1.000	1.000	0.109	0.086
FPB	FCR	ALL	0.004*	0.083	<0.001*	<0.001*	0.826	1.000	1.000	0.733
FCR	ADM	FPB	0.001*	0.044*	0.001*	<0.001*	0.522	0.925	0.253	1.000
FCR	ADM	ALL	<0.001*	<0.001*	<0.001*	<0.001*	0.463	0.878	0.697	1.000
FCR	FPB	ALL	0.096	0.086	0.042*	0.003*	1.000	1.000	1.000	1.000

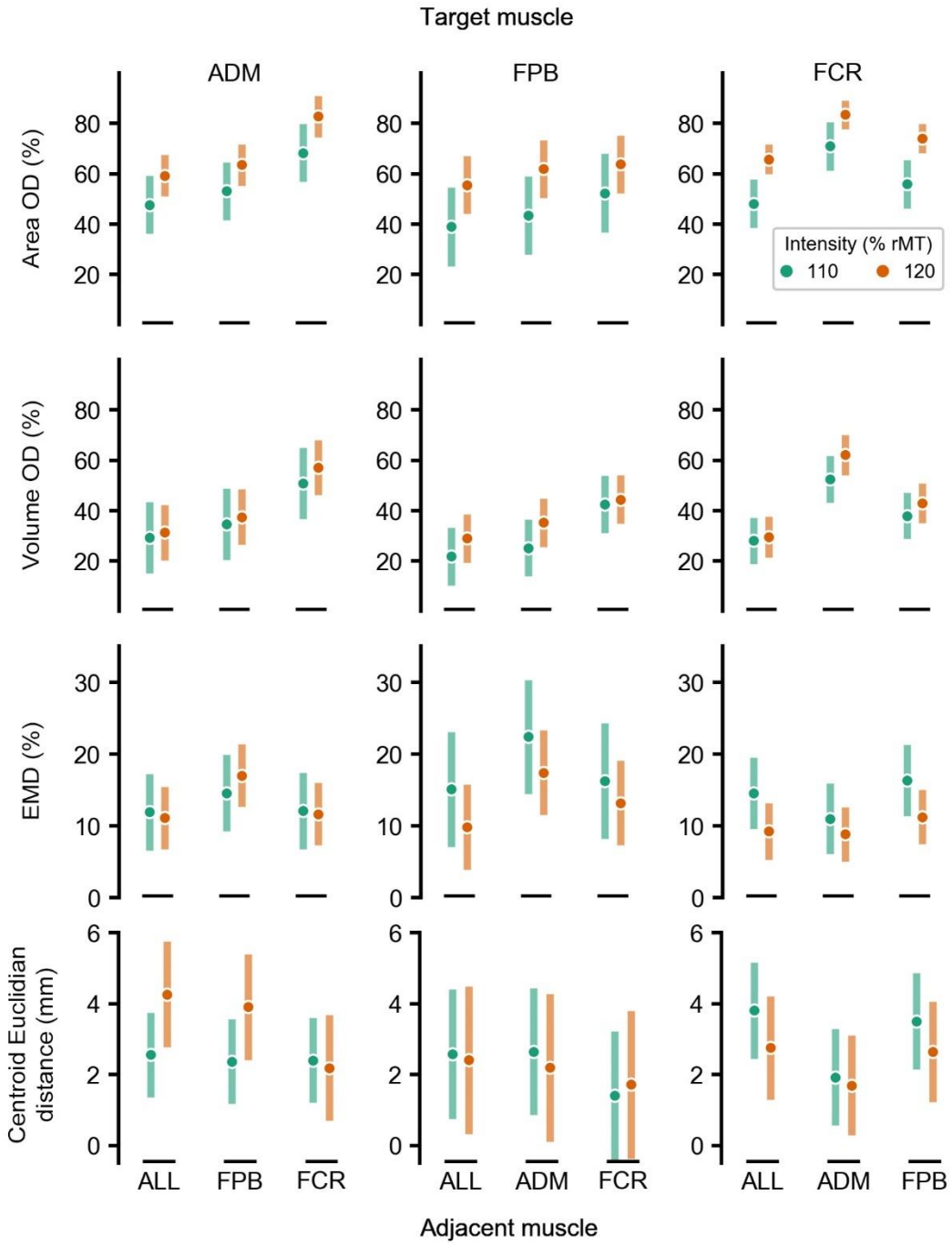

Fig. 3 Mean and standard deviation of the motor maps' size and topography parameters across the 11 subjects. The rows and columns of the chart grid contain the map parameters and the target muscle, respectively. The green and orange colors represent 110% and 120% of the rMT stimulation intensity. The term ALL refers to the overlap of the target with both adjacent muscles simultaneously

Discussion

In this study, we demonstrate that the motor map parameters vary significantly between the pairs of muscles in size (area and volume) but not in topography (EMD and centroid Euclidean distance). While area OD of the muscle's pairs was mainly medium to very high, volume OD was negligible to low. Our results also show that increasing the stimulation intensity from 110% to 120% of the rMT causes a significant increase in the area OD among different muscles. In turn, changing the stimulation intensity does not affect the map topographies. The volume OD does not seem to increase with the stimulus intensity, possibly due to OD variations between subjects and muscles.

The effect of TMS intensity on the map parameters

Lower stimulation intensities resulted in a motor representation with more restricted sites of muscle activation than higher intensities, as depicted in Figure 4. One likely interpretation is that the weaker intensity might not recruit the less excitable neuronal populations (KALLIONIEMI; JULKUNEN, 2016). When studying the functional overlapping of muscles with different motor thresholds, one might observe that M1 is organized by discrete or slightly overlapping representations. In each M1 representation site, the target muscle can be overlapped with different adjacent muscles that may be related to distinct synergies and, therefore, contribute to various movements. This association might point towards the functional organization of M1 (MASSÉ-ALARIE *et al.*, 2017).

In turn, higher stimulation intensities are associated with stronger magnetic fields spanning a larger cortical region (VAN DE RUIT; GREY, 2016) and reflect in smoother motor maps that may lead to two outcomes. First, the higher intensity may excite neuronal populations located further from the region of interest, recruited indirectly from the excitation of intracortical neurons, thus producing progressively larger motor map areas (NIEMINEN *et al.*, 2019b; SCHIEBER, 2001). This stimulation leakage may overestimate the muscle representations and the region-of-interest muscle representation overlap, losing the specificity of the studied movement. Secondly, the higher intensity may delineate the full extent of the muscles' motor representation, providing a complete picture of the muscle group coactivation. In summary, coactivation maps obtained from lower and higher stimulation intensities might provide complementary perspectives on the

M1's functional organization. The stimulation intensity needs to be carefully chosen to account for the synergy when mapping the representation of different muscles, especially in pre-surgical applications where the mapping methods must be the most accurate possible (KRIEG *et al.*, 2017).

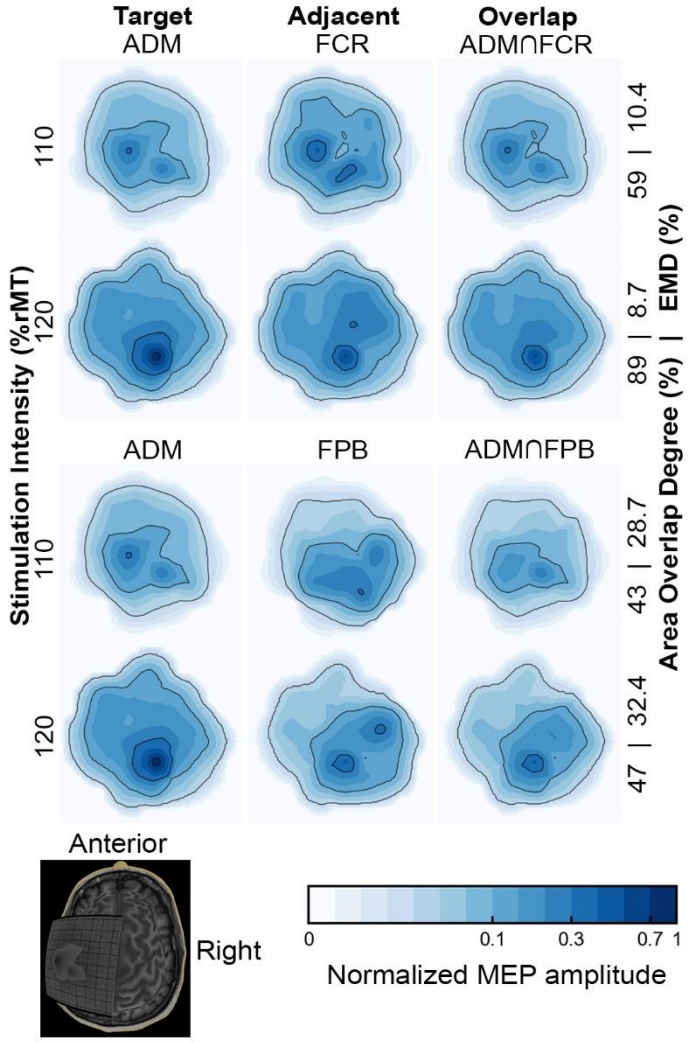

Fig. 4 Normalized motor maps of a representative subject with low and high area and topographic similarity, and MEP amplitude affected by a higher TMS intensity. The contour line indicates the 5, 30, and 70% of the maximal MEP amplitude. Note that the map size and the area OD, but not the EMD, is significantly higher at 120% than in 110% of rMT. In addition, the increase in the area OD is greater when the EMD is lower, i.e., when the maps of the target and adjacent muscles have a more remarkable similarity. The ∩ (intersection) symbol represents the overlap between muscles.

A stimulation intensity of 120% of rMT resulted in larger representation areas of the target and adjacent muscles, corroborating previous findings (JULKUNEN, 2014b; KALLIONIEMI; JULKUNEN, 2016; THORDSTEIN *et al.*, 2013; VAN DE RUIT; GREY, 2016). The increase in the OD is due to a higher spatial overlap between the two cortical maps than in the total area encompassed by two (or three) maps individually, as illustrated in Figure 5. Regardless of the higher overlap, the spatial distributions remain similar, and the most excitable regions of the cortex for a particular muscle seem to stay the same. Our results align with a previous study showing that an increase in stimulation intensity changes the extension of the motor representation but keeps similar topographies and centroids (VAN DE RUIT; GREY, 2016).

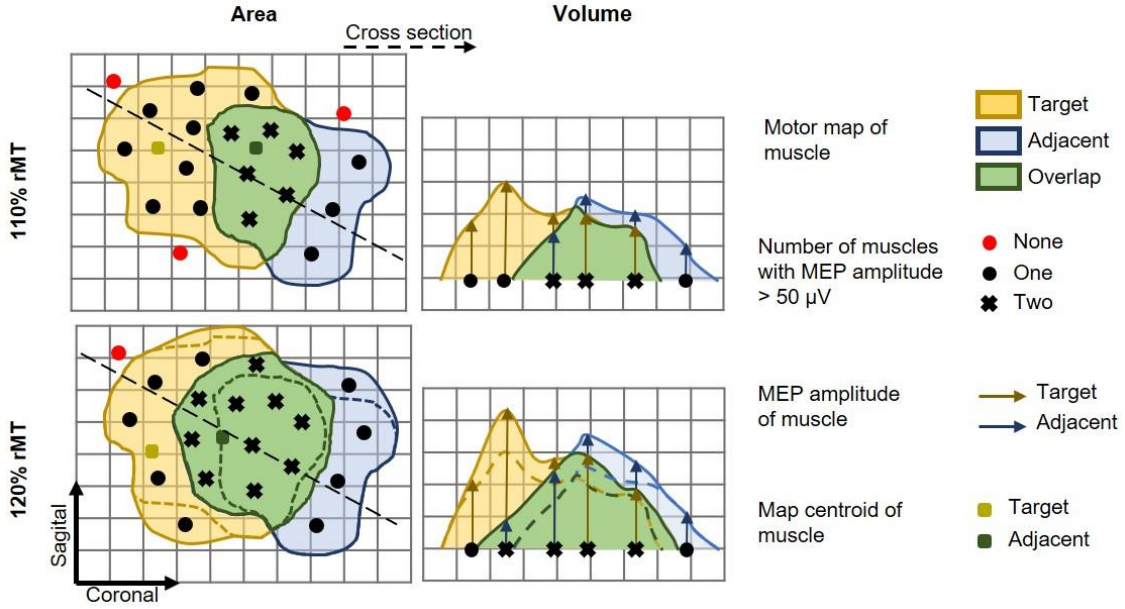

Fig. 5 Schematic illustration of the effect of the stimulation intensity on the individual and overlap maps. In the left panel, the motor map area, and on the right, a cross-section represents the map's height profile (MEP amplitude). Note that, at a higher stimulation intensity (120% rMT), the increase in the number of stimulation sites resulting in MEP amplitudes greater than 50 µV (black markers) from one (circle) to two (cross) muscles was more pronounced than the increase from none to one muscle. Thus, even though all maps (target and adjacent muscle and overlap) showed an increase in area, the overlap map increased more than the total map

The cortical representation overlapping of a carpal and intrinsic hand muscles

We observed a higher overlapping between the forearm (FCR) and both intrinsic hand muscles (ADM or FPB) than between the intrinsic themselves. In addition, the centroids of the hand muscle representations are further away than those between the forearm and hand muscles. In contrast, a previous study observed higher levels of overlapping among the representations of intrinsic hand muscles when compared to those obtained between them and the carpal forearm muscles (MELGARI *et al.*, 2008; NAZAROVA *et al.*, 2021). Possibly, this difference is because the subjects in our study kept their hands in a neutral posture, offering distinct proprioceptive feedback from that generated in maintaining the pronated posture (GRAZIANO, 2006), as adopted in the study by (MELGARI *et al.*, 2008). The hand posture is implicitly related to grasping and the corresponding body movements (PEREZ; ROTHWELL, 2015). The influence of the hand posture on overlapping was previously associated with a dynamic modification in the neuronal network structure related to motor control (MELGARI *et al.*, 2008; PEREZ; ROTHWELL, 2015; RAFFIN; SIEBNER, 2019). Furthermore, the higher rMT of the forearm compared to the hand muscles may contribute to the observed higher overlap, while the low rMT of FPB may only partially stimulate adjacent muscles with higher rMT. In this sense, our results suggest that different muscles have cortical areas preferentially shared with specific muscles, as depicted in Figure 6.

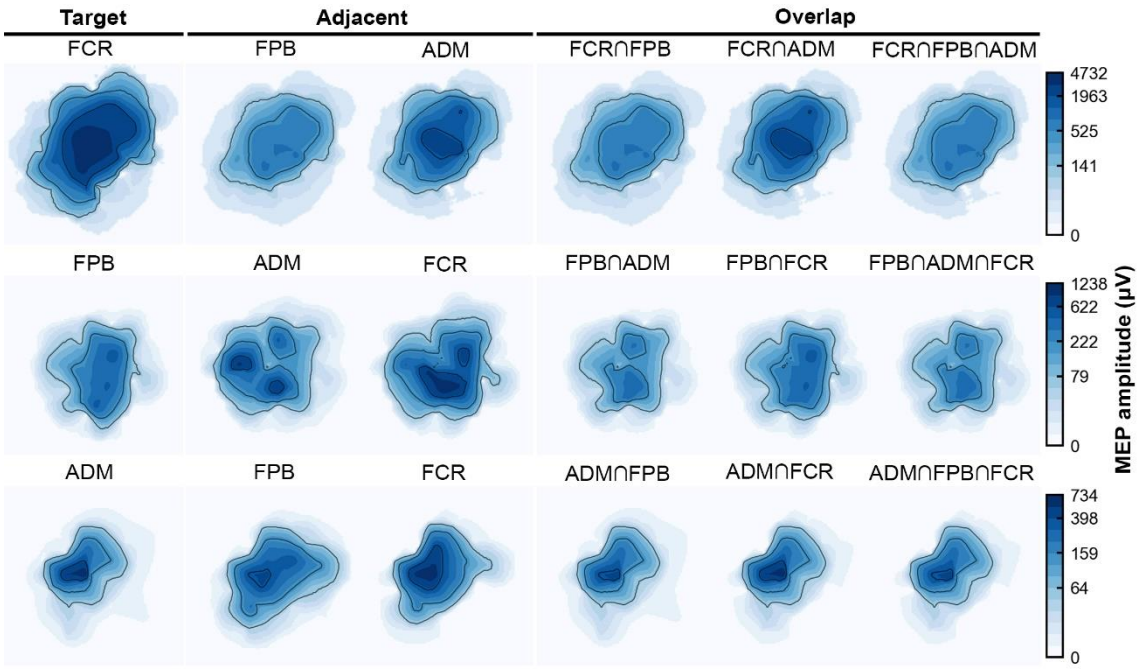

Fig. 6 Motor maps of a representative subject at a stimulation intensity of 120% rMT, comparing topography, size, and MEP amplitudes of all possible combinations of ADM, FPB, and FCR muscle maps. The map's anatomical references are the same as in Figure 4. The ∩ (intersection) symbol represents the overlap between muscles.

We associate the high overlap in motor representations of upper limb muscles to a functionally organized M1 hypothesis. Our view is in agreement with previous studies that investigated the organization pattern of M1 through the nTMS motor overlapping (MARCONI *et al.*, 2007; MELGARI *et al.*, 2008; NAZAROVA *et al.*, 2021; WASSERMANN *et al.*, 1992b; WILSON; THICKBROOM; MASTAGLIA, 1993), and functional MRI in humans (INDOVINA; SANES, 2001; LEO *et al.*, 2016). As we expected, our results revealed that the OD was smaller but still significant when both hand and forearm muscles were overlapped. This may indicate that increasing the number of overlapped motor representations reduces the overlapping degrees, resulting in greater specificity of the evoked synergies. Despite the highly overlapped representations, we have not focused on whether it reflects the ability to perform fine movements, as previous studies interpreted as indications of functional reorganization of M1 (PEARCE *et al.*, 2000; TYC; BOYADJIAN, 2005). However, this factor could be

associated with different OD among subjects and may be tested in the future through parallel behavioral approaches.

The substantial overlapping is possibly explained by how the M1 seems to encode movements and muscle recruitment. Individual muscles appear to be recruited by a complex neuronal network instead of an individualized set of neurons, connected by a set of synergies responsible for a wide range of movements and tasks (GENTNER; CLASSEN, 2006; LEO *et al.*, 2016). Such motor representation is given by groups of functionally related neurons (KLOCHKOV *et al.*, 2018) following two possible mechanisms: convergence and divergence. In the convergence mechanism, a muscle has its motor representation on separate sites over M1, i.e., each site is probably overlapped with the motor representation of different groups of muscles and, thus, associated with various movements (MASSÉ-ALARIE *et al.*, 2017; SCHIEBER, 2001). In the divergence mechanism, one site can elicit several muscles simultaneously with different intensities according to their performed movement (MELGARI *et al.*, 2008; SCHIEBER, 2001).

The divergence mechanism is observed through connections between specific pyramidal neurons and motoneurons associated with different muscles (SCHIEBER, 2001). Such a phenomenon could be related to the shared innervation between FPB with both ADM and FCR. The FPB is a hypothenar muscle composed of a superficial and a deep head that have different innervations. The deep head of the FPB is innervated by the ulnar nerve, the same innervation of the ADM. The superficial head of the FPB has the same innervation as the FCR, the median nerve (VISHRAM, 2014). It possibly relates to the OD in the cortical representation. The action potential generated in the cortical site associated with the FPB propagates through similar pathways, resulting in a simultaneous contraction of the muscles with shared innervations. Therefore, the significant area OD probably resulted from the divergence of the overlapping motor representation indicating the synergism between the studied muscles. Animal studies further support such a view. For instance, cortical motor neurons in cats are connected to neurons of multiple muscles, not as the expected point-to-point connectivity. The synergistic interactions between neuronal populations in different cortical sites might generate descending volleys

influencing various movements through the recruitment of multiple muscles (CAPADAY *et al.*, 2009).

Methodological considerations

Despite the evident extension of the overlapping representation of muscles on M1, the focality of the TMS is challenging to estimate, and stimulation can propagate over regions responsible for adjacent muscles that can contribute to a high OD (FRICKE *et al.*, 2017; SCHIEBER, 2001). However, simple models based on the coil's center projection, like the one used in this experiment, have more than 85% accuracy and can delineate the cortical motor representation, but the stimulus propagation in the realistic cortical geometry is still disregarded (SEYNAEVE *et al.*, 2019).

We should note that the EMG crosstalk in the pseudo-monopolar montage may contaminate the cortical motor representations. However, the electrode over the innervation zone might detect the direct neural drive to the muscle alleviating the crosstalk for the intrinsic hand muscles (superficial fibers running parallel to the skin) and the FCR muscle we studied (GARCIA *et al.*, 2020; GARCIA; SOUZA; VARGAS, 2017). Also, the cortical overlaps between the forearm and intrinsic hand muscle are more prominent than the overlap within intrinsic muscles. Thus, considering that the hand muscles are closely located and have bigger crosstalk between each other (SELVANAYAGAM; RIEK; CARROLL, 2012), our findings are significant despite this limitation and would only be further supported by reducing the potential crosstalk.

We used 100 µV MEP amplitude as a reference to estimate the rMT. The 110% and 120% of rMT stimulation intensities may correspond to slightly higher stimulator outputs when compared to protocols using 50 µV MEP amplitude. Nonetheless, our key results are the changes in motor map parameters and overlap relative to the increase in the stimulation, which are likely to occur regardless of the small deviation from the stimulator output. Moreover, the adopted protocol ensured consistent MEPs for a relatively small number of trials in each location coil location during the motor mapping procedure. We should note that only one set of muscles linked to the manual grasp movement was assessed. Our results may not generalize to muscle groups with different

movement refinement, such as the lower limbs. Even so, we provide an important systemic perspective on how to evaluate the cortical motor representation.

Conclusion

We aimed at understanding the cortical motor organization of three muscles linked to the grasping movement. Our results showed a higher cortical representation overlapping between the carpal forearm and both intrinsic hand muscles than between the intrinsic themselves. Stronger stimulation intensities led to higher overlap in the map areas but did not affect the volume and the map topographies. Our study contributes to a more detailed representation of the motor cortex associated with the functional arrangement among muscles, implying a synergistic spatial organization. Understanding the coactivation of muscle groups may provide accurate functional maps over M1. Finally, spatially accurate cortical motor mapping with nTMS can have an immediate clinical impact, for instance, when defining the eloquent brain regions during pre-surgical planning. Avoiding highly overlapped areas associated with muscular synergy would minimize deficits in the patients' motor function (LEFAUCHEUR; PICHT, 2016; THARIN; GOLBY, 2007).

References

Bashir S, Perez JM, Horvath JC, Pascual-Leone A (2013) Differentiation of Motor Cortical Representation of Hand Muscles by Navigated Mapping of Optimal TMS Current Directions in Healthy Subjects. Journal of Clinical Neurophysiology 30:390–395. https://doi.org/10.1097/WNP.0b013e31829dda6b

Capaday C, Ethier C, Brizzi L, et al (2009) On the nature of the intrinsic connectivity of the cat motor cortex: Evidence for a recurrent neural network topology. Journal of Neurophysiology 102:2131–2141. https://doi.org/10.1152/jn.91319.2008

Cavaleri R, Schabrun SM, Chipchase LS (2018) The reliability and validity of rapid transcranial magnetic stimulation mapping. Brain Stimulation 11:1291–1295. https://doi.org/10.1016/j.brs.2018.07.043

Cheung VCK, Turolla A, Agostini M, et al (2012) Muscle synergy patterns as physiological markers of motor cortical damage. Proceedings of the National Academy of Sciences of the United States of America 109:14652–14656. https://doi.org/10.1073/pnas.1212056109

Conforto AB, Z'Graggen WJ, Kohl AS, et al (2004) Impact of coil position and electrophysiological monitoring on determination of motor thresholds to transcranial magnetic stimulation. Clinical Neurophysiology 115:812–819. https://doi.org/10.1016/j.clinph.2003.11.010

Devanne H, Cassim F, Ethier C, et al (2006) The comparable size and overlapping nature of upper limb distal and proximal muscle representations in the human motor cortex. European Journal of Neuroscience 23:2467–2476. https://doi.org/10.1111/j.1460-9568.2006.04760.x

Frey D, Schilt S, Strack V, et al (2014) Navigated transcranial magnetic stimulation improves the treatment outcome in patients with brain tumors in motor eloquent locations. Neuro-Oncology 16:1365–1372. https://doi.org/10.1093/neuonc/nou110

Fricke C, Gentner R, Alizadeh J, Classen J (2020) Linking Individual Movements to a Skilled Repertoire: Fast Modulation of Motor Synergies by Repetition of Stereotyped Movements. Cerebral Cortex 30:1185–1198. https://doi.org/10.1093/cercor/bhz159

Fricke C, Gentner R, Rumpf JJ, et al (2017) Differential spatial representation of precision and power grasps in the human motor system. NeuroImage 158:58–69. https://doi.org/10.1016/j.neuroimage.2017.06.080

Friston K, Ashburner J, Kiebel S, et al (2006) Statistical Parametric Mapping: The Analysis of Functional Brain Images, 1st Editio. Academic Press

Garcia MAC, Souza VH, Lindolfo-Almas J, et al (2020) Motor potential evoked by transcranial magnetic stimulation depends on the placement protocol of recording electrodes: A pilot study. Biomedical Physics and Engineering Express 6:047003. https://doi.org/10.1088/2057-1976/ab950a

Garcia MAC, Souza VH, Vargas CD (2017) Can the Recording of Motor Potentials Evoked by Transcranial Magnetic Stimulation Be Optimized? Frontiers in Human Neuroscience 11:1–4. https://doi.org/10.3389/fnhum.2017.00413

Gentner R, Classen J (2006) Modular Organization of Finger Movements by the Human Central Nervous System. Neuron 52:731–742. https://doi.org/10.1016/j.neuron.2006.09.038

Gentner R, Gorges S, Weise D, et al (2010) Encoding of motor skill in the corticomuscular system of musicians. Current Biology 20:1869–1874. https://doi.org/10.1016/j.cub.2010.09.045

Graziano M (2006) The Organization of Behavioral Repertoire in Motor Cortex. The Annual Review of Neuroscience 29:105–134. https://doi.org/10.1146/annurev.neuro.29.051605.112924

Groppa S, Oliviero A, Eisen A, et al (2012) A practical guide to diagnostic transcranial magnetic stimulation: Report of an IFCN committee. Clinical Neurophysiology 123:858–882. https://doi.org/10.1016/j.clinph.2012.01.010

Huffmaster XSLA, Iii GMVA, Luchies CW, Cheney XD (2018) Muscle Synergies Obtained from Comprehensive Mapping of the Cortical Forelimb Representation Using Stimulus Triggered Averaging of EMG Activity. The Journal of Neuroscience 38:8759–8771. https://doi.org/10.1523/JNEUROSCI.2519-17.2018

Indovina I, Sanes JN (2001) On somatotopic representation centers for finger movements in human primary motor cortex and supplementary motor area. Neuroimage 13:1027–1034. https://doi.org/10.1006/nimg.2001.0776

Jonker ZD, Vliet R van der, Hauwert CM, et al (2018) TMS motor mapping: Comparing the absolute reliability of digital reconstruction methods to the golden standard. Brain Stimulation 12:309–313. https://doi.org/10.1016/j.brs.2018.11.005

Julkunen P (2014) Methods for estimating cortical motor representation size and location in navigated transcranial magnetic stimulation. Journal of Neuroscience Methods 232:125–133. https://doi.org/10.1016/j.jneumeth.2014.05.020

Kallioniemi E, Julkunen P (2016) Alternative Stimulation Intensities for Mapping Cortical Motor Area with Navigated TMS. Brain Topography 29:395–404. https://doi.org/10.1007/s10548-016-0470-x

Klochkov AS, Khizhnikova AE, Nazarova MA, Chernikova LA (2018) Pathological Upper Limb Synergies of Patients with Poststroke Hemiparesis. Neuroscience and Behavioral Physiology 48:. https://doi.org/10.1007/s11055-018-0634-0

Krieg SM, Lioumis P, Mäkelä JP, et al (2017) Protocol for motor and language mapping by navigated TMS in patients and healthy volunteers; workshop report. Acta Neurochirurgica 159:1187–1195. https://doi.org/10.1007/s00701-017-3187-z

Latash ML, Scholz JP, Schöner G (2007) Toward a new theory of motor synergies. Motor Control 11:276–308

Lefaucheur JP, Picht T (2016) The value of preoperative functional cortical mapping using navigated TMS. Neurophysiologie Clinique 46:125–133. https://doi.org/10.1016/j.neucli.2016.05.001

Leo A, Handjaras G, Bianchi M, et al (2016) A synergy-based hand control is encoded in human motor cortical areas. eLife 5:e13420. https://doi.org/10.7554/eLife.13420

Marconi B, Pecchioli C, Koch G, Caltagirone C (2007) Functional overlap between hand and forearm motor cortical representations during motor cognitive tasks. Clinical Neurophysiology 118:1767–1775. https://doi.org/10.1016/j.clinph.2007.04.028

Massé-Alarie H, Bergin MJG, Schneider C, et al (2017) “Discrete peaks” of excitability and map overlap reveal task-specific organization of primary motor cortex for control of human forearm muscles. Human Brain Mapping 38:6118–6132. https://doi.org/10.1002/hbm.23816

Melgari J, Pasqualetti P, Pauri F, Rossini PM (2008) Muscles in ‘“ Concert ”’: Study of Primary Motor Cortex Upper Limb Functional Topography. PLoS ONE 3:e3069. https://doi.org/10.1371/journal.pone.0003069

Nazarova M, Novikov P, Ivanina E, et al (2021) Mapping of multiple muscles with transcranial magnetic stimulation: absolute and relative test–retest reliability. Human Brain Mapping 42:1–21. https://doi.org/10.1002/hbm.25383

Nielsen JF (1996) Logarithmic distribution of amplitudes of compound muscle action potentials evoked by transcranial magnetic stimulation. Journal of Clinical Neurophysiology 13:423–434. https://doi.org/10.1097/00004691-199609000-00005

Nieminen JO, Koponen LM, Ilmoniemi RJ (2015) Experimental Characterization of the Electric Field Distribution Induced by TMS Devices. Brain Stimulation 8:582–589. https://doi.org/10.1016/j.brs.2015.01.004

Nieminen JO, Koponen LM, Mäkelä N, et al (2019) Short-interval intracortical inhibition in human primary motor cortex: A multi-locus transcranial magnetic stimulation study. NeuroImage 203:116194. https://doi.org/10.1016/j.neuroimage.2019.116194

Nogueira-Campos AA, Oliveira LAS de, Della-Maggiore V, et al (2014) Corticospinal Excitability Preceding the Grasping of Emotion-Laden Stimuli. PLOS One 9:e94824. https://doi.org/10.1371/journal.pone.0094824

Novikov PA, Nazarova MA, Nikulin V v. (2018) TMSmap – Software for Quantitative Analysis of TMS Mapping Results. Frontiers in Human Neuroscience 12:239. https://doi.org/10.3389/fnhum.2018.00239

Overduin SA, d'Avella A, Carmena JM, Bizzi E (2012) Microstimulation Activates a Handful of Muscle Synergies. Neuron 76:1071–1077. https://doi.org/10.1016/j.neuron.2012.10.018

Pearce A, Thickbroom GW, Byrnes ML, Mastaglia FL (2000) Functional Organisation of the Corticomotor Projection to the Hand in Skilled Functional reorganisation of the corticomotor projection to the hand in skilled racquet players. Experimental Brain Research 130:238–243. https://doi.org/10.1007/s002219900236

Pellegrini M, Zoghi M, Jaberzadeh S (2018) The effect of transcranial magnetic stimulation test intensity on the amplitude, variability and reliability of motor evoked potentials. Brain Research 1700:190–198. https://doi.org/10.1016/j.brainres.2018.09.002

Penfield W, Rasmussen T (1950) The Cerebral Cortex of Man. MacMillan New York

Perez MA, Rothwell JC (2015) Distinct influence of hand posture on cortical activity during human grasping. Journal of Neuroscience 35:4882–4889. https://doi.org/10.1523/JNEUROSCI.4170-14.2015

Picht T, Frey D, Thieme S, et al (2016) Presurgical navigated TMS motor cortex mapping improves outcome in glioblastoma surgery: a controlled observational study. Journal of Neuro-Oncology 126:535–543. https://doi.org/10.1007/s11060-015-1993-9

Raffin E, Siebner HR (2019) Use-Dependent Plasticity in Human Primary Motor Hand Area : Synergistic Interplay Between Training and Immobilization. Cerebral Cortex 29:356–371. https://doi.org/10.1093/cercor/bhy226

Romero JR, Ramirez DM, Aglio LS, Gugino LD (2011) Brain mapping using transcranial magnetic stimulation. Neurosurgery Clinics of North America 22:141–152. https://doi.org/10.1016/j.nec.2010.11.002

Rubner Y, Tomasi C, Guibas LJ (1998) The Earth Mover's Distance as a Metric for Image Retrieval. International Journal of Computer Vision 40:99–121. https://doi.org/https://doi.org/10.1023/A:1026543900054

Schieber MH (2001) Constraints on somatotopic organization in the primary motor cortex. Journal of Neurophysiology 86:2125–2143. https://doi.org/10.1152/jn.2001.86.5.2125

Selvanayagam VS, Riek S, Carroll TJ (2012) A systematic method to quantify the presence of cross-talk in stimulus-evoked EMG responses: Implications for TMS studies. Journal of Applied Physiology 112:259–265. https://doi.org/10.1152/japplphysiol.00558.2011

Seynaeve L, Haeck T, Gramer M, et al (2019) Optimized preoperative motor cortex mapping in brain tumors using advanced processing of transcranial magnetic stimulation data. NeuroImage: Clinical 21:101657 Contents. https://doi.org/10.1016/j.nicl.2019.101657

Souza VH, Matsuda RH, Peres ASC, et al (2018) Development and characterization of the InVesalius Navigator software for navigated transcranial magnetic stimulation. Journal of Neuroscience Methods 309:109–120. https://doi.org/10.1016/j.jneumeth.2018.08.023

Souza VH, Vieira TM, Peres ASC, et al (2017) Effect of TMS coil orientation on the spatial distribution of motor evoked potentials in an intrinsic hand muscle. Biomedical Engineering / Biomedizinische Technik 63:635–645. https://doi.org/10.1515/bmt-2016-0240

Strother L, Medendorp WP, Coros AM, Vilis T (2012) Double representation of the wrist and elbow in human motor cortex. European Journal of Neuroscience 36:3291–3298. https://doi.org/10.1111/j.1460-9568.2012.08241.x

Tharin S, Golby A (2007) Functional brain mapping and its applications to neurosurgery. Neurosurgery 60:185–202. https://doi.org/10.1227/01.NEU.0000255386.95464.52

Thordstein M, Saar K, Pegenius G, Elam M (2013) Individual effects of varying stimulation intensity and response criteria on area of activation for different muscles in humans . A study using navigated transcranial magnetic stimulation. Brain Stimulation 6:49–53. https://doi.org/10.1016/j.brs.2012.01.004

Tyc F, Boyadjian A (2005) Motor cortex plasticity induced by extensive training revealed by transcranial magnetic stimulation in human. European Journal of Neuroscience 21:259–266. https://doi.org/10.1111/j.1460-9568.2004.03835.x

van de Ruit M, Grey MJ (2016) The TMS Map Scales with Increased Stimulation Intensity and Muscle Activation. Brain Topography 29:56–66. https://doi.org/10.1007/s10548-015-0447-1

Van De Ruit M, Perenboom MJL, Grey MJ (2015) TMS brain mapping in less than two minutes. Brain Stimulation 8:231–239. https://doi.org/10.1016/j.brs.2014.10.020

Vishram S (2014) Textbook of Anatomy: Upper Limb and Thorax, 2nd edn. Reed Elsevier India Private Limited

Wassermann EM, McShane LM, Hallett M, Cohen LG (1992) Noninvasive mapping of muscle representations in human motor cortex. Electroencephalography and clinical neurophysiology 85:1–8. https://doi.org/10.1016/0168-5597(92)90094-R

Wilson SA, Thickbroom GW, Mastaglia FL (1993) Transcranial magnetic stimulation mapping of the motor cortex in normal subjects. Journal of the Neurological Sciences 118:134–144. https://doi.org/10.1016/0022-510X(93)90102-5

Appendix 1

The cortical motor maps were created in the TMSmap software (NOVIKOV; NAZAROVA; NIKULIN, 2018). The software uses the coil center coordinates to fit the closest spherical surface in the least square sense. It projects them to generate a surface in a region called the patch of interest, where a quasi-regular grid is constructed. Spatial filtering is applied to merge stimulation coordinates located closer than 3 mm to compensate for the inherent errors and fluctuations of the neuronavigation system and to avoid strong influence from outliers. The mean coordinates and the median peak-to-peak MEP amplitudes of the merged coordinates are projected on the grid, and interpolation with a smoothly changing function approach is applied to construct the map. The maximal radius of the stimulation site influence on the cortical surface was set to 15 mm according to the approximate full width at half maximum (FWHM) of the electric field distribution on the cortical surface (NIEMINEN; KOPONEN; ILMONIEMI, 2015b).

The area, volume, and centroid were computed from the cortical motor maps. The map area and volume were calculated according to the equations below:

$$\text{Area} = \sum_{i=1}^{N} \Delta s_i \quad \text{(A1)}$$

$$\text{Volume} = \sum_{i=1}^{N} \text{MEP}_i . \Delta s_i \quad \text{(A2)}$$

where N is the number of square grid elements with area Δs_i and MEP_i is the peak-to-peak amplitude. MEP amplitudes smaller than 50 μV were discarded from the area and volume estimates (GROPPA *et al.*, 2012). The map area represents the extent of the cortical motor representation, and the volume represents the map area weighted by the MEP amplitude. The volume is better described as an effective area. Considering a map within a particular area, the height of the map is the MEP amplitude, and it represents how strong the muscle's response was to the stimuli applied in that area. Comparing two maps with the same area and different volumes, the extent of that muscle's representation on M1 is equal, although the map whose height is higher has stronger muscle recruitment and representation. The centroid was calculated as:

$$\text{centroid} = \left(\frac{\sum_{i=1}^{N}(h_i * s_i * x_i)}{\sum_{i=1}^{N}(h_i * s_i)}, \frac{\sum_{i=1}^{N}(h_i * s_i * y_i)}{\sum_{i=1}^{N}(h_i * s_i)}, \frac{\sum_{i=1}^{N}(h_i * s_i * z_i)}{\sum_{i=1}^{N}(h_i * s_i)} \right) \quad \text{(A3)}$$

where N is the number of grid elements, h_i is the height of the constructed map above the grid element, s_i is the area and x_i, y_i, and z_i are the coordinates of the center of the grid element (NOVIKOV; NAZAROVA; NIKULIN, 2018).

The overlap map was constructed considering the area where MEP amplitudes were greater than 50 μV for all the recorded muscles. The map height is the smallest MEP amplitude across all muscles at each grid element. The area, volume, centroid and EMD for the overlap maps were calculated as described above. The size and topography parameters selected to assess the coactivation between adjacent muscles were area and volume OD, and EMD and centroids Euclidean distance, respectively, as described in Methods.

APPENDIX B – MOTOR POTENTIAL EVOKED BY TRANSCRANIAL MAGNETIC STIMULATION DEPENDS ON THE PLACEMENT PROTOCOL OF RECORDING ELECTRODES: A PILOT STUDY

This article is published at the journal Biomedical Physics & Engineering Express (DOI: 10.1088/2057-1976/ab950a). The reuse of this article in my thesis is in compliance with IOP Copyright policy.

Title: Motor potential evoked by transcranial magnetic stimulation depends on the placement protocol of recording electrodes: a pilot study

Authors: Marco Antonio Cavalcanti Garcia[1,2,3,*], Victor Hugo Souza[3,4], Jordania Lindolfo-Almas[1], Renan Hiroshi Matsuda[3] and Anaelli Aparecida Nogueira-Campos[2]

[1] Programa de Pós-Graduação em Ciências da Reabilitação e Desempenho Físico-Funcional, Faculdade de Fisioterapia, Universidade Federal de Juiz de Fora, Juiz de Fora, Brazil

[2] Laboratório de Neurofisiologia Cognitiva, Instituto de Ciências Biológicas, Universidade Federal de Juiz de Fora, Juiz de Fora, Brazil

[3] Laboratório de Biomagnetismo, Faculdade de Filosofia, Ciências e Letras de Ribeirão Preto, Universidade de São Paulo, Ribeirão Preto, Brazil

[4] Department of Neuroscience and Biomedical Engineering, Aalto University School of Science, Espoo, Finland

Abstract

Objective: There seems to be no consensus in the literature regarding the protocol of surface EMG electrode placement for recording motor potentials (MEP) evoked by transcranial magnetic stimulation (TMS). Thus, the aim of this study was to investigate MEP amplitudes obtained from two different protocols of electrode placement. Methods: Surface electrodes were placed on three upper arm muscles (biceps brachii, flexor carpi radialis and flexor pollicis brevis) of six right-handed subjects following two different protocols (1 and 2), which varied according to the interelectrode distance and location relative to the muscle. TMS

pulses were applied to the hotspot of biceps brachii, while surface electromyographic signals were recorded from the two protocols and for each muscle simultaneously. Main Results: Greater MEP amplitudes were obtained for Protocol 1 compared to Protocol 2 ($P < 0.05$). Significance: Different electrode placement protocols may result in distinct MEP amplitudes, which should be taken into account regarding the intensity adjustments on single and repetitive TMS modalities of stimulation.

Keywords: Motor Evoked Potential, Surface Electromyography, Corticospinal excitability

Introduction

The amplitude of the motor evoked potential (MEP) recorded with surface electromyography (sEMG) is the most common parameter used for determining the intensity of transcranial magnetic stimulation (TMS) in neurophysiological and treatment approaches. MEP amplitude critically depends on the electrode shape, size, placement relative to the muscle fibers, and on the muscle properties such as fiber architecture and size [1-3]. Although there are some recommendations regarding the use of sEMG for many clinical applications [2,4-6], to our best knowledge, there is no consensus concerning the protocol of electrode placement for TMS applications. This methodological issue was recently addressed by Garcia et al. [7], who reinforced the need for standardization on the electrode placement for recording MEPs. Garcia et al. [7] suggested that the electrodes should be placed over the neuromuscular junction and a bony prominence for recording MEPs with maximal amplitudes. In turn, the Surface ElectroMyoGraphy for the Non-Invasive Assessment of Muscles (SENIAM) recommendations [2] for surface electrodes placement was the first proposal for the standardization of sensor location with the aim, among other objectives, of minimizing the crosstalk between electrodes by adjusting the inter-electrode distance depending on the muscle size. As far as we know, there is no previous data on how conventional electrode placement protocols affect the MEP amplitude. If MEP amplitudes vary depending on the placement protocols, the outcome of research and clinical TMS studies might lead to conflicting results. Thus, the present pilot study investigated the effects of the protocols proposed

by SENIAM [2] and Garcia et al. [7] on the MEP amplitude recorded from three upper limb muscles commonly studied with TMS.

Methods

Participants

Six participants, all free of neurological and motor disorders (4 females; 18-49 years old), participated in this study. They all self-reported as right handed for daily living tasks. This study was approved by the local ethical committee (CAEE: 01158218.0.0000.5147) and followed the Declaration of Helsinki. An informed consent was obtained from all participants prior to the experimental session. The information of each participant is presented in Table 1.

Table 1. Descriptive data from each participant.

Participant	Age	Gender	rMT_{RH}	rMT_{LH}
1	26	F	41	42
2	49	M	58	60
3	37	M	53	44
4	25	F	56	60
5	18	F	45	47
6	26	F	45	42

Age (years) ; Gender: Female [F] and Male [M]; Resting Motor Thresholds (rMT) for right (RH – non dominant) and left (LH - dominant) cerebral hemispheres obtained from the minimum TMS intensity required to evoke a motor potential with a peak to peak value of 100 μV.

Surface EMG

Montages

Surface EMG signals were recorded from the biceps brachii (BB), flexor carpi radialis (FCR), and flexor pollicis brevis (FPB) of the right and left upper limbs of each subject using an EMG signal amplifier (EMG System do Brasil Ltda, São José dos Campos, Brazil; model: 410C; gain: 2000, sampling frequency: 3.5 kHz per channel; filter: band-pass 4th order Butterworth: 20-500 Hz; A/D conversor: 12 Bits). Surface electrodes (silver/silver chloride [Ag-AgCl]; 1 cm diameter; 2223 BRQ-3M) were placed on the three muscles according to two

different recommendations. In Protocol 1 [7], electrodes were placed in a pseudo-monopolar montage with one electrode over the muscle's innervation zone and the other over the nearest bony prominence. The muscles' innervation zones were located by means of a specific atlas [8]. Then, this location was confirmed using electrical stimulation (Meridian Energy Acupuncture Pen, Guangzhou Fabulous BYL Beauty Instrument Co., Ltd., China). In Protocol 2, a pair of electrodes were placed on the muscle belly with an interelectrode distance of 1 or 2 cm, depending on the muscle, according to the SENIAM [2]. Figure 1 provides a schematic view of the adopted electrode placement protocols. The reference electrode was placed over the cervical prominence C7. The skin was shaved and cleaned with neutral soap and alcohol before the placement of the electrodes.

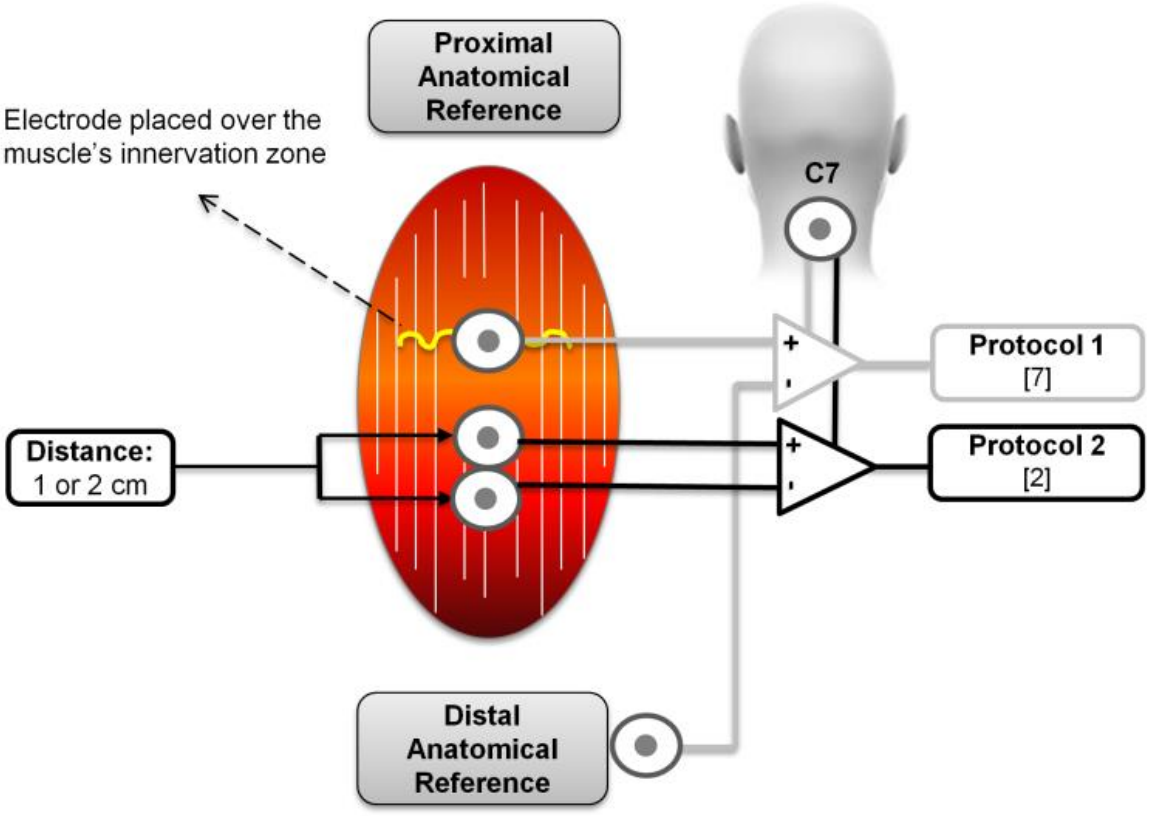

Figure 1. Schematic representation of the electrodes positioning according to the investigated protocols 1 [2] and 2 [7]. The proximal and distal anatomical references, as well as the muscles' innervation zones, were taken as the anatomical landmarks for the placement of the electrodes.

TMS

Shoulder and elbow joints were kept on neutral and flexed (□90o) positions, respectively, and forearms resting on neutral position on a pillow during the whole experimental session. MEPs were recorded from both protocols (1 and 2) simultaneously for each muscle. Between thirty and forty TMS pulses (Magstin 2002, figure-of-eight coil) were applied for 4 minutes to the BB muscle hotspot with an intensity of 120% of the resting motor threshold (rMT) in pseudo-randomized intervals of 5–10 seconds. The BB muscle was chosen as reference since it has the highest motor threshold among the three studied muscles [9,10]. The rMT was defined as the minimum intensity needed to evoke MEPs larger than 100 μV peak-to-peak amplitude [11,12] in at least five out of ten pulses. A cap containing a 1cm2 spaced grid positioned over the participant's skull was used to guide the coil placement during the whole session of recordings. TMS pulses were applied by the same experimenter throughout the sessions. Stimulation on BB muscle hotspot consistently evoked MEPs from the three monitored muscles simultaneously. The participants were vision-deprived during the sEMG recording.

Statistical Analysis

The sEMG signals were processed and analyzed using the Signal Hunter [13] software (MATLAB version 8.1 R2013a, Mathworks Inc., Natick, MA, USA). Peak-to-peak amplitude was extracted from the MEPs. A linear mixed model was applied to assess the effects of protocol type, muscles, limb sides on the natural logarithm of the MEP amplitude. The linear mixed model had a fixed (interaction between protocols, muscles, and limb sides) and a random structure (correlated random intercepts and slopes for protocols and muscles). The random structure was selected based on a sequential testing of hierarchical modelling with each model fit using likelihood ratio tests. The selected model was recomputed using restricted maximum likelihood estimation and p-values estimated using Satterthwaite approximations in a Type III Analysis of Variance. Post-hoc comparisons were performed with estimated marginal means with false discovery rate correction for p-values. The residuals of the model were inspected for deviations from normality and a scale-location plot analyzed to check the assumption of equal variance (homoscedasticity). The analysis was performed in

scripts written in R version 3.6 (R Core Team, Vienna, Austria). The level of significance was set at 0.05.

Results

The MEP amplitude for each protocol, muscle, and limb side is presented in Figure 2. The protocols for electrode placement resulted in different MEP amplitudes depending on the target muscle (protocol × muscle; $F_{2,2213.2} = 5.61$; $P < 0.01$). Overall, Protocol 1 generated higher MEP amplitudes than Protocol 2 (protocol; $F_{1,5.0} = 32.00$; $P < 0.01$). On the FPB muscle, Protocol 1 resulted in MEP amplitudes about 3.8 and 5.3 times higher than in Protocol 2 on the right and left limbs, respectively ($P < 0.01$). For the FCR muscle, Protocol 1 showed MEP amplitudes about 3.6 and 5.6 times higher than in Protocol 2 for the right and left limbs, respectively ($P < 0.05$). Finally, for the BB muscle, Protocol 1 recorded MEP amplitudes 5.1 and 6.1 times higher than Protocol 2 ($P < 0.01$) on the right and left limbs, respectively (Figure 2).

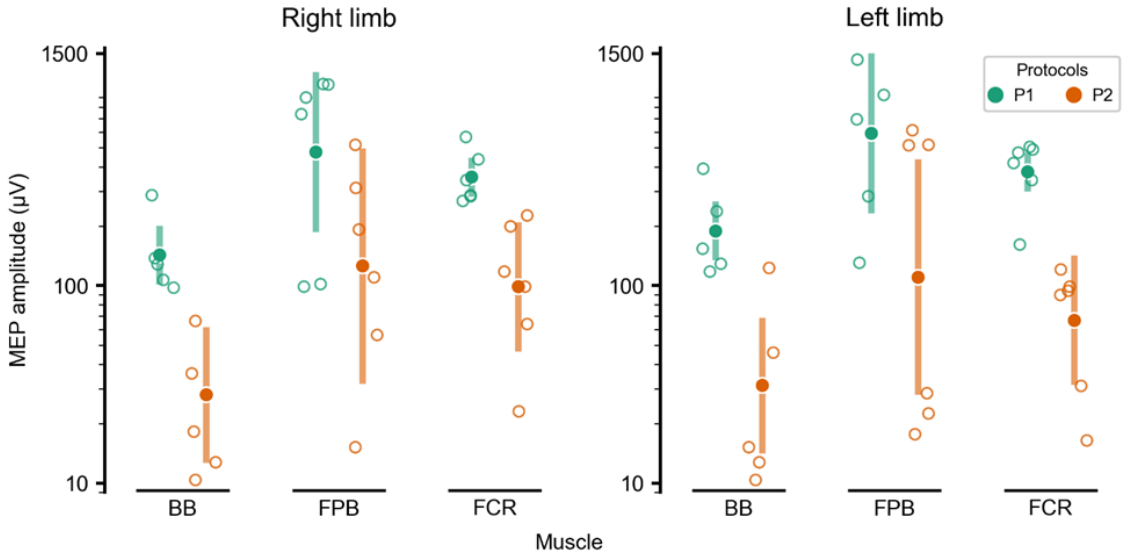

Figure 2. Model predictions and 95% confidence intervals of the MEP amplitudes obtained from the two electrode placement protocols (P1 and P2) in the muscles flexor pollicis brevis (FPB), flexor carpi radialis (FCR), and biceps brachii (BB) on the right and left limbs. The open circles represent the median MEP amplitude for each subject in each condition.

Discussion

The temporal and spectral contents of the sEMG signal strongly depends on the selected protocol of surface electrodes positioning [1,3]. Nonetheless, the standards in electrode placement seem to be disregarded by several TMS studies [14-18]. Therefore, in this study, we evaluated two electrode placement protocols: Protocol 1 as suggested by Garcia et al. [7] and Protocol 2 following the SENIAM recommendations [2]. Our results strongly suggested that the MEP amplitude depends on the electrode placement protocol, which may have a direct impact on comparisons across studies and on TMS treatment outcomes.

Protocol 1 resulted in 3.5 to 6.1 times higher MEP amplitudes compared to Protocol 2 for the three muscles investigated, which is most likely explained by the distinct operating principles of each protocol. Protocol 1 records the MEP in a monopolar configuration over the neuromuscular junctions and would result in a higher probability of action potentials coherent summation when reaching the muscle fibers [7]. The coherent summation leads to MEPs with greater amplitude. It is interesting to note that the adoption of this type of protocol was recently advocated by Stålberg et al. [19] in neurography evaluations, i.e., when peripheral electrical nervous stimuli are applied. According to the authors, the placement of an electrode on the neuromuscular junction offered more robust estimates of the latency, which would also be another advantage for this type of protocol in TMS applications. On the other hand, Protocol 2 was designed to reduce the level of crosstalk during signal acquisition using inter-electrode distances between 1-2 cm, depending on the muscle. The crosstalk from neighbor muscles contaminates the MEPs recorded in the forearm with conventional EMG montages [24,25]. In this case, the use of high-density sEMG might provide additional insights for the electrode placement based on the MEP spatial distribution over the entire muscle extent [26]. Even so, the relatively small distance between electrodes in Protocol 2 may offer a reduced volume conductor when recording MEPs even from small muscle, such as the FPB, reducing the total evoked myoelectric activity when compared to Protocol 1.

The MEP amplitude is routinely adopted as a parameter to evaluate the integrity of the corticospinal pathway and in the interpretation of the process of integration and processing of cortical and subcortical areas in healthy and pathological subjects [10,20]. Thus, the application of different protocols for the

electrode placement in studies whose questions are similar could result in diverging outcomes, making it difficult to establish comparisons [21]. In addition, we should point out that the intensity of repetitive TMS (rTMS) is mainly defined relative to the MEP amplitude, and distinct electrode placement protocols may partially explain the divergences found in the literature regarding the efficacy of rTMS in the treatment of patients with similar diagnoses [22, 23], which is probably due to inappropriate dose delivery during the treatment.

We should note that the resting motor threshold in our study was adjusted to obtain 100 µV MEPs which is commonly used in multiple TMS studies [11,12]. However, distinct adjustment of stimulation intensities may provide a different dependency of the MEP amplitude on the electrode placement.

Finally, our study was performed in a limited number of subjects and assessed only two electrode placement protocols. Nonetheless, the observed differences provide first evidence that distinct protocols lead to large differences in MEP amplitude, and electrode placement should be carefully considered in brain stimulation studies and clinical applications.

Conclusion

Our study fosters the scientific community for the need of a standardized electrode placement on experiments recording MEPs, which seems to be significantly affected by the adopted protocol.

References

[1] Lynn PA, Bettles ND, Hughes AD and Johnson SW 1978 Influence of electrode geometry on bipolar recordings of the surface electromyogram Med Biol Eng Comput. 16 651-60

[2] Hermens HJ, Freriks B, Disselhorst-Klug C and Rau G 2000 Development of recommendations for SEMG sensors and sensor placement procedures J Electromyogr Kinesiol. 10 361-74

[3] Garcia MAC and Vieira TMM 2011 Surface electromyography: Why, when and how to use it Rev Andal Med Deport. 4 17-28

[4] Groppa S, Oliviero A, Eisen A, Quartarone A, Cohen LG, Mall V, Kaelin-Lang A, Mima T, Rossi S, Thickbroom GW, Rossini PM, Ziemann U, Valls-Solé and Siebner HR 2012 A pratical guide to diagnostic transcranial magnetic stimulation: Report of an IFCN committee J Clin Neurophysiol. 123 858-82

[5] Legatt AD, Emerson RG, Epstein CM, MacDonald DB, Deletis V, Bravo RJ and López JR 2016 ACNS guideline: Transcranial electrical stimulation motor evoked potential monitoring J Clin Neurophysiol. 33 42-50

[6] Tankisi H, Burke D, Cui L, de Carvalho M, Kuwabara S, Nandedkar SD, Rutkove S, Stålberg E, van Putten MJAM and Fuglsang-Frederiksen 2020 Standards of instrumentation of EMG J Clin Neurophysiol. 131 243-58

[7] Garcia MAC, Souza VH and Vargas CD 2017 Can the recording of motor potentials evoked by transcranial magnetic stimulation be optimized? Front Hum Neurosci. 11 413

[8] Barbero M, Merletti R and Rainoldi A 2012 Atlas of Muscle Innervation Zones (Milan: Springer-Verlag)

[9] Vargas CD, Aballéa A, Rodrigues EC, Reilly KT, Mercier C, Petruzzo P, Dubernanrd JM and Sirigu A 2009 Re-emergence of hand-muscle representations in human motor cortex after hand allograft Proc Natl Acad Sci U S A. 106 7197-202

[10] Garcia MAC, Catunda JMY, Souza MN, Fontana AP, Sperandei S and Vargas CD 2016 Is the frequency in somatosensory electrical stimulation the key parameter in modulating the corticospinal excitability of healthy volunteers and stroke patients with spasticity? Neural Plast. 2016 3034963

[11] Nogueira-Campos AA, de Oliveira LAS, Della-Maggiore V, Esteves PO, Rodrigues EC and Vargas CD 2014 Corticospinal excitability preceding the grasping of emotion-laden stimuli PLoS One. 9 e94824

[12] Borgomaneri S, Vitale F, Gazzola V and Avenanti A 2015 Seeing feaful body language rapidly freezes the observer's motor cortex Cortex. 65 232-45

[13] Souza VH, Peres A, Zacharias L and Baffa O 2015 SignalHunter: Software for electrophysiological data analysis and visualization (Version v1.0.0) https://doi.org/10.5281/zenodo.1326307

[13] Golaszewski S, Schwenker K, Bergmann J, Brigo F, Christova, M, Trinka E and Nardone R 2016 Abnormal short-latency synaptic plasticity in the motor cortex of subjects with Becker muscular dystrophy: A rTMS study Neurosci Lett. 610 218-22

[15] Pedapati EV, Gilbert DL, Erickson CA, Horn PS, Shaffer RC, Wink LK, Laue CS and Wu SW 2016 Abnormal Cortical Plasticity in Youth with Autism Spectrum Disorder: A Transcranial Magnetic Stimulation Case-Control Pilot Study J Child Adolesc Psychopharmacol. 26 625-31

[16] Tang Z-, Xuan C-, Li X, Dou Z-, Lan Y- and Wen H- 2019 Effect of different pulse numbers of transcranial magnetic stimulation on motor cortex excitability: Single-blind, randomized cross-over design CNS Neurosci Ther. 25 1277-81

[17] Hannah R, Rocchi L, Tremblay S, Wilson E and Rothwell JC 2020 Pulse width biases the balance of excitation and inhibition recruited by transcranial stimulation Brain Stimul. 13 536-8

[18] Muellbacher W, Ziemann U, Boroojerdi B, Cohen L and Halltett M 2001 Role of the human motor cortex in rapid motor learning Exp Brain Res. 136 431-8

[19] Stålberg E, van Dijk H, Falk B, Kimura J, Neuwirth C, Pitt M, Podnar S, Rubin DI, Rutkove S, Sanders DB, Sonoo M, Tankisi H and Zwarts M 2019 Standards for quantification of EMG and neurography J Clin Neurophysiol. 130 1688-1729

[20] Peres ASC, Souza VH, Catunda JMY, Mazzetto-Betti KC, Santos-Pontelli TEG, Vargas CD, Baffa O, Araújo DB de, Pontes Neto OM, Leite JP and Garcia MAC 2018 Can somatosensory electrical stimulation relieve spasticity in post-stroke patients ? A TMS pilot study Biomed Tech (Berl). 63 501-6

[21] Catroflorio T, Farina D, Bottin A, Piancino MG, Bracco P and Merletti R 2005 Surface EMG of jaw elevator muscles: effect of electrode location and inter-electrode distance J Oral Rehabil. 32 411-7

[22] Rollnik JD, Huber TJ, Mogk H, Siggelkow S, Kropp S, Dengler R, Emrich HM and Schneider U 2000 High frequency repetitive magnetic stimulation (rTMS) of the dorsolateral prefontral cortex in schizophrenic patients Neuroreport. 11 4013-15

[23] Saba G, Verdon CM, Kalalou K, Rocamora JF, Dumontier G, Benadhira R, Stamatiadis L, Vicaut E, Lipski H, Januel D 2006 Transcranial magnetic stimulation in the treatment of schizophrenic symptoms: A double blind sham controlled study J Psychiatr Res. 40 147-52

[24] Neva JL, Gallina A, Peters S, Garland SJ and Boyd LA 2017 Differentiation of motor evoked potentials elicited from multiple forearm muscles: An investigation with high-density surface electromyography Brain Res. 1676 91-9

[25] Gallina A, Peters S, Jason L. Neva JL, Boyd LA and Garland SJ 2017 Selectivity of conventional electrodes for recording motor evoked potentials: An investigation with high-density surface electromyography Muscle Nerve. 55 828-34

[26] Souza VH, Vieira TM, Peres ASC, Garcia MAC, Vargas CD and Baffa O 2018 Effect of TMS coil orientation on the spatial distribution of motor evoked potentials in an intrinsic hand muscle Biomed Tech (Berl). 63 635-45

APPENDIX C – ESTIMULAÇÃO MAGNÉTICA TRANSCRANIANA: UMA BREVE REVISÃO DOS PRINCÍPIOS E APLICAÇÕES

This article is published at the journal Revista Brasileira de Física Médica (DOI: 10.29384/rbfm.2019.v13.n1.p49-56). The reuse of this article in my thesis is in compliance with journal Copyright policy.

Title: Estimulação magnética transcraniana: uma breve revisão dos princípios e aplicações

Authors: Renan H. Matsuda[1], Gabriela P. Tardelli[1], Carlos O. Guimarães[1], Victor Hugo Souza[2], Oswaldo Baffa[1]

[1]Laboratório de Biomagnetismo, Departamento de Física da Faculdade de Filosofia Ciências e Letras da Universidade de São Paulo (USP), Ribeirão Preto (SP), Brasil

[2]Department of Neuroscience and Biomedical Engineering, Aalto University School of Science (AALTO), Espoo, Finland

Resumo

A estimulação magnética transcraniana é um método não invasivo de estimulação do córtex humano. Conhecida pela sigla TMS, a técnica foi introduzida por Barker et al. em 1985. Seu funcionamento baseia-se na Lei de Faraday, no qual um intenso campo magnético que varia rapidamente é capaz de induzir um campo elétrico na superfície do cérebro, despolarizando os neurônios no córtex cerebral. Devido a sua versatilidade, a TMS é utilizada atualmente tanto no âmbito da pesquisa quanto em aplicações clínicas. Dentre as aplicações clínicas a TMS é utilizada como uma ferramenta diagnóstica e também como uma técnica terapêutica de algumas doenças neurodegenerativas e distúrbios psiquiátricos como a depressão, a doença de Parkinson e o tinnitus. Quanto a ferramenta diagnóstica, destaca-se o mapeamento motor, uma técnica de delimitação da área de representação do músculo alvo em sua superfície cortical, cuja aplicabilidade pode ser em estudos da fisiologia cerebral para avaliar danos ao córtex motor e trato corticoespinhal. Essa revisão tem como

objetivo introduzir a física, os elementos básicos, os princípios biológicos e as principais aplicações da estimulação magnética transcraniana.

Palavras-chave: estimulação magnética transcraniana; biomagnetismo; neuroestimulação; neuronavegação.

Abstract

Transcranial magnetic stimulation is a noninvasive method of stimulation of the human cortex. Known by the acronym TMS, the technique was introduced by Barker et al. in 1985. Its operation is based on Faraday's Law, in which an intense magnetic field that varies rapidly is able to induce an electric field in the surface of the brain, depolarizing the neurons in the cerebral cortex. Because of its versatility, TMS is currently used for both research and clinical applications. Among the clinical applications, TMS is used as a diagnostic tool and also as a therapeutic technique for some neurodegenerative diseases and psychiatric disorders such as depression, Parkinson's disease and tinnitus. As for the diagnostic tool, the motor mapping is a technique to delineate the area of representation of the target muscle in its cortical surface, whose applicability may be in studies of the cerebral physiology to evaluate damage to the motor cortex and corticospinal tract. This review aims to introduce physics, the basic elements, the biological principles and the main applications of transcranial magnetic stimulation.

Keywords*: transcranial magnetic stimulation; biomagnetism; neurostimulation; neuronavigation.*

Introdução

A estimulação magnética transcraniana (TMS, do inglês *transcranial magnetic stimulation*) foi introduzido em 1985 por Barker et al. como um método não invasivo de estimulação do córtex humano (BARKER; JALINOUS; FREESTON, 1985). O experimento de Barker et al. evidenciou o efeito da aplicação de um pulso simples de TMS sobre o córtex motor primário. Uma corrente elétrica da ordem de kA é aplicada em uma bobina posicionada externamente sobre o escalpo. A rápida variação da corrente elétrica gera um pulso magnético da ordem de centenas de microsegundos de duração, que por sua vez induz campos elétricos no tecido cerebral. O campo elétrico induzido é capaz de

despolarizar os neurônios no córtex cerebral e gerar potenciais de ação. No caso do córtex motor primário, parte dos potenciais de ação resultantes percorrem o trato corticoespinhal atingindo os neurônios motores espinhais e, finalmente, um músculo alvo. Após a neuroestimulação, Barker et al. observou uma rápida contração dos músculos da mão. As contrações musculares podem ser mensuradas através dos sinais elétricos adquiridos por um eletromiógrafo de eletrodo de superfície. Essa atividade mioelétrica produzida em resposta à TMS é denominada potencial evocado motor (PEM ou MEP, do inglês *motor evoked potential*) (GARCIA; SOUZA; VARGAS, 2017; ROSSINI; ROSSI, 1998b; WASSERMANN *et al.*, 1992a).

Atualmente a TMS é uma ferramenta consolidada para estimulação não-invasiva do cérebro. A técnica é utilizada tanto por neurocientistas no âmbito da pesquisa quanto por médicos e fisioterapeutas em aplicações clínicas. Devido à sua versatilidade de aplicações, a TMS é usada para diagnóstico e também para terapia. Dentre as aplicações diagnósticas, cabe destacar a avaliação da integridade funcional das vias motoras corticoespinais (PERES *et al.*, 2018). Avaliando então possíveis danos, lesões e outros transtornos neurológicos (GROPPA *et al.*, 2012a).

A aplicação de pulsos repetitivos de TMS no córtex pode atuar de maneira excitatória ou de forma inibitória, dependendo da frequência com que os pulsos são aplicados. Resultando assim na reativação de regiões de pouca atividade ou na redução da atividade metabólica de regiões muito ativas (FITZGERALD; FOUNTAIN; DASKALAKIS, 2006). A partir desse princípio, a TMS é usada para auxiliar o tratamento de algumas doenças neurodegenerativas e distúrbios psiquiátricos, como a depressão, a doença de Parkinson e o tinnitus (ROSSINI *et al.*, 2015).

O objetivo dessa revisão é introduzir de forma sucinta a física da estimulação magnética transcraniana e também apresentar suas principais aplicações como o mapeamento motor e a TMS repetitiva na terapia de algumas neuropatologias.

Princípio físico

O equipamento de TMS é composto por uma bobina, isto é, um enrolamento de fios de cobre que definem um indutor, conectado a um circuito

elétrico com capacitores e resistores em série. Apesar de receber o nome de ‘’estimulação magnética’’, à nível neuronal é o campo elétrico que excita regiões do cérebro.

Os capacitores, inicialmente carregados, são descarregados fazendo fluir uma corrente através da bobina. De acordo com a Lei de Ampére-Maxwell, descrita pela equação (1), essa corrente induz um campo magnético que varia rapidamente no tempo.

$$\nabla x\vec{B} = \mu_0 \vec{J} + \mu_0 \varepsilon_0 \frac{\partial \vec{E}}{\partial t} \qquad (1)$$

onde $\vec{B}$ é o campo magnético, $\vec{E}$ o campo elétrico, $\vec{J}$ a densidade de corrente, μ_0 a permeabilidade magnética no vácuo e ε_0 a permissividade elétrica no vácuo.

Como tecidos biológicos possuem permeabilidade magnética aproximadamente igual à do vácuo, o campo magnético penetra pelo escalpo e pelo crânio sem sofrer uma atenuação significativa. Ao alcançar a superfície cortical condutora este campo magnético variante induz um campo elétrico primário descrito pela Lei de Faraday – equação (2). Dessa forma, as partículas carregadas no tecido cerebral são a um intenso campo elétrico, que induz um fluxo de densidade de corrente, descrito pela equação (3), capaz de despolarizar os neurônios na região em questão.

$$\nabla x\vec{E} = -\frac{\partial \vec{B}}{\partial t} \qquad (2)$$

$$\vec{J} = \sigma \vec{E} \qquad (3)$$

onde $\vec{B}$ é o campo magnético, $\vec{E}$ o campo elétrico, $\vec{J}$ a densidade de corrente e σ a condutividade do tecido.

Ao posicionar a bobina tangencialmente à superfície da cabeça do sujeito, o campo magnético gerado encontra-se perpendicular à bobina e consequentemente o campo elétrico induzido é perpendicular ao campo magnético, sendo assim antiparalelo à corrente da bobina (figura 1). O campo

magnético possui entre 1 e 2,5 T de intensidade (GROPPA *et al.*, 2012b) chegando a penetrar de 2 a 4 cm do escalpo. O campo elétrico necessário para provocar um PEM é de aproximadamente 70 V/m (RUOHONEN, 2005). Tais magnitudes dependem de uma série de fatores, como o tipo de bobina, a forma de onda da corrente elétrica e do tipo de pulso magnético (PETERCHEV *et al.*, 2013).

Figura 1 - Representação da corrente em uma bobina circular sobre o escalpo, das linhas de campo magnético e campo elétrico induzido.

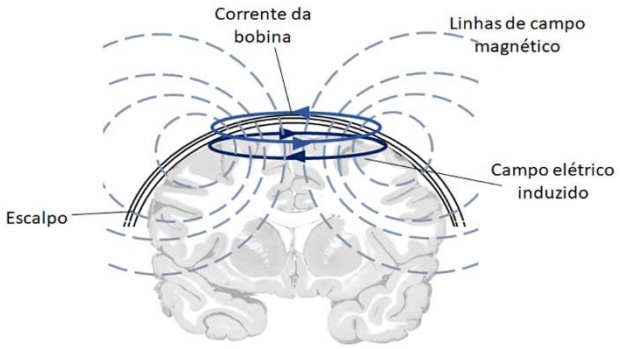

Fonte: Os autores (2019)

Princípio biológico

Na membrana da célula nervosa há uma diferença de potencial elétrico gerado por íons negativos dissociados no meio interno da célula e íons positivos no meio externo, chamado de potencial de repouso. Quando um campo elétrico é induzido em uma célula nervosa uma alteração do potencial de repouso da célula é provocada, a qual terá sua polaridade invertida. Dessa forma, o interior da célula ficará eletricamente positivo e o exterior negativo por algumas dezenas de microssegundos, retomando seu potencial de repouso rapidamente (figura 2). Este processo de despolarização e repolarização envolve correntes elétricas que podem provocar um potencial de ação que se propagará ao longo da célula nervosa. Além do potencial excitatório gerado pela despolarização dos neurônios, existe um processo contrário na qual o potencial tem função inibitória, chamado de hiperpolarização.

Figura 2 - Representação do campo elétrico sobre neurônios piramidais; A parte ampliada representa um axônio sofrendo despolarização.

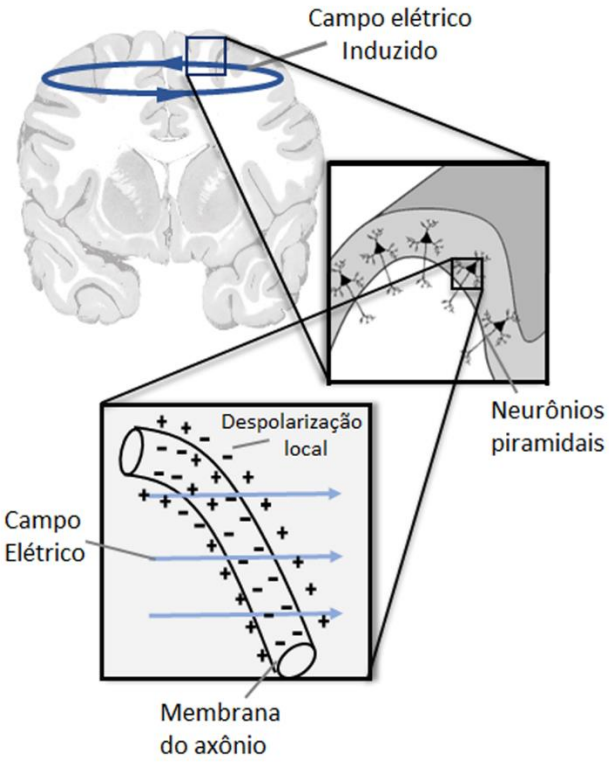

Fonte: Adaptado de Ruohonen e Ilmoniemi (2005) (RUOHONEN, 2005).

A TMS, quando aplicada no córtex motor, induz potenciais de ação em neurônios piramidais, que se propagam para áreas subcorticais e são projetados no trato corticospinhal atingindo neurônios motores e, por último o musculo alvo. A atividade mioelétrica é adquirida e monitorada por eletromiografia de superfície (figura 3) (ROSSINI; ROSSI, 1998a; WASSERMANN *et al.*, 1992b), sendo a amplitude e latência dos PEM os principais parâmetros extraídos.

Figura 3 - Esquema da aplicação da TMS sobre o córtex motor. O potencial de ação propaga pelo trato corticospinhal até o músculo alvo,

produzido o MEP.

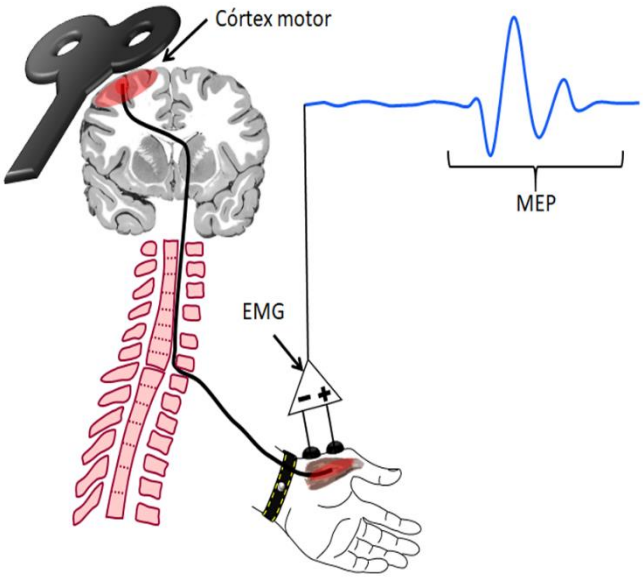

Fonte: Os autores (2019)

Equipamento de estimulação

É de grande importância o conhecimento de propriedades que influenciam a TMS a fim de determinar quais os objetivos de cada técnica e quais as melhores condições para alcançá-lo. Dentre essas especificidades encontram-se a geometria da bobina, bem como sua localização, a sequência de pulsos aplicados, o formato da onda desse pulso, a corrente aplicada e as propriedades dos tecidos estimulados.

Configurações do estimulador

O circuito básico de um estimulador magnético é composto por um capacitor, uma bobina e uma chave de estado sólido. Um pulso de TMS inicia-se com o capacitor totalmente carregado. Assim que a chave de estado sólido fecha o circuito, o capacitor descarrega uma corrente elétrica diretamente na bobina. Dessa forma, quando a corrente é zero, a energia está no capacitor; quando a corrente é máxima, a energia está na bobina(WASSERMANN; ZIMMERMANN, 2012b).

Durante um pulso monofásico, após a corrente na bobina atingir seu valor máximo, a energia do circuito começa a ser dissipada lentamente, como mostra a figura 4. Em um pulso bifásico, ao invés de ser dissipada a energia é

recuperada de forma a gerar uma segunda corrente no sentido contrário que recarregará o capacitor (MATTHÄUS; SCHWEIKARD, 2008), e a forma da onda terá o comportamento de um seno amortecido (figura 4). A reutilização da energia faz com que o pulso bifásico seja útil em aplicações de intervalo de tempo curtos como em uma estimulação repetitiva, e o pulso monofásico em uma estimulação de pulso único (EPSTEIN; WASSERMANN; ZIEMANN, 2012).

Figura 4 - Representação da forma de onda de um pulso bifásico acima, e de um pulso monofásico abaixo. A curva vermelha representa tanto a tensão na bobina quanto a tensão induzida no cérebro e a curva em azul representa a corrente que passa pela bobina.

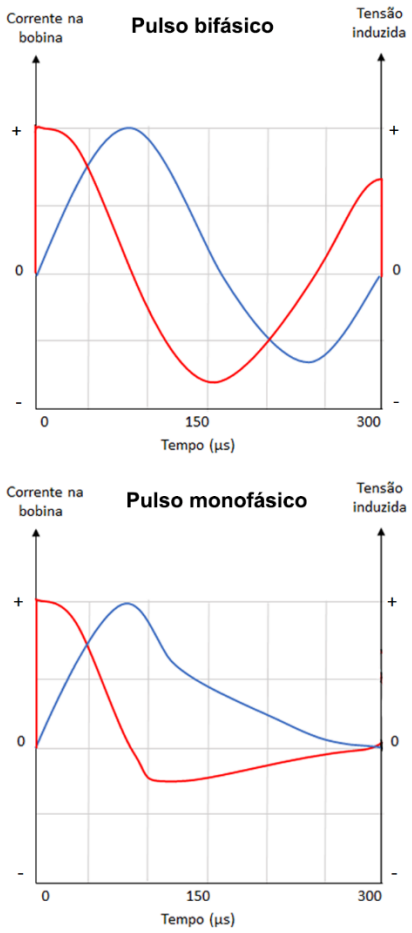

Fonte: Adaptado de Epstein et al. (2012)[16]

O intervalo de tempo de aplicação de pulsos é um dos fatores a ser considerado em uma técnica de TMS. A estimulação de pulso simples é realizada através de um único estímulo sobre a região de interesse, os estímulos

podem ser repetidos de acordo com o experimentador, sendo este método útil em experimentos de estudo do sistema motor (WASSERMANN; ZIMMERMANN, 2012b). A estimulação de pulsos pareados (pTMS) consiste em dois pulsos sucessivos através da mesma bobina em um curto intervalo de tempo de alguns milissegundos. Esta técnica é utilizada a fim de explorar redes intracorticais inibitórias ou excitatórias, cuja resposta vai depender, dentre outros fatores, do intervalo entre os pulsos (SOUZA; BAFFA; GARCIA, 2018).

Um terceiro método é a TMS repetitiva (rTMS), que é definido por uma sequência de pulsos aplicados em uma determinada frequência, na qual é possível alterar e modular a atividade cortical. Os efeitos modulatórios da rTMS são controversos, mas há indícios de que aplicações em frequências abaixo de 1 Hz podem diminuir a excitabilidade cortical, enquanto pulsos aplicados em frequências mais altas, acima de 5 Hz, podem aumentar a excitabilidade cortical (MULLER *et al.*, 2013). Dessa forma, a rTMS tem sido amplamente utilizada no tratamento de distúrbios neurológicos (KLOMJAI; KATZ; LACKMY-VALLÉE, 2015a). Uma modalidade variante da rTMS é o procedimento de estimulação Theta Burst (TBS, do inglês *theta burst stimulation*) na qual são aplicados pacotes de pulsos com 50 Hz de frequência a cada 200 ms (5 Hz) (BENALI *et al.*, 2011; OBERMAN, LINDSAY; PASCUAL-LEONE, 2011). A TBS possui efeitos semelhantes à rTMS na excitabilidade cortical, mas tem mostrado ser mais eficaz com efeito mais duradouro em menor tempo da sessão.

Configurações de bobina

Estudos de EMT iniciaram-se com a bobina em formato circular (figura 5). Nesta configuração, a corrente que percorre a bobina induz uma corrente no sentido antiparalelo no cérebro e o campo magnético é máximo abaixo do centro da bobina (EPSTEIN; WASSERMANN; ZIEMANN, 2012). No entanto, a especificidade deste estímulo é pequena, uma vez que o campo elétrico é induzido seguindo a circunferência da bobina. A bobina circular é mais utilizada em aplicações clínicas em que se deseja estimular uma ampla região do cérebro.

Bobinas em formato de 8, ou *butterfly*, são constituídas por dois enrolamentos posicionados lado a lado, na qual o campo elétrico é máximo no

ponto de encontro entre eles e a estimulação é mais focal na região abaixo da junção (EPSTEIN; WASSERMANN; ZIEMANN, 2012; PERES *et al.*, 2009).

Figura 5 - Representação do campo elétrico induzido pela bobina circular, em cima, e pela bobina figura 8, em baixo.

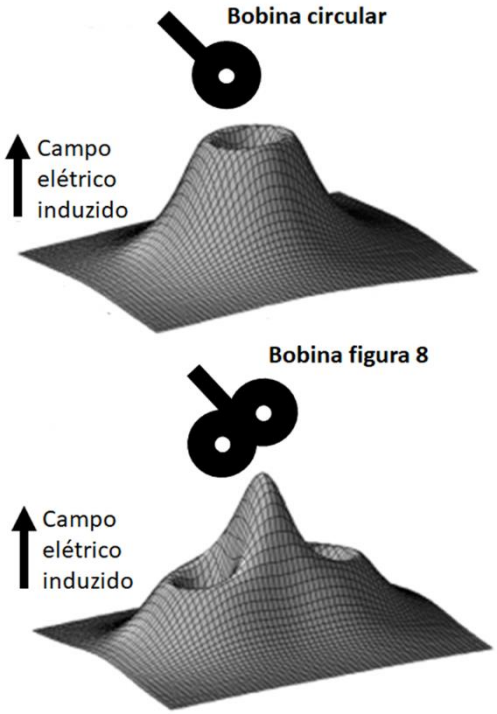

Fonte: Adaptado de Ruohonen e Ilmoniemi (2005) (BRASIL-NETO *et al.*, 1992b; SOUZA *et al.*, 2018b).

Bobinas em formato de cone duplo assemelham-se à figura 5, porém os anéis são montados em um ângulo entre 90 a 100 graus. Isso fornece a capacidade de estimular uma porção maior e assim atingir estruturas relativamente mais profundas, possibilitando, por exemplo, estimulações mais eficientes dos membros inferiores (ARAÚJO *et al.*, 2011). Contudo, está bobina não é focal e um único pulso pode provocar respostas bilaterais (KLOMJAI; KATZ; LACKMY-VALLÉE, 2015b). É importante notar que, estimulações mais profundas com TMS são sempre seguidas da estimulação com intensidade consideravelmente maior das camadas superficiais do cérebro. Portanto, perde-se em termos de focalização, estimulando também camadas preliminares referentes a membros inferiores e contrações faciais.

Além do formato, outros parâmetros importantes a serem considerados é a posição da bobina e sua orientação em relação as regiões do cérebro. A bobina é posicionada sobre o escalpo acima da região de interesse para estimulação. Estudos sugerem que campos elétricos induzidos paralelamente às estruturas do córtex motor ativam maior número de elementos neurais e, portanto, a amplitude do potencial evocado é maior. Por exemplo, a orientação ótima para estimular os músculos intrínsecos da mão é com alinhamento do campo elétrico resultante aproximadamente perpendicular ao sulco central, isto é, entre 45° e 90° em relação ao plano sagital, ao contrário, de ângulos de 135° e 315°MENDELEY CITATION PLACEHOLDER 23.

Estimulação magnética transcraniana navegada

A neuronavegação é uma técnica de visualização computacional em tempo real cujo objetivo é auxiliar o posicionamento de instrumentos cirúrgicos em relação às estruturas neuronais (SOUZA *et al.*, 2018a). Os instrumentos e a morfologia cerebral são representados por modelos tridimensionais, criados a partir de imagens de tomografia computadorizada ou de ressonância magnética. As posições dos instrumentos são monitoradas em tempo real por equipamentos de rastreamento espacial e visualizadas em uma interface gráfica computacional. Sendo assim, é possível verificar a posição da bobina de estimulação em relação às estruturas neuronais durante a aplicação do TMS.

A TMS guiada por neuronavegação é chamada de estimulação magnética transcraniana navegada (nTMS). A nTMS permite considerar as diferenças anatômicas entre os indivíduos para posicionamento da bobina sobre o sítio investigado. Além da localização da bobina, a neuronavegação também permite ajustar a orientação ótima e a inclinação do campo de estimulação em relação ao escalpo.

Tradicionalmente, o posicionamento da bobina de TMS utiliza como referência o protocolo de posicionamento de eletrodos de EEG (sistema 10-20) para estimular as regiões alvo. O estudo de Julkunen et al., 2009, comparou a TMS aplicada da maneira tradicional e navegada. Foi mostrado que, utilizando a neuronavegação, os limiares motores atingidos são mais estáveis, permitindo. uma estimulação mais precisa e reprodutível (JULKUNEN *et al.*, 2009). Mesmo

com auxílio de mapas durante o processo de TMS não navegado, variações na orientação e rotação da bobina podem acabar estimulando uma área diferente da área de interesse. Tal problema é contornado pela neuronavegação, que permite definir e acompanhar o local e a orientação ideal de estimulação.

Atualmente existem dois princípios de neuronavegação para TMS: a navegação por projeção linear e a navegação pelo campo elétrico. O método de navegação por projeção linear se baseia na projeção de um vetor normal do centro da bobina de estimulação até superfície do córtex. Logo, o ponto de estímulo é determinado pela intersecção do vetor normal com a superfície do cérebro (SOLLMANN *et al.*, 2016). Porém, a região que realmente é estimulada pela TMS é dada pelo campo elétrico induzido no córtex. O campo elétrico pode variar pela geometria, condutividade do meio e da intensidade do campo magnético aplicado. Por isso, o método de navegação pelo campo elétrico leva em consideração informações anatômicas e físicas do meio. Por exemplo, a espessura do crânio, a distância entre a bobina e cérebro, a condutividade elétrica e a geometria do cérebro. Para então, a partir da posição da bobina e da intensidade do campo magnético aplicado da TMS, simular em tempo real o campo elétrico induzido na superfície do córtex.

Principais aplicações

Mapeamento motor

O mapeamento motor é uma técnica de delimitação da área de representação do músculo alvo em sua superfície cortical (ROMERO *et al.*, 2011; WASSERMANN *et al.*, 1992b). Essa técnica é utilizada em estudos da fisiologia cerebral (ROSSINI *et al.*, 2015) para avaliar danos ao córtex motor e trato corticoespinhal (ROSSINI *et al.*, 2015; ZIEMANN, 2000), e para avaliação da representação funcional do músculo no cérebro (ETTINGER *et al.*, 1998).

O procedimento de mapeamento é dado pela amplitude do MEP e o sítio de aplicação do pulso de TMS, que juntos definem a região sobre o escalpo para obtenção de resposta do músculo desejado. Os parâmetros mais importantes do mapa motor é o *hotspot* e o limiar motor de repouso. O *hotspot* é o sítio cortical abaixo do centro da bobina que resulta em um MEP com máxima amplitude para um pulso simples de TMS (SÄISÄNEN *et al.*, 2008; WASSERMANN *et al.*, 1992b). O limiar motor de repouso é definido como a menor intensidade de

estímulo capaz de evocar potenciais maiores que uma determinada amplitude (CONFORTO *et al.*, 2004).

Figura 6 - Mapeamento motor do músculo flexor curto do polegar. Os pontos vermelhos são os locais de estímulos. As linhas verdes são as projeções do local de estímulo até o córtex. Note que as projeções são mostradas para efeito de visualização, e não representam o local de estimulação do córtex. A escala de cor está normalizada sendo 1 a maior amplitude do MEP encontrado e zero nenhuma resposta obtida.

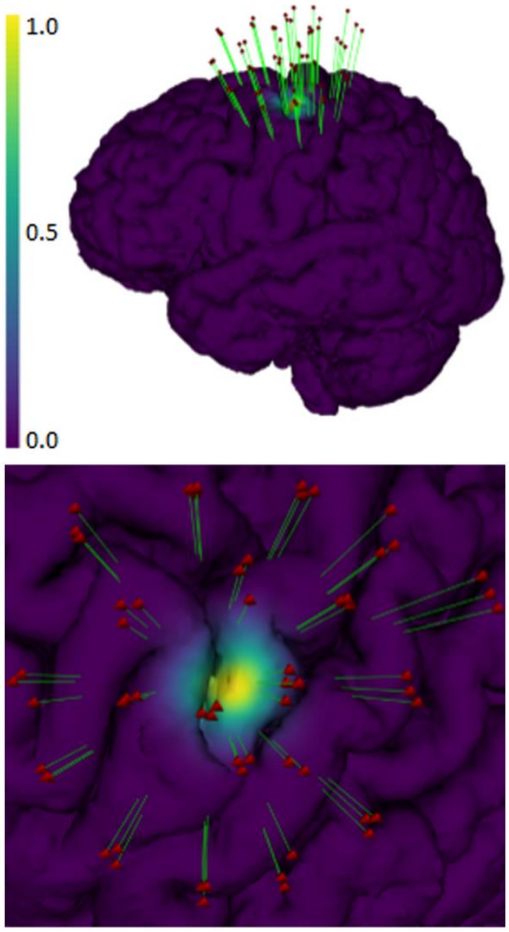

Fonte: Os autores (2019)

A localização do *hotspot* e o limiar motor estão relacionados com a representação do músculo no córtex motor. A busca pelo *hotspot* pode ser realizada com o auxílio de um sistema de neuronavegação, ou com base em referências anatômicas (BOROOJERDI *et al.*, 1999b). Na ausência dos sistemas

de neuronavegação, a busca pelo *hotspot* é um procedimento demorado e requer experiência prévia do operador, estando assim, sujeito à grande variabilidade.

A figura 6 apresenta um exemplo de mapeamento motor por TMS do músculo flexor curto do polegar. As avaliações da representação cortical do músculo podem ser quantificadas por meio de grandezas do mapa motor, como a área, volume e o centroide (JULKUNEN, 2014).

rTMS como terapia

A rTMS é amplamente utilizada no âmbito terapêutico, de acordo com a frequência da sequência de pulsos. Aplicações de rTMS no córtex podem atuar de maneira excitatória reativando regiões de pouca atividade ou de forma inibitória reduzindo regiões muito ativas. Dentre algumas doenças na qual o tratamento com rTMS é utilizada encontram-se acidente vascular cerebral (AVC), dor crônica, depressão, transtorno bipolar, transtorno obsessivo compulsivo, tinnitus, esquizofrenia e doenças neurodegenerativas como doença de Parkinson e Alzheimer.

Depressão

A depressão é uma doença na qual os dois hemisférios do cérebro estão em desequilíbrio: o lado direito fica mais ativo, enquanto o esquerdo fica inibido, ou seja, com menor atividade metabólica.

A primeira aplicação terapêutica da rTMS no tratamento da depressão foi realizada por 36 em uma sessão de pulsos a 20Hz de frequência, a fim de excitar o córtex pré-frontal dorsolateral esquerdo (DLPFC)(WASSERMANN; ZIMMERMANN, 2012b) e aumentar a estabilidade do hemisfério esquerdo, restabelecendo o equilíbrio entre eles.

A rTMS apresenta resultados diferentes de acordo com o tratamento. Se a estimulação é combinada a fármacos, é necessário adequar a frequência, o número de sessões e a intensidade dos pulsos. Além disso, o posicionamento da bobina é fundamental no tratamento, que pode ser realizada com equipamentos de neuronavegação (FORSTER *et al.*, 2014; SOUZA *et al.*, 2018a).

Doenças neurodegenerativas – Doença de Parkinson

A doença de Parkinson é uma doença degenerativa, crônica e progressiva que se desenvolve quando os neurônios da substância negra, pequena área do cérebro, começam a morrer. Esses neurônios são responsáveis pela produção de dopamina, um neurotransmissor que comunica áreas cerebrais responsáveis pelos movimentos (LEENTJENS, 2004).

A degeneração desses neurônios indica diminuição da atividade metabólica nesta região. Métodos de tratamento cirúrgicos ou através de fármacos ainda são limitados, dessa maneira a rTMS mostra-se uma nova modalidade a ser considerada uma vez que direcionar pulsos de rTMS no córtex motor pode estimular a secreção de dopamina e levar a resultados positivos quanto ao tratamento (HELMICH *et al.*, 2006).

A diversidade de resultados obtidos por estimulação em pacientes com doença de Parkinson, dificulta a seleção de uma melhor área e frequência (ARAÚJO *et al.*, 2011). Estudos mostram que a estimulação do córtex motor primário com frequência entre 0,5 e 25Hz por uma bobina em formato de oito fornecem melhorias na escala de avaliação da doença, na fala, redução da rigidez e bradicinesia contralateral.

Esquizofrenia e tinnitus

A aplicação de rTMS com baixa frequência (menor ou igual a 1Hz) é utilizada como terapia para o tinnitus que se caracteriza como zumbido no ouvido. Ele pode ser fraco e não causar incômodos, mas em alguns casos pode afetar o dia a dia do paciente. O zumbido está associado à atividade metabólica no córtex auditivo primário esquerdo, o que requer tratamento de efeitos inibitórios das células excitadas a fim de reduzir, no paciente, a percepção do zumbido (LEFAUCHEUR *et al.*, 2012b).

Além do zumbido, estudos mostram que alucinações auditivas esquizofrênicas também são causadas por ativação de regiões do córtex temporoparietal, e dessa maneira, a rTMS de baixa frequência no tratamento da esquizofrenia age de maneira a reduzir a atividade nessa área do cérebro e controlar alucinações auditivas (HOFFMAN *et al.*, 2000; SILBERSWEIG *et al.*, 1995)

O futuro da TMS

A TMS é uma modalidade diagnóstica e terapêutica baseada em agentes físicos relativamente recente. Embora já se tenha conhecimentos de experimentos com a indução de correntes em nervos por D´Ansorval (1889) foi somente depois dos experimentos de Barker et al (1985) que a TMS começou a se popularizar. O que Barker e colaboradores conseguiram foi usar uma válvula como chave eletrônica para fazer o capacitor descarregar rapidamente e com isso se produzir o campo elétrico no interior do cérebro. Com o avanço dos componentes eletrônicos, a válvula foi substituída por um elemento de estado sólido, tornando os estimuladores mais compactos e fáceis de se usar.

Recentemente, foram propostas novas configurações do circuito eletrônico do equipamento de TMS. O objetivo é controlar a forma de onda da corrente elétrica do pulso de estimulação (PETERCHEV *et al.*, 2013). Sendo assim, estudos identificaram como os parâmetros de estimulação afetam a resposta fisiológica cerebral (HANNAH; ROTHWELL, 2017; ILMONIEMI *et al.*, 2016). Além do desenvolvimento eletrônico, novas propostas têm sido apresentadas para desenvolvimento das bobinas de estimulação. Denominada multi-locus TMS, permite alterar eletronicamente a orientação e a distribuição do campo elétrico no cérebro, isto é, sem movimentar a bobina (KOPONEN; NIEMINEN; ILMONIEMI, 2018). Essa técnica abre novas possibilidades para o estudo de conexões intra e intercorticais, bem como melhor interação com as redes cerebrais. Como se depreende os avanços tecnológicos são fundamentais para o amadurecimento da TMS.

Espera-se que em futuro próximo se possa controlar a forma e a orientação do pulso magnético e a sua penetração. Isso vai envolver o desenvolvimento de componentes eletrônicos de potência rápidos, fontes de corrente controladas por computador, bobinas com desenhos inovadores, uma integração com imagens anatômicas de alta resolução e dotadas de informação sobre as propriedades elétricas de cada seguimento, dentre outras coisas. Do ponto de vista clínico temos a interação do sujeito/paciente com o estimulador e para melhorar a precisão do método teremos que sair de 3D e ir para 4D, ou seja, o eixo do tempo tem que ser incorporado no processo. A maneira com que o nosso grupo pretende atacar esse aspecto é através da robótica e sensoriamento de posição.

Sensores podem medir a posição da bobina e do paciente e através de um sistema de controle possibilitar a estimulação da mesma área do cérebro mesmo que o sujeito se mova. Essa característica não somente irá melhorar a precisão da TMS mas também abrir novas possibilidades de aplicação para pacientes com tremor, crianças e todos aqueles que apresentam dificuldades para se manterem imóveis durante as sessões de TMS.

Conclusão

Comparada com outras áreas da física médica, a TMS é uma área relativamente nova, tendo surgido 90 anos após a descoberta dos raios X. Como mostrado nesta revisão, ainda existem muitas oportunidades a serem exploradas, não somente do ponto de vista instrumental e de processamento de sinais, como também no desenho de protocolos, análise de dados e propostas de modelos. Físicos são treinados com grande zelo para analisar e modelar experimentos, e as aplicações médicas em neurociências têm muito a ganhar com essas habilidades.

Referências

ARAÚJO, H. A.; FERRARETO IGLESIO, R.; SACCHI DE CAMARGO CORREIA, G.; TOLEDO, D.; FERNANDES, R. M.; GALHARDONI, R.; MARCOLIN, M. A.; TEIXEIRA, M. J.; CIAMPI DE ANDRADE, D. Estimulação magnética transcraniana e aplicabilidade clínica: perspectivas na conduta terapêutica neuropsiquiátrica Transcranial magnetic stimulation and clinical applicability: perspectives in neuropsychiatric therapeutics. Rev Med (São Paulo, v. 90, n. 1, p. 3–14, 2011.

BARKER, A. T.; JALINOUS, R.; FREESTON, I. L. Non-invasive magnetic stimulation of human motor cortex. The Lancet, v. 325, n. 8437, p. 1106–1107, 1985.

BENALI, A.; TRIPPE, J.; WEILER, E.; MIX, A.; PETRASCH-PARWEZ, E.; GIRZALSKY, W.; EYSEL, U. T.; ERDMANN, R.; FUNKE, K. Theta-Burst Transcranial Magnetic Stimulation Alters Cortical Inhibition. Journal of Neuroscience, v. 31, n. 4, p. 1193–1203, 2011.

BOROOJERDI, B.; FOLTYS, H.; KRINGS, T.; SPETZGER, U.; THRON, A.; TÖPPER, R. Localization of the motor hand area using transcranial magnetic stimulation and functional magnetic resonance imaging. Clinical neurophysiology : official journal of the International Federation of Clinical Neurophysiology, v. 110, n. 4, p. 699–704, abr. 1999.

BRASIL-NETO, J. P.; MCSHANE, L. M.; FUHR, P.; HALLETT, M.; COHEN, L. G. Topographic mapping of the human motor cortex with magnetic stimulation: factors affecting accuracy and reproducibility. Electroencephalogr Clin Neurophysiol, v. 85, n. 1, p. 9–16, 1992.

CONFORTO, A. B.; Z'GRAGGEN, W. J.; KOHL, A. S.; RÖSLER, K. M.; KAELIN-LANG, A. Impact of coil position and electrophysiological monitoring on determination of motor thresholds to transcranial magnetic stimulation. Clinical Neurophysiology, v. 115, n. 4, p. 812–819, 2004.

EPSTEIN, C. M.; WASSERMANN, E. M.; ZIEMANN, U. The Oxford handbook of transcranial stimulation. [s.l.] Oxford University Press, 2012. v. 191–764 p.

ETTINGER, G. J.; LEVENTON, M. E.; GRIMSON, W. E.; KIKINIS, R.; GUGINO, L.; COTE, W.; SPRUNG, L.; AGLIO, L.; SHENTON, M. E.; POTTS, G.; HERNANDEZ, V. L.; ALEXANDER, E. Experimentation with a transcranial magnetic stimulation system for functional brain mapping. Medical image analysis, v. 2, n. 2, p. 133–142, 1998.

FITZGERALD, P. B.; FOUNTAIN, S.; DASKALAKIS, Z. J. A comprehensive review of the effects of rTMS on motor cortical excitability and inhibition. Clinical Neurophysiology, v. 117, n. 12, p. 2584–2596, 2006.

FORSTER, M.-T.; LIMBART, M.; SEIFERT, V.; SENFT, C. Test-retest reliability of navigated transcranial magnetic stimulation of the motor cortex. Neurosurgery, v. 10 Suppl 1, n. 1, p. 51–5; discussion 55-6, 2014.

GARCIA, M. A. C.; SOUZA, V. H.; VARGAS, C. D. Can the Recording of Motor Potentials Evoked by Transcranial Magnetic Stimulation Be Optimized? Frontiers in Human Neuroscience, v. 11, n. August, p. 1–4, 2017.

GEORGE, M. S.; WASSERMANN, E. M.; WILLIAMS, W. A.; CALLAHAN, A.; KETTER, T. A.; BASSER, P.; HALLETT, M.; POST, R. M. Daily repetitive transcranial magnetic stimulation (rTMS) improves mood in depression. NeuroReport, v. 6, n. 14, p. 1853–1856, out. 1995.

GROPPA, S.; OLIVIERO, A.; EISEN, A.; QUARTARONE, A.; COHEN, L. G.; MALL, V.; KAELIN-LANG, A.; MIMA, T.; ROSSI, S.; THICKBROOM, G. W.; ROSSINI, P. M.; ZIEMANN, U.; VALLS-SOLÉ, J.; SIEBNER, H. R. A practical guide to diagnostic transcranial magnetic stimulation: Report of an IFCN committee. Clinical Neurophysiology, v. 123, n. 5, p. 858–882, 2012a.

GROPPA, S.; OLIVIERO, A.; EISEN, A.; QUARTARONE, A.; COHEN, L. G.; MALL, V.; KAELIN-LANG, A.; MIMA, T.; ROSSI, S.; THICKBROOM, G. W.; ROSSINI, P. M.; ZIEMANN, U.; VALLS-SOLÉ, J.; SIEBNER, H. R. A practical guide to diagnostic transcranial magnetic stimulation: Report of an IFCN committee Clinical Neurophysiology. Clinical Neurophysiology, v. 123, p. 858–882, 2012b.

HANNAH, R.; ROTHWELL, J. C. Pulse Duration as Well as Current Direction Determines the Specificity of Transcranial Magnetic Stimulation of Motor Cortex during Contraction. Brain Stimulation, v. 10, n. 1, p. 106–115, 2017.

HELMICH, R. C.; SIEBNER, H. R.; BAKKER, M.; MÜNCHAU, A.; BLOEM, B. R. Repetitive transcranial magnetic stimulation to improve mood and motor function in Parkinson's disease. Journal of the Neurological Sciences, v. 248, n. 1–2, p. 84–96, 2006.

HOFFMAN, R. E.; BOUTROS, N. N.; HU, S.; BERMAN, R. M.; KRYSTAL, J. H.; CHARNEY, D. S. Transcranial magnetic stimulation and auditory hallucinations in schizophrenia. The Lancet, v. 355, n. 9209, p. 1073–1075, 2000.

ILMONIEMI, R. J.; MÄKI, H.; SAARI, J.; SALVADOR, R.; MIRANDA, P. C. The Frequency-Dependent Neuronal Length Constant in Transcranial Magnetic Stimulation. Frontiers in Cellular Neuroscience, v. 10, n. August, 9 ago. 2016.

JULKUNEN, P. Methods for estimating cortical motor representation size and location in navigated transcranial magnetic stimulation. Journal of Neuroscience Methods, v. 232, p. 125–133, 2014.

JULKUNEN, P.; SÄISÄNEN, L.; DANNER, N.; NISKANEN, E.; HUKKANEN, T.; MERVAALA, E.; KÖNÖNEN, M. Comparison of navigated and non-navigated transcranial magnetic stimulation for motor cortex mapping, motor threshold and motor evoked potentials. NeuroImage, v. 44, n. 3, p. 790–795, 2009. Disponível em: <http://dx.doi.org/10.1016/j.neuroimage.2008.09.040>.

KLOMJAI, W.; KATZ, R.; LACKMY-VALLÉE, A. Basic principles of transcranial magnetic stimulation (TMS) and repetitive TMS (rTMS). Annals of Physical and Rehabilitation Medicine, v. 58, n. 4, p. 208–213, 2015a.

KLOMJAI, W.; KATZ, R.; LACKMY-VALLÉE, A. Basic principles of transcranial magnetic stimulation (TMS) and repetitive TMS (rTMS). Annals of Physical and Rehabilitation Medicine, v. 58, n. 4, p. 208–213, 2015b.

KOPONEN, L. M.; NIEMINEN, J. O.; ILMONIEMI, R. J. Multi-locus transcranial magnetic stimulation—theory and implementation. Brain Stimulation, v. 11, n. 4, p. 849–855, 2018.

LEENTJENS, A. F. G. Depression in Parkinson's disease: Conceptual issues and clinical challenges. Journal of Geriatric Psychiatry and Neurology, v. 17, n. 3, p. 120–126, 2004.

LEFAUCHEUR, J. P.; BRUGIÈRES, P.; GUIMONT, F.; IGLESIAS, S.; FRANCO-RODRIGUES, a.; LIÉGEOIS-CHAUVEL, C.; LONDERO, a. Navigated rTMS for the treatment of tinnitus: A pilot study with assessment by fMRI and AEPs. Neurophysiologie Clinique, v. 42, n. 3, p. 95–109, 2012.

MATTHÄUS, L.; SCHWEIKARD, Prof. Dr.-Ing. A. A robotic assistance system for transcranial magnetic stimulation and its application to motor cortex mapping. Institute for Robotics and Cognitive Systems, v. Ph.D., p. 174, 2008.

MULLER, V. T.; SANTOS, P. P. dos; CARNAVAL, T.; GOMES, M. da M. G.; FREGNI, F. O que é estimulação magnética transcraniana ? Revista brasileira de neurologia, v. 49, n. 1, p. 20–31, 2013.

OBERMAN, LINDSAY; PASCUAL-LEONE, A. Safety of Theta burst stimulation: A systematic review of the literature. v. 28, n. 1, p. 67–74, 2011.

PERES, A. S. C.; SOUZA, V. H.; CATUNDA, J. M. Y.; MAZZETO-BETTI, K. C.; SANTOS-PONTELLI, T. E. G.; VARGAS, C. D.; BAFFA, O.; DE ARAÚJO, D. B.; PONTES-NETO, O. M.; LEITE, J. P.; GARCIA, M. A. C. Can somatosensory electrical stimulation relieve spasticity in post-stroke patients? A TMS pilot study. Biomedizinische Technik, v. 63, n. 4, p. 501–506, 2018.

PERES, A. S. C.; SOUZA, V. H. O.; MAZIERO, D.; DE ARAUJO, D. B.; SALMON, C. E. G.; BAFFA, O. Vector magnetic field mapping of a Transcranial Magnetic Stimulation coil using Magnetic Resonance Imaging: in vitro and in vivo experiments. IFMBE Proceedings, v. 25, n. 7, p. 571–574, 2009.

PETERCHEV, A. V.; GOETZ, S. M.; WESTIN, G. G.; LUBER, B.; LISANBY, S. H. Pulse width dependence of motor threshold and input-output curve characterized with controllable pulse parameter transcranial magnetic stimulation. Clinical Neurophysiology, v. 124, n. 7, p. 1364–1372, 2013.

ROMERO, J. R.; RAMIREZ, D. M.; AGLIO, L. S.; GUGINO, L. D. Brain mapping using transcranial magnetic stimulation. Neurosurgery Clinics of North America, v. 22, n. 2, p. 141–52, vii, 2011.

ROSSINI, P. M.; BURKE, D.; CHEN, R.; COHEN, L. G.; DASKALAKIS, Z.; DI IORIO, R.; DI LAZZARO, V.; FERRERI, F.; FITZGERALD, P. B.; GEORGE, M. S.; HALLETT, M.; LEFAUCHEUR, J. P.; LANGGUTH, B.; MATSUMOTO, H.; MINIUSSI, C.; NITSCHE, M. A.; PASCUAL-LEONE, A.; PAULUS, W.; ROSSI, S.; ROTHWELL, J. C.; SIEBNER, H. R.; UGAWA, Y.; WALSH, V.; ZIEMANN, U. Non-invasive electrical and magnetic stimulation of the brain, spinal cord, roots and peripheral nerves: Basic principles and procedures for routine clinical and research application: An updated report from an I.F.C.N. Committee. Clinical Neurophysiology, v. 126, n. 6, p. 1071–1107, 2015. Disponível em: <http://dx.doi.org/10.1016/j.clinph.2015.02.001>.

ROSSINI, P. M.; ROSSI, S. Clinical applications of motor evoked potentials. Electroencephalography and clinical neurophysiology, v. 106, n. 3, p. 180–94, mar. 1998a.

ROSSINI, P. M.; ROSSI, S. Clinical applications of motor evoked potentials. Electroencephalography and clinical neurophysiology, v. 106, n. 3, p. 180–94, mar. 1998b. Disponível em: <http://www.ncbi.nlm.nih.gov/pubmed/9743275>.

RUOHONEN, J. Basic Physics and Design of Transcranial Magnetic Stimulation Devices and Coils. Em: Magnetic Stimulation in Clinical Neurophysiology. [s.l.] Elsevier, 2005. p. 17–30.

SÄISÄNEN, L.; PIRINEN, E.; TEITTI, S.; KÖNÖNEN, M.; JULKUNEN, P.; MÄÄTTÄ, S.; KARHU, J. Factors influencing cortical silent period: Optimized stimulus location, intensity and muscle contraction. Journal of Neuroscience Methods, v. 169, n. 1, p. 231–238, 2008.

SILBERSWEIG, D. A.; STERN, E.; FRITH, C.; CAHILL, C.; HOLMES, A.; GROOTOONK, S.; SEAWARD, J.; MCKENNA, P.; CHUA, S. E.; SCHNORR, L.; JONES, T.; FRACKOWIAK, R. S. J. A functional neuroanatomy of hallucinations in schizophrenia. Nature, v. 378, n. 6553, p. 176–179, nov. 1995.

SOLLMANN, N.; GOBLIRSCH-KOLB, M. F.; ILLE, S.; BUTENSCHOEN, V. M.; BOECKH-BEHRENS, T.; MEYER, B.; RINGEL, F.; KRIEG, S. M. Comparison between electric-field-navigated and line-navigated TMS for cortical motor mapping in patients with brain tumors. Acta Neurochirurgica, v. 158, n. 12, p. 2277–2289, 2016. Disponível em: <http://dx.doi.org/10.1007/s00701-016-2970-6>.

SOUZA, V. H.; BAFFA, O.; GARCIA, M. A. C. Lateralized asymmetries in distribution of muscular evoked responses: An evidence of specialized motor control over an intrinsic hand muscle. Brain Research, v. 1684, p. 60–66, 2018. Disponível em: <https://doi.org/10.1016/j.brainres.2018.01.031>.

SOUZA, V. H.; MATSUDA, R. H.; PERES, A. S. C.; AMORIM, P. H. J.; MORAES, T. F.; SILVA, J. V. L.; BAFFA, O. Development and characterization of the InVesalius Navigator software for navigated transcranial magnetic stimulation. Journal of Neuroscience Methods, v. 309, n. June, p. 109–120, 2018a. Disponível em: <https://linkinghub.elsevier.com/retrieve/pii/S0165027018302577>.

SOUZA, V. H.; VIEIRA, T. M.; PERES, A. S. C.; GARCIA, M. A. C.; VARGAS, C. D.; BAFFA, O. Effect of TMS coil orientation on the spatial distribution of motor evoked potentials in an intrinsic hand muscle. Biomedical Engineering / Biomedizinische Technik, v. 63, n. 6, p. 635–645, 27 nov. 2018b. Disponível em: <http://www.degruyter.com/view/j/bmte.ahead-of-print/bmt-2016-0240/bmt-2016-0240.xml>.

WASSERMANN, E. M.; MCSHANE, L. M.; HALLETT, M.; COHEN, L. G. Noninvasive mapping of muscle representations in human motor cortex. Electroencephalography and Clinical Neurophysiology/ Evoked Potentials, v. 85, n. 1, p. 1–8, 1992a.

WASSERMANN, E. M.; MCSHANE, L. M.; HALLETT, M.; COHEN, L. G. Noninvasive mapping of muscle representations in human motor cortex. Electroencephalography and clinical neurophysiology, v. 85, n. 1, p. 1–8, 1992b.

WASSERMANN, E. M.; ZIMMERMANN, T. Transcranial magnetic brain stimulation: Therapeutic promises and scientific gaps. Pharmacology and Therapeutics, v. 133, n. 1, p. 98–107, 2012.

ZIEMANN, U. Transcranial magnetic stimulation: Its Current Role in the Evaluation of Patients Post-Stroke. Neurology Report, v. 24, n. 3, 2000.